Applied Computational Electromagnetics Society

Journal

April 2013 Vol. 28 No. 4

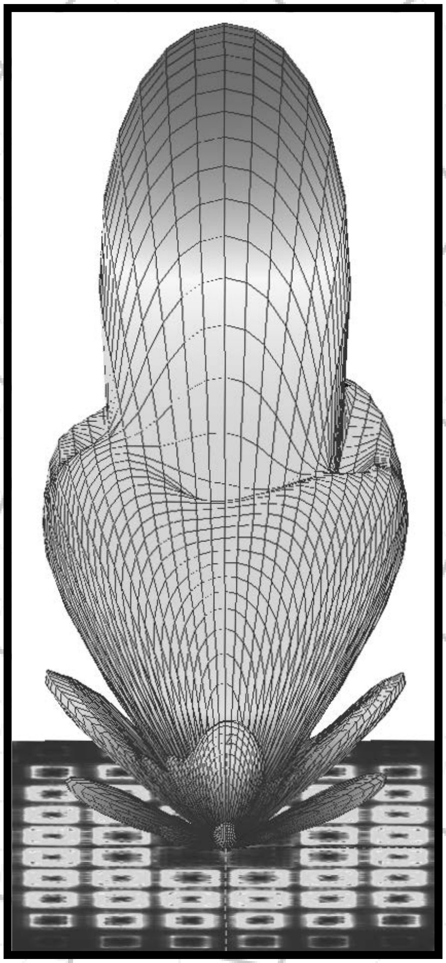

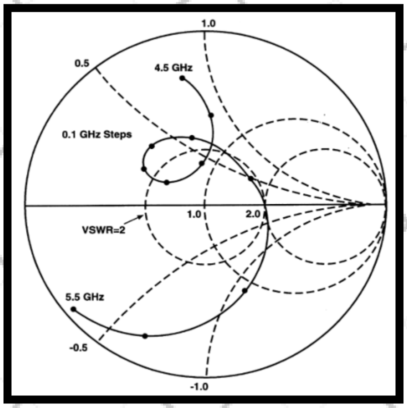

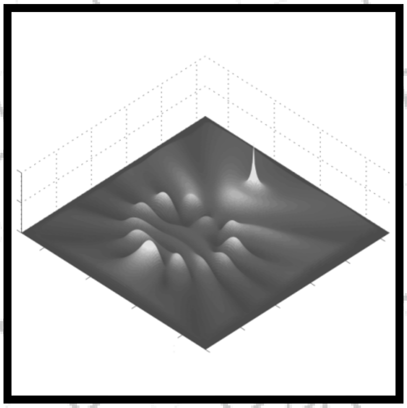

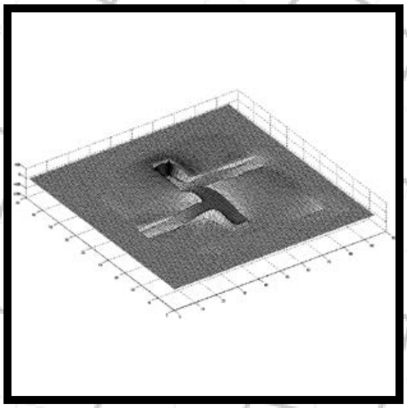

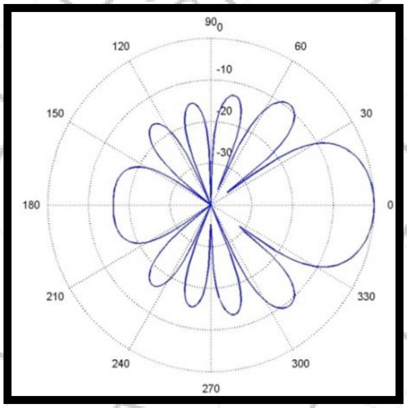

ISSN 1054-4887

GENERAL PURPOSE AND SCOPE: The Applied Computational Electromagnetics Society ***(ACES)*** Journal hereinafter known as the ***ACES Journal*** is devoted to the exchange of information in computational electromagnetics, to the advancement of the state-of-the art, and the promotion of related technical activities. The primary objective of the information exchange is to inform the scientific community on the developments of new computational electromagnetics tools and their use in electrical engineering, physics, or related areas. The technical activities promoted by this publication include code validation, performance analysis, and input/output standardization; code or technique optimization and error minimization; innovations in solution technique or in data input/output; identification of new applications for electromagnetics modeling codes and techniques; integration of computational electromagnetics techniques with new computer architectures; and correlation of computational parameters with physical mechanisms.

SUBMISSIONS: The ***ACES Journal*** welcomes original, previously unpublished papers, relating to applied computational electromagnetics. Typical papers will represent the computational electromagnetics aspects of research in electrical engineering, physics, or related disciplines. However, papers which represent research in applied computational electromagnetics itself are equally acceptable.

Manuscripts are to be submitted through the upload system of ***ACES*** web site http://www.aces-society.org See "Information for Authors" on inside of back cover and at ***ACES*** web site. For additional information contact the Editor-in-Chief:

Dr. Atef Elsherbeni
Department of Electrical Engineering
The University of Mississippi
University, MS 386377 USA
Phone: 662-915-5382
Email: atef@olemiss.edu

SUBSCRIPTIONS: All members of the Applied Computational Electromagnetics Society are entitled to access and download the ***ACES Journal*** any published journal article available at http://www.aces-society.org. Printed issues of the ***ACES Journal*** are delivered to institutional members. Each author of published papers receives a printed issue of the ***ACES Journal*** in which the paper is published.

Back issues, when available, are $50 each. Subscription to ***ACES*** is through the web site. Orders for back issues of the ***ACES Journal*** and change of address requests should be sent directly to ***ACES*** office at:

Department of Electrical Engineering
The University of Mississippi
University, MS 386377 USA
Phone: 662-915-7231
Email: aglisson@olemiss.edu

Allow four weeks advance notice for change of address. Claims for missing issues will not be honored because of insufficient notice, or address change, or loss in the mail unless the ***ACES*** office is notified within 60 days for USA and Canadian subscribers, or 90 days for subscribers in other countries, from the last day of the month of publication. For information regarding reprints of individual papers or other materials, see "Information for Authors".

LIABILITY. Neither ***ACES***, nor the ***ACES Journal*** editors, are responsible for any consequence of misinformation or claims, express or implied, in any published material in an ***ACES Journal*** issue. This also applies to advertising, for which only camera-ready copies are accepted. Authors are responsible for information contained in their papers. If any material submitted for publication includes material which has already been published elsewhere, it is the author's responsibility to obtain written permission to reproduce such material.

APPLIED
COMPUTATIONAL
ELECTROMAGNETICS
SOCIETY
JOURNAL

April 2013
Vol. 28 No. 4
ISSN 1054-4887

The ACES Journal is abstracted in INSPEC, in Engineering Index, DTIC, Science Citation Index Expanded, the Research Alert, and to Current Contents/Engineering, Computing & Technology.

The illustrations on the front cover have been obtained from the research groups at the Department of Electrical Engineering, The University of Mississippi.

THE APPLIED COMPUTATIONAL ELECTROMAGNETICS SOCIETY
http://aces.ee.olemiss.edu

EDITOR-IN-CHIEF

Atef Elsherbeni
University of Mississippi, EE Dept.
University, MS 38677, USA

ASSOCIATE EDITORS-IN-CHIEF

Sami Barmada
University of Pisa. EE Dept.
Pisa, Italy, 56126

Fan Yang
University of Mississippi, EE Dept.
University, MS 38677, USA

Mohamed Bakr
McMaster University, ECE Dept.
Hamilton, ON, L8S 4K1, Canada

Yasushi Kanai
Niigata Inst. of Technology
Kashiwazaki, Japan

Mohammed Hadi
Kuwait University, EE Dept.
Safat, Kuwait

Mohamed Abouzahra
MIT Lincoln Laboratory
Lexington, MA, USA

Alistair Duffy
De Montfort University
Leicester, UK

EDITORIAL ASSISTANTS

Matthew J. Inman
University of Mississippi, EE Dept.
University, MS 38677, USA

Anne Graham
University of Mississippi, EE Dept.
University, MS 38677, USA

EMERITUS EDITORS-IN-CHIEF

Duncan C. Baker
EE Dept. U. of Pretoria
0002 Pretoria, South Africa

Allen Glisson
University of Mississippi, EE Dept.
University, MS 38677, USA

David E. Stein
USAF Scientific Advisory Board
Washington, DC 20330, USA

Robert M. Bevensee
Box 812
Alamo, CA 94507-0516, USA

Ahmed Kishk
University of Mississippi, EE Dept.
University, MS 38677, USA

EMERITUS ASSOCIATE EDITORS-IN-CHIEF

Alexander Yakovlev
University of Mississippi, EE Dept.
University, MS 38677, USA

Erdem Topsakal
Mississippi State University, EE Dept.
Mississippi State, MS 39762, USA

EMERITUS EDITORIAL ASSISTANTS

Khaled ElMaghoub
University of Mississippi, EE Dept.
University, MS 38677, USA

Mohamed Al Sharkawy
Arab Academy for Science and
Technology, ECE Dept.
Alexandria, Egypt

Christina Bonnington
University of Mississippi, EE Dept.
University, MS 38677, USA

APRIL 2013 REVIEWERS

Ahmed Abdelrahman
Ahmed Attiya
Mohamed Bakr
Mouloud Challal
Mehdi Ghandehari
Ge Guang-Ding
Tuan-Yung Han
David Hill
Ahmad Hoorfar
Mark Ingalls
Mohammad Islam
Haider Khaleel
Zulfiqar Khan
Antonino Musolino
Lotfi Osman
Michael Schneider
Abhishek Shrivastava
Sellakkutti Suganthi
Jianpeng Wang
Qiang Yu
Amir Zaghloul
Qiaoli Zhang

THE APPLIED COMPUTATIONAL ELECTROMAGNETICS SOCIETY

JOURNAL

Vol. 28 No. 4 April 2013

TABLE OF CONTENTS

An Optimized Equivalent Source Modeling for the Evaluation of Time Harmonic Radiated Fields from Electrical Machines and Drives

M. R. Barzegaran, Ali Sarikhani, and Osama A. Mohammed

Energy systems Research Laboratory, Department of Electrical and Computer Engineering
Florida International University, Miami, FL 33174, USA
mohammed@fiu.edu

Abstract **─** A model for electrical machines useful for radiated electromagnetic field studies in a multi-source environment is proposed. The various aspects of electromagnetic signature are considered. This model was created from a representative rectangular prism carrying a set of unbalanced currents in its branches. The geometry and the currents of the equivalent model were calculated based upon a genetic algorithm-based particle swarm optimization process taking into consideration the actual size and the operating conditions of the drive system being studied. The electric field was chosen as the objective function, which is the main element of the optimization. The simulated results show acceptable accuracy and excellent simulation time as compared to the full 3D FE model of the actual machine. Various types of signature studies of the model were conducted. This included stationary and time analysis in addition to the effect of rotation of the machine. For verification, we utilized two machines in a connected system to study and compare the results with their actual model. The results show satisfactory accuracy. The practical implication of this effort is in the fact that, with this equivalent model, we can evaluate radiation and stray effects for EMC evaluation at the design stage.

Index Terms **─** Electromagnetic field signatures, electric machines and drives, finite element analysis, optimization, and time harmonic field analysis.

I. INTRODUCTION

In the recent years, there has been an increased interest in the expansion of multi-level numerical simulation methods for investigation of EMI issue, in the early stages of the design of electrical apparatus at low frequency. Systems such as electric drives and power converters circuits are in this category of systems being studied. The EMI studies of a complete motor drive system were performed by several numbers of researchers [1-9]. In [1, 2], the kHz range frequency models of the various components of a complete motor drive were developed. The efforts have been made to measure the EMI emissions from kHz up to the GHz range in the case of adjustable speed drives (ASD). The EMI modeling and simulation for inverters were also performed. For EMI caused by the ground current in [3], the coupled FE-circuit high frequency electric machine model for simulating electromagnetic interference in a motor drive was presented. The model can predict the EMI caused by the ground current and motor terminal overvoltage. The proposed model in [2] can be used as a computational prototyping tool for evaluating the high frequency operating conditions of electric machines numerically. Likewise, studies in lower frequency are performed. For signature studies outside the machine, Le Coat *et al* evaluated electromagnetic signatures of induction machines [4]. Two types of these machines were studied experimentally and theoretically using 2D and 3D methods. The 3D model consists of several frames as conductors and specific frame with suitable permeability as stator. The results show that this model has good accuracy and is suitable for single machine case

Submitted On: Dec. 6, 2012
Accepted On: Feb. 10, 2013

1054-4887 © 2013 ACES

study. More similar works, in this area, were conducted by others [5-9].

In order to study the electric and magnetic behavior of power components in multi component study, an accurate physics-based model of each component is considered in this paper. For instance, all windings, type of connections in addition to the geometrical features slot shapes; rotor and stators structure as well as material properties are considered in developing the actual machine model.

In addition to the electric machines, other components such as power converters, cables and transformers have very tiny elements. Considering all of these in the FEA model causes an increase in the computational complexity. In addition to considering the essential elements of each parameter for the EMI study, there is a need to observe the fields in far distances. Therefore, a very large region must be considered in such a model. Therefore, the number of degrees of freedom in meshing will increase dramatically and subsequently the speed of analysis will decrease. Consequently, logical simplification in designing components should be implemented.

In this paper, it is proposed to develop the complete geometrical model of the machine to a simple rectangular prism but it should produce similar electromagnetic behaviors for studying the EMI issues. The basic concept for EMI signature evaluation for this case is explained in section II below. The study approach was investigated in section III for the purpose of simplifying the model of electrical machine. The optimization process and other theoretical aspects are explained in this part. The electric field is chosen as the objective function, which is the most important parameters in the optimization. The various aspects of the model including time analysis are also studied. Since it is proposed to use this model as a typical model for an induction machine, other operating conditions of this machine are investigated. For verification purposes, in all part of this study, the results of the model are compared with the result of the actual model.

II. BASIC CONCEPT

We are primarily interested in the radiation pattern of the electric component (in this case electrical machines) at a distance from the source. Hence, the electromagnetic fields are usually measured at a considerably far distance from the components. The electric and magnetic fields specifically at an infinite distance can be the most effective index in investigating the EMI [10]. Since the wave length in power frequency, 60 Hz, is so large, the far distance means thousand kilometers or more. Therefore, the region and proposed measurement points, which are intended to be far, should be considered in a very far distance. However, computationally utilizing such a large region could be impossible. Hence, we need to obtain the fields virtually. The process of obtaining the fields, in this case, is investigated. Figure1 shows the geometry for calculating the EMI from the motor at a far distance.

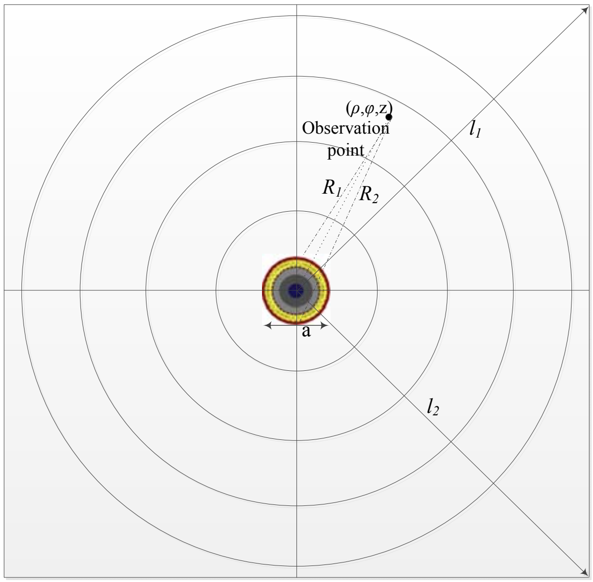

Fig. 1. Geometry for calculating the electromagnetic field at relatively far distances.

The present concept is based upon the Stratton-Chu [11] magnetic field intensity solution to the time-harmonic form of Maxwell's equations. The mathematical form used here, given by Silver [12, 13] yields the magnetic flux density as a volume integral of the electric and magnetic current densities, *J* and *M*, respectively,

$$\overline{B}\left(P\right)=\frac{-j}{4\pi\omega}\int_{V}[(\overline{M}.\overline{\nabla})\overline{\nabla}+k^{2}\overline{M}+j\omega\mu\overline{J}\times\overline{\nabla}].\frac{e^{-jkR}}{R}dV. \tag{1}$$

In the above equation, *P* denotes the observation point, *V* is the volume occupied by *J* and *M*. Here, *R* is the vector from the current density elements J and M to the observation point P. Also, ω is equal to $2\pi f$ where f is the frequency of the currents. Finally, k is the wave number given by $k = \omega(\mu\varepsilon)^{1/2}$, where ε and μ are the permittivity and permeability of the medium, respectively. The time-harmonic variation $e^{j\omega t}$ has been suppressed.

It is assumed that the volumetric current density elements, $J\ dV$, can be represented as linear current elements $I\ dl$, located at infinity and aligned with the current flow directions. Recalling that M = 0, and completing the indicated vector operations yield,

$$\overline{B}(P) = \frac{\mu}{4\pi}\int_{l_1}^{l_2}[\left(jk+\frac{1}{\boldsymbol{R}}\right)\frac{e^{-jkR}}{R}].I(l)\left(\overline{dl}\times\overline{u_R}\right) \quad (2)$$

where u_R is the unit vector pointing in the direction of R. The bracketed term in equation (2) describes the time-harmonic retardation effects for the current element $I\ dl$, and suggests a criterion for using a quasi-static electromagnetic formulation. The l_1 and l_2 are considered the distance of the source to the end of the region to have the possibility of the calculation of the radiated B at any given P point in the area. The geometry is illustrated in Figure 1. Examining equation (2), it is seen that whenever,

$$R << \frac{c}{2\pi f}, \quad (3)$$

where c is the homogenous medium light speed, the bracketed term may be approximated by $1/\mathbf{R}^2$ and equation (2) reduces to the electromagnetic quasi-static result,

$$\overline{B}(P) \cong \frac{\mu}{4\pi}\sum_{i=1}^{2}\int_{l_1}^{l_2}[\frac{1}{\boldsymbol{R_i}^3}I_i(l)].\left(\overline{dl_i}\times\overline{R_i}\right)]. \quad (4)$$

In equation (4), the summation is over the two points of the source with I, being the currents in the motor wires, dl, the current elements along the motor wires, and R, the vectors from the current elements dl, to the observation point P (i = 1 and 2 for the corresponding points). Additionally, to facilitate computer programming, the vector R, is used in the cross product of equation (4). This is in contrast to the unit vector u_R, which was used in equation (2), resulting in R_i^3 in the integrand denominator of equation (4).

Returning to equation (4), the distances R_i between the differential line elements dl_i and the observation point, P, are (see Fig. 1),

$$R_1 = [\rho^2 + a^2 - 2\rho a\cos\left(\varphi - 2\pi z\right) + \left(Z - z\right)^2]^{1/2}, \quad (5)$$

$$R_2 = [\rho^2 + a^2 + 2\rho a\cos\left(\varphi - 2\pi z\right) + \left(Z - z\right)^2]^{1/2}, \quad (6)$$

where ρ, φ, and z are the cylindrical coordinates of the observation point and a is the width of the source. Assuming that the currents I_i, are oppositely directed, identical, and uniform over the length of the winding in the motor, substitution of the differential current elements dl_i and the distances R_i into equation (4) yields the Cartesian components of the magnetic flux density,

$$\begin{aligned}B_x = \frac{\mu I}{4\pi}\int_{z_1}^{z_2}\{\boldsymbol{R_1}^{-3}[2\pi a\left(Z-z\right)\cos\left(2\pi z\right)+a\sin\left(2\pi z\right)- \\ \rho\sin\left(\varphi\right)]+R_2^{-3}[2\pi a\left(Z-z\right)\cos\left(2\pi z\right)+a\sin\left(2\pi z\right)+ \\ \rho\sin\left(\varphi\right)]\}dz,\end{aligned} \quad (7)$$

$$\begin{aligned}B_y = \frac{\mu I}{4\pi}\int_{z_1}^{z_2}\{R_1^{-3}[2\pi a\left(Z-z\right)\sin\left(2\pi z\right)-a\cos\left(2\pi z\right)+ \\ \rho\cos\left(\varphi\right)]+R_2^{-3}[2\pi a\left(Z-z\right)\sin\left(2\pi z\right)-a\cos\left(2\pi z\right)- \\ \rho\cos\left(\varphi\right)]\}dz,\end{aligned} \quad (8)$$

$$\begin{aligned}B_z = \frac{\mu I}{4\pi}\int_{z_1}^{z_2}2\pi a\{R_1^{-3}\left[a-\rho\cos\left(\varphi-2\pi z\right)\right]- \\ R_2^{-3}[a+\rho\cos\left(\varphi-2\pi z\right)]\}dz.\end{aligned} \quad (9)$$

In the above equations, I is the total current in each wire of the motor in phase A, z_1, and z_2 are the axial coordinates of the electrical machine end points, and R_1 and R_2 are given by equations (5) and (6). According to standards, when ρ = 0, equations (7) to (9) reduce to the well-known expressions for the on-axis magnetic flux densities of motors in the region, [14, 15].

In order to derive the electric field as well as the magnetic field, with the spherical coordinate components of B known, the next step is straightforward [10]. The free space relationship shown in equation (10) is applied to equation (11),

$$H = \mu_0^{-1}B, \quad (10)$$

$$E = \frac{1}{j\omega\varepsilon_0}\nabla\times H. \quad (11)$$

The analysis method, which is used in this analysis, is the generalized minimal residual method (usually abbreviated GMRES) with successive over-relaxation (SOR) pre and post smoothers. The GMRES is an iterative method for the numerical solution of system of linear equations [16]. In numerical linear algebra, the SOR is a variant of the Gauss–Seidel method for solving a linear system of equations, resulting in faster convergence. The convergence is shown in Fig. 2. A similar method can be used for any slowly converging iterative process. The SOR method uses a more accurate approximation of the matrix, which leads to fewer iterations but slightly more work is required per iteration than in the Jacobi method. It should be noted that the problem consists of nonlinear equations due to the presence of the B-H curve of the core of the motor. The iterative solver solves the problem by dividing the nonlinear curves to the sets of linear one as μ_r ramp and solving each of them individually [16].

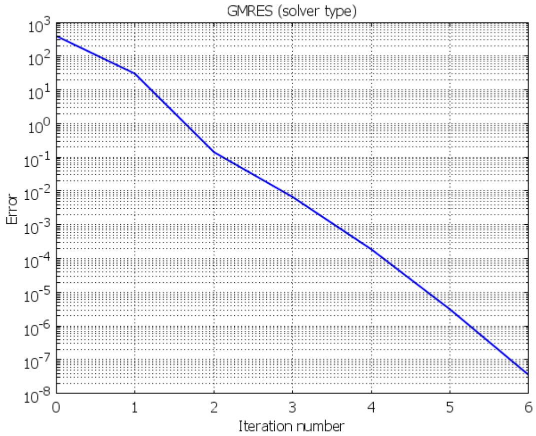

Fig. 2. Convergence of the problem using GMRES solver.

III. STUDY APPROACH

The electromagnetic signature study of the electrical machine in Figs. 1 and 3 (a) can be estimated based on equations (7) to (11). Since the electric and magnetic fields are interconnected to each other through equations (10) and (11), studying each of them shows the behavior of the electric machine at a far distance. However, as it is mentioned earlier, estimating the parameters of electrical machines at far distances requires significant time especially for multi-component studies using physics-based simulations. Therefore, a logical simplification was used here throughout the optimization.

The proposed equivalent machine model for signature study is a rectangular prism as shown in Fig. 3 (b). The cylinder around the model is for concentrating meshes to have accurate results. The rectangular prism model has currents in all of its branches, which are evaluated based upon an intelligent optimization process. The rectangular prism lengths (A, B, C) and the corresponding currents to each leg (i_{x1} i_{x2} i_{x3} i_{x4}, i_{y1} i_{y2} i_{y3} i_{y4}, and i_{z1} i_{z2} i_{z3} i_{z4}) are calculated. The proposed optimization process (GA-based PSO) is explained next.

PSO is a population-based algorithm that exploits a population of individuals to probe promising region of the search space. In this context, the population is called swarm and the individuals are called particles. Each particle moves with an adaptable velocity within the search space and retains in its memory the best position it ever encountered. The global variant of PSO, the best position ever attained by all individuals of the swarm is communicated to all the particles. The general principles for the GA and the PSO algorithms are stated in [17].

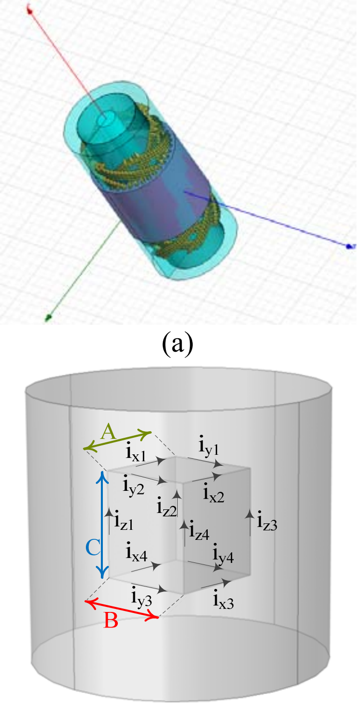

(a)

(b)

Fig. 3. Prototype of the proposed machine (SCIM) in finite element analysis for (a) actual model and (b) an equivalent current loop model for signature studies.

In order to prevent premature convergence to suboptimal solutions, Raymond Tan augmented a binary PSO with a GA-based mutation operator and achieved significant improvement in the rate of successful convergence [18]. Therefore, in the current study we incorporated a mutation operator into our continuous-space PSO algorithm. This mutation operator reinitiates the value of each continuous variable into its feasible range by a predefined probability (e.g., 5 %).

In this study, the number of population is set to 7, and for preventing explosion of the swarm, the maximum allowable velocity along each dimension is set to half of its feasible ranges. The results show that, in this application, for different number of switching angles, the algorithm converges within 100 to 150 iterations. Hence, in a conservative manner, the number of iterations is set to 30. Also, for enhancing the PSO's ability in escaping from local minima, a mutation operator is incorporated into the algorithm. The results indicate that, it is better to utilize this operator in discrete iteration intervals, with different probability. In this study, the mutation probabilities for iteration intervals of {5, 7} and {7, 30} are 1 % and 3 %, respectively. Other iteration intervals are not influenced by mutation.

The objective function of the optimization process for this case is the main index for evaluating the values of the model. This is because the initial and the later in the process, the modified values are just compared by means of the objective function. For this paper as mentioned earlier, the electric field was chosen, which is because of sensitivity of electric field in signature studies. In other words, the effect of changes on the condition of the component has influence on the electric field [19]. Consequently, the objective function is assigned as follows,

$$\begin{aligned} obj = mean(&|Ex_{motor}| - |Ex_{rp}| + |Ey_{motor}| \\ &- |Ey_{rp}| + |Ez_{motor}| - |Ez_{rp}|). \end{aligned} \tag{12}$$

where Ex, Ey, and Ez represent the normal electric field along a line in x, y, and z directions. The indices, *motor* and *rp* stands for actual 3D motor model, and its correspondence to the rectangular prism current loop model (see Fig. 3).

IV. SIMULATION APPROACH

In this study, the finite element analysis is used as an accurate method for physics-based simulation. The analysis of electromagnetic finite element method is based on equation (13) and typical Maxwell equations,

$$\nabla \times \mathbf{H} = \mathbf{J} = \sigma(\mathbf{E} + \mathbf{v} \times \mathbf{B}) + \mathbf{J}^e \tag{13}$$

where $\mathbf{J}^e$ is an externally generated current density and $\mathbf{v}$ is the velocity of the conductor. Note that **B** and **E** are used uniquely in magnetic or electric solution, respectively, but are fully coupled here.

Using the definitions of the fields $\mathbf{B} = \nabla \times \mathbf{A}$ and $E = -\nabla V - j\omega \boldsymbol{A}$ and combining them with the constitutive relationships $\mathbf{B} = \mu_0 (\mathbf{H} + M)$ and $D = \varepsilon_0 \mathbf{E}$ and rewriting Ampere's law, the required current density will be achieved,

$$\begin{aligned} &(j\omega\sigma - \omega^2\varepsilon_0)\mathbf{A} + \nabla \times (\mu_0^{-1} \nabla \times \mathbf{A} - \mathbf{M}) \\ &-\sigma \mathbf{v} \times (\nabla \times \mathbf{A}) + (\sigma + j\omega\varepsilon_0)\nabla V = \mathbf{J}^e. \end{aligned} \tag{14}$$

The equation of continuity is obtained by taking the divergence of Ampere's law. This equation is solved for the electric potential. Thus the following equations for V and A is obtained,

$$\begin{aligned} &-\nabla.\Big((j\omega\sigma - \omega^2\varepsilon_0)\mathbf{A} - \sigma \mathbf{v} \times (\nabla \times \mathbf{A}) \\ &+(\sigma + j\omega\varepsilon_0)\nabla V - (\mathbf{J}^e + j\omega \mathbf{P})\Big) = 0. \end{aligned} \tag{15}$$

A particular gauge can be obtained by reducing the system of equation by choosing $\Psi = -jV/\omega$ in the gauge transformation. Therefore, the modified magnetic vector potential is obtained as

$$\tilde{\mathbf{A}} = \mathbf{A} - \frac{j}{\omega} \nabla V . \tag{16}$$

Working with $\tilde{\mathbf{A}}$ is often the best option when it is possible to specify all source currents as external currents $\mathbf{J}^e$ or as surface currents on boundaries,

$$\begin{aligned} &\left(j\omega\sigma - \omega^2\varepsilon_0\right)\tilde{\mathbf{A}} + \nabla \times \left(\mu_0^{-1} \nabla \times \tilde{\mathbf{A}} - \mathbf{M}\right) - \\ &\sigma \mathbf{v} \times \left(\nabla \times \tilde{\mathbf{A}}\right) + \left(\sigma + j\omega\varepsilon_0\right)\nabla V = \mathbf{J}^e + j\omega \mathbf{P} \ , \end{aligned} \tag{17}$$

where $\mathbf{A}$ is magnetic potential, $\mathbf{J}^e$ is external current density, **M** is magnetization and $\mathbf{v}$ is the motion speed, which here, it is equal to zero. Equation (17) is a modified version of the classic quasi-static equation (15), which is implemented in the FE software. The magnetic field density (**B**) for the evaluation of the radiated field would be calculated by getting **A** from equation (17) and applying it to $\mathbf{B} = \nabla\times\mathbf{A}$.

Further modification in this study is applied by linking Matlab software with FE software. This can be done by defining a variable in Matlab codes as **D** (electric displacement field) and making a link to the FE software, then considering this new **D** instead of the default D. This new defined electric displacement field is based on the electric field obtained from the software solution. The other element ($\tilde{\mathbf{A}}$) is defined in the same way.

V. SIMULATION RESULT AND DISCUSSION

For simulation purposes, a 3-phase, 380-V, 5-A, 120-turn/phase induction machine with stack length of 0.15 m and outer diameter of 17.5 cm is simulated in the 3D electromagnetic FE domain for one instant of time at the frequency of 60 Hz. The electric field along three lines in the *x*, *y*, and *z* directions are calculated. The optimization process was then implemented.

Following the optimization process, the rectangular prism length are calculated as (A = 0.1009 m, B = 0.125 m, C = 0.1282 m). Table 1 shows the calculated current for the rectangular prism branches following the optimization process in one case. Although the optimization is performed with the electric field as the objective function, the magnetic field radiated form the proposed model also shows great similarity when it compares with actual model.

Table 1: The calculated current for rectangular prism legs.

i_{x1}	i_{x2}	i_{x3}	i_{x4}
-61.18	528.12	-267.44	-107.82
i_{y1}	i_{y2}	i_{y3}	i_{y4}
-115.25	-251.54	36.107	424.1
i_{z1}	i_{z2}	i_{z3}	i_{z4}
-150.03	-99.84	4.46	-135.6

The comparison between the normal electric field of the actual 3D model and the cubic model for one motor case is illustrated in various circumstances. For brevity, only some indices including field spectrum, arrow-line and stream-line are selected for the study. For instance, electric field spectrum radiated from the actual machine and the equivalent models are compared as shown in Fig. 4. Also, magnetic field density spectrum was compared and is shown in Fig. 5. The magnetic field density is evaluated with the same amount of current shown in Table 1 for this specific case.

Considering Fig. 4, the accuracy of the E field in all coordinates is significantly similar as the difference between the two models, which is really negligible. By choosing different optimization parameters including; mutation probabilities, iteration intervals, and number of iteration, the inaccuracy of the equivalent model in some points can be fixed. As shown in Figs. 4 and 5, the electromagnetic fields radiate dipole fields at far distance because the machine will act similar to a complex loop and a loop will propagate dipole electromagnetic fields.

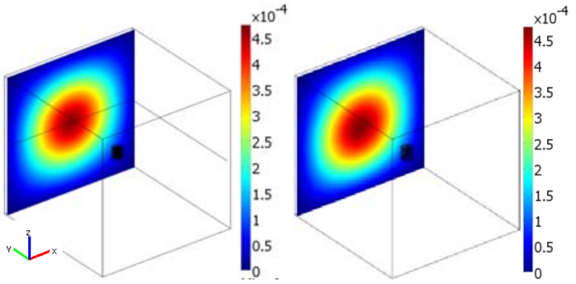

(a) (b)

Fig. 4. Electric field spectrum (V/m) of (a) actual machine and (b) equivalent source model in the *xz*-plane.

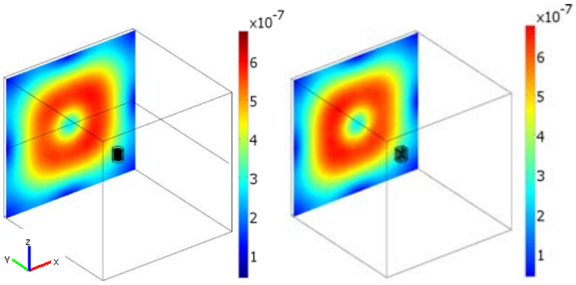

(a) (b)

Fig. 5. Magnetic field density spectrum (T) of (a) actual machine and (b) equivalent source model in the *xz*-plane.

The figure shows that with the amount of current in Table 1, the equivalent model has similar electromagnetic behavior to the actual machine as the signature study point of view. In addition to the importance of the accuracy of the field spectrums, the direction of the flowing fields is significant because the field spectrum figures, Figs. 4 and 5, don't show the direction of the fields. Hence, the arrow line of magnetic field density of the actual and equivalent machines are compared and shown in Fig. 6. As displayed in this figure, the magnetic field in the actual case around the motor is denser in comparison with the equivalent source model case. However, the radiated magnetic field at further distance is almost the same in these two models. This is more important because the model is designed for far distance. While the arrow plot in Fig. 6 shows the magnetic field density, this can be classified as discrete streamline of this field. A continues stream-line of the H field (magnetic field intensity) of the two models (actual and equivalent source models) is obtained as shown in Fig. 7. The H field streamline also shows that the equivalent source model has very similar result to the actual model. It also shows that the dipoles establish around the equivalent source model also in near distance. It should be noted that the purpose of this model was to obtain resembling fields at far distance.

For other conditions of the machine; for example other voltages or power rates and/or other size of the machine, the ratio of the new condition to a basic condition can be considered. The basic case could be any case similar to the case studied in this paper. Then this ratio will be applied to the currents. It is likely to have similar results compared to the actual case in the new condition. As mentioned earlier in the paper, the main goal of this research is to study the signature of multi machine system. For validation of the calculated equivalent source model (rectangular prism) from one motor case, the model is compared in a case containing two motors, as shown in Fig. 8, while the current in the branches of the rectangular prism model remain the same as in the first case. The centers of the coordinates of the two rectangular prisms are exactly the same as the 3D motor model. The figure shows a comparison between the electric field spectrum in the actual and rectangular prism model for the two motor cases. As can be seen, the electric fields similarly follow the same patterns with acceptable accuracy. Also magnetic field density, which is shown in Fig. 9 has a very good accuracy in comparison with the actual model.

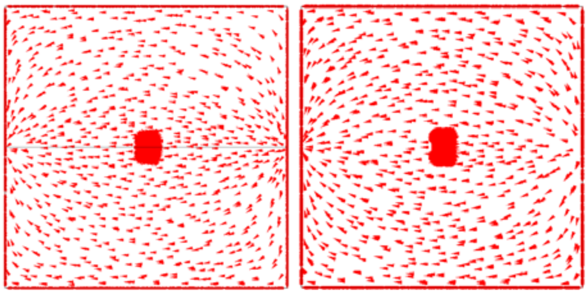

(a) (b)

Fig. 6. Arrow plot of magnetic field density (T) of (a) actual machine and (b) equivalent model in the *xy*-plane.

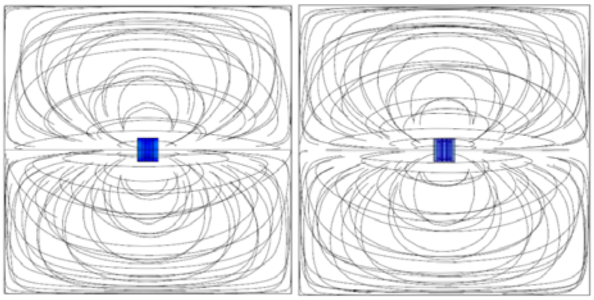

(a) (b)

Fig. 7. Stream-line of H field of (a) actual machine model in the *xy*-plane (A/m) and (b) equivalent source model in the *xy*-plane (A/m).

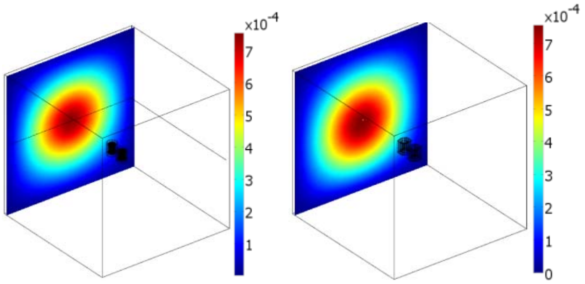

(a) (b)

Fig. 8. Electric field spectrum (V/m) of (a) actual machine and (b) equivalent source model in the *xz*-plane in the two machine case.

A. Simulation time comparison

Comparison between the simulation time of the actual model and equivalent model shows that this approach makes the simulation at least 100 times faster than the full 3D model. This enables the numerical simulation of multiple sources in a reasonable time allowing the practical study of EMC issues during electric drive development stages. Moreover, it is observed that in case of evaluation of the field in some directions more accurate results can be calculated.

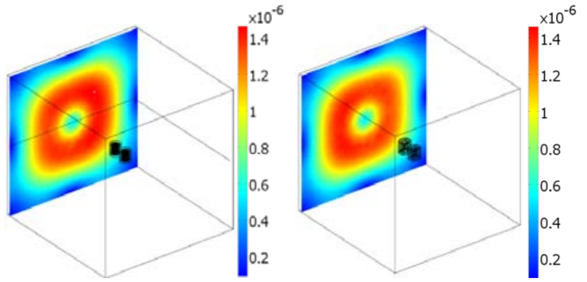

(a) (b)

Fig. 9. Magnetic field density (T) spectrum of (a) actual machine and (b) equivalent model in the *xz*-plane in the two machine case.

VI. TIME AND ROTATION STUDY

A. Time-based analysis

Since the actual induction machine carries AC current, the time-based analysis is more useful. Although in the previous sections, the analysis was time-based however, the figures are just depicted in one typical moment of time. In this section, the radiated electromagnetic fields of different instances of time in one cycle are studied. For brevity, four time instances are selected (0.0025 s, 0.005 s, 0.0075 s, and 0.0125 s). The voltage amplitude of the terminal of the model during one time cycle is shown in Fig. 10.

Firstly, the radiated magnetic field in the near distance (0.5 m) from the machine is studied. The magnetic field density measured in four time instants is shown in Fig. 11. The result shows that the magnetic field rotates by the variation in time, although the position of the maximum field point remained unchanged. It can be inferred from this result that the model resembles the machine and can be used instead of that at all time instants not just one time instant in which the model is designed. Next, the radiated magnetic field at a far distance (~10 m) from the machine is studied. In this distance the rule of the magnetic dipoles for these distances cause the field become similar to a dipole as shown in Fig. 12 [20]. As shown in this figure, the dipoles are sensitive to time changes and they rotates when the time changes. Consequently, the equivalent source model can be used for the time-based analysis at near and far distances.

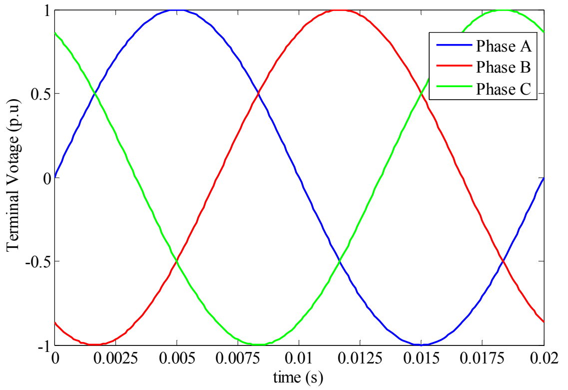

Fig. 10. Voltage amplitude of the terminal of the model during one time cycle.

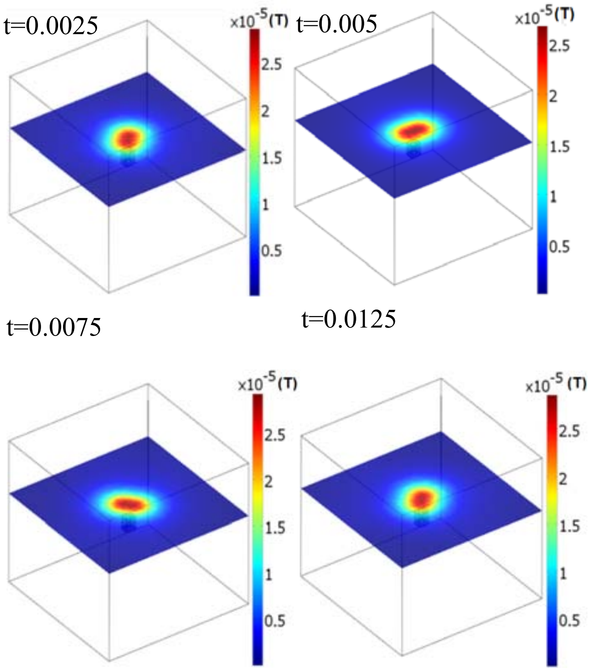

Fig. 11. Magnetic field density (B) of equivalent model in four different moments of time at near distance.

B. The effect of rotation

Another condition that should be studied for the induction machine is testing various positions of the machine. In many cases, the location of the motor with respect to the measured points will change. Therefore, the electromagnetic signatures are expected to be changed. Hence, a specific change of the motor is studied here. The whole machine was rotated around an axis and the results were obtained and illustrated in Fig. 13. The magnetic field in this figure is plotted at a far distance.

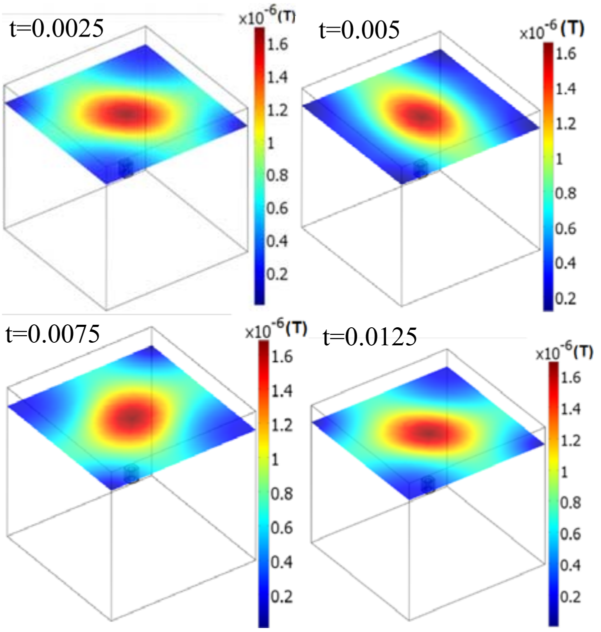

Fig. 12. Magnetic field density (B) of equivalent model at the four different intendances of time at far distance.

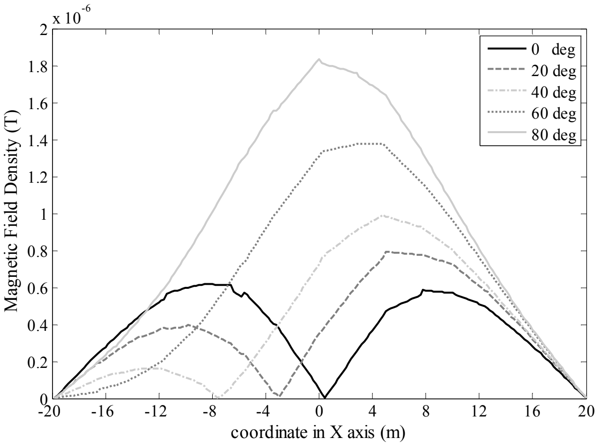

Fig. 13. Deviation of magnetic field density (B) of the equivalent model due to the rotation of the whole machine around z-axis.

As shown in Fig. 13, by rotating the stator of the induction machine around the z-axis, the magnetic field moves along the perpendicular coordinates (x, y) from right to left. When plotting other angles ranging from 90 to 180 degrees, the results are exactly symmetrical with respect to the changes from 0 to 90 degrees. The magnetic field density of 180 degree change is exactly the same as the one with 0 degree change. This study is useful in identifying the situation of the source machine by looking at the signatures at far distance. All of these studies can be imported to an optimization program such as genetic algorithm or neural network. Therefore, the machine in any situation can be recognized.

VII. CONCLUSION

Considering the simulation of multi-machine environment with actual models requires significant time and large computing resources. An equivalent source model for these electric machines for the purpose of evaluation signatures and radiated fields are designed, presented, and verified. A rectangular prism model was proposed with variable currents in its branches. The GA-based PSO method was used for evaluating the currents of the rectangular prism branches while the electric field was chosen as objective function because of its sensitivity to the change of situation. A modified finite element analysis was used, which include modification in the equations in which deviation of electric displacement field over time was considered. The accuracy of the results shows that it is possible to replace the actual model of the electrical machines with the equivalent rectangular prism current model for signature studies. The simulation time of the equivalent source rectangular prism model is approximately 100 times less than the actual model enabling the numerical simulation of multiple cases.

The model was validated by considering a two machine case as a representative situation of multi machine case. The actual models in two machine case were replaced with equivalent models in the sample position with the same values of single machine cases. The results show excellent accuracy with considerable simulation time reduction. This facilitates the numerical simulation of multiple electromagnetic sources in a reasonable time allowing the practical study of important issues such as EMC standards during the development stages of electric drives systems. Furthermore, time harmonic analysis and the effect of rotation were investigated. These types of studies are useful in recognizing the condition of the source machine by looking at its signatures at a far distance.

REFERENCES

[1] O. A. Mohammed and S. Ganu, "FE-circuit coupled model of electric machines for simulation and evaluation of EMI issues in motor drives," *IEEE Transactions on Magnetics,* vol. 46, no. 8, pp. 3389-3392, Aug. 2010.

[2] O. A. Mohammed, S. Ganu, N. Abed, S. Liu, and Z. Liu, "High frequency phase variable model of electric machines from electromagnetic field computation," *Appl. Comp. Electro. Society (ACES) Journal*, vol. 22, no. 1, pp. 164-171, Mar. 2007.

[3] A. Rosales, A. Sarikhani, and O. A. Mohammed, "Evaluation of radiated electromagnetic field interference due to frequency switching in PWM motor drives by 3D finite elements," *IEEE Transactions on Magnetics*, vol. 47, no. 5, pp. 1474-1477, May 2011.

[4] G. Coat, A. Foggia, JP. Bongiraud, and P. Thiec, "Electromagnetic signature of induction machines," *IEEE Transaction on Energy Conversion,* vol. 14, no. 3, pp. 628-632, Sep. 1999.

[5] H. Hasper, "Reduction of magnetic stray field from squirrel-cage induction motors," *COMBIMAC document*, Feb. 1991.

[6] X. Brunotte, G. Meunier, and J. P. Bongiraud, "Ship magnetizations modeling by the finite element method," *IEEE Transactions on Magnetics*, vol. 29, no. 2, pp. 1970-1975, Mar. 1993.

[7] G. G. Karady, Sh. FI. Berisha, J. A. Demcko, and M. Samotyj, "Variable speed motor drive generated magnetic fields," *IEEE Transactions on Power Delivery*, vol. 9, no. 3, pp. 1639-1646, July 1994.

[8] A. Sarikhani and O. A. Mohammed, "Coupled electromagnetic field computation with external circuit for the evaluation the performance of electric motor designs," *Appl. Comp. Electro. Society (ACES) Journal*, vol. 26, no. 12, pp. 997-1006, Dec. 2011.

[9] J. H. Alwash and L. J. Qaseer, "Three-dimension finite element analysis of a helical motion induction motor," *Appl. Comp. Electro. Society, (ACES) Journal*, vol. 25, no. 8, pp. 703-712, Aug. 2010.

[10] F. Ulaby, *Fundamental of Applied Electromagnetics*, 5th Edition, Prentice Hall, Massachusetts, pp. 321-324, 2006.

[11] J. A. Stratton and L. J. Chu, "Diffraction theory of electromagnetic waves," *Physical Review*, vol. 56, pp. 99-107, 1939.

[12] S. Silver, *Microwave Antenna Theory and Design*. McGraw-Hill, 1949, MIT Rad. Lab. Series, vol. 12, Ch. 3, reprinted by Peter Peregrinus Ltd., London, UK, 1986.

[13] G. R. Piper and A. Prata, "Magnetic flux density produced by finite-length twisted-wire pairs," *IEEE Transactions on Electromagnetic Compatibility,* vol. 38, no. 1, pp. 84-92, Feb. 1996.

[14] W. R. Smythe, *Static and Dynamic Electricity*, vol. 28, McGraw-Hill, New York, pp. 296-298, 1968.

[15] J. G. Van Bladel, *Electromagnetic Fields*, vol. 19, John Wiley & Sons, New York, pp. 157, 1985.

[16] Y. Saad, *Iterative Methods for Sparse Linear Systems*, 2nd edition, Society for Industrial and Applied Mathematics, 2003.

[17] C. –F. Juang, "A hybrid of genetic algorithm and particle swarm optimization for recurrent network design," *IEEE Transactions on Cybernetics, Systems, Man, and Cybernetics, Part B,* vol. 34, no. 2, pp. 997-1006, Apr. 2004.

[18] R. Raymond, "Hybrid evolutionary computation for the development of pollution prevention and control strategies," *Journal of Cleaner Prod.*, vol. 15, no. 10, pp. 902-906, 2007.

[19] J. William, Y. Pan, E. J. Fenyves, I. Sujisawa, H. Suyama, N. Samadi, and G. H. Ross, "Electromagnetic field sensitivity," *Electromagnetic Biology and Medicine*, vol. 10, no. 1-2, pp. 241-256, 1991.

[20] T. L. Chow, *Introduction to Electromagnetic Theory: A Modern Perspective*, Jones & Bartlett Learning, Massachusetts, 2006.

Mohammadreza Barzegaran obtained B.Sc. and M.Sc. Degrees in Power Engineering from University of Mazandaran, Iran in 2007 and 2010, respectively. He is currently pursuing the Ph.D. degree in the department of Electrical and Computer Engineering, Florida International University, Florida, USA. His research interests include studying electromagnetic compatibility in power components, life assessment of electrical power components, fault detection in electrical machines, and also computer-aid simulation of power components. He has many published papers in international journals and conferences.

Ali Sarikhani received his Bachelor degree in Transmission and Distribution Engineering in Power and Water University of Technology, Iran. He followed his Masters in Power Electrical Engineering in Shahrood University of Technology, Iran. He is now a Ph.D. Candidate of Electrical Engineering at Energy Systems Research Lab, Florida International University, USA. His current interests are computational design prototyping, computational electromagnetic, and fault tolerant machine-drive systems.

Osama A. Mohammed (S'79, M'83 SM'84, F'94): is a Professor of Electrical and Computer Engineering and the Director of the Energy Systems Research Laboratory at Florida International University. He received his M.S. and Ph.D. degrees in Electrical Engineering from Virginia Polytechnic Institute and State University. He published numerous journal articles over the past 30 years in areas relating to power systems, electric machines and drives, computational electromagnetics and in design optimization of electromagnetic devices, artificial intelligence applications to energy systems. He authored and co-authored more than 350 technical papers in the archival literature. He has conducted research work for government and research laboratories in shipboard power conversion systems and integrated motor drives. He is also interested in the application communication and wide area networks for the distributed control of smart power grids. He has been successful in obtaining a number of research contracts and grants from industries and Federal government agencies for projects related to these areas. Professor Mohammed also published several book chapters including; Chapter 8 on direct current machinery in the Standard Handbook for Electrical Engineers, 15th Edition, McGraw-Hill, 2007 and a book Chapter entitled " Optimal Design of Magnetostatic Devices: the genetic Algorithm Approach and System Optimization Strategies," in the Book entitled: Electromagnetic Optimization by Genetic Algorithms, John Wiley & Sons, 1999.

Professor Mohammed is a Fellow of IEEE and is the recipient of the IEEE PES 2010 Cyril Veinott Electromechanical Energy Conversion Award. Dr. Mohammed is also a Fellow of the Applied Computational Electromagnetic Society. He is Editor of IEEE Transactions on Energy Conversion, IEEE Transactions on Magnetics, IEEE Transactions on Smart Grid and COMPEL. Professor Mohammed was the past President of the Applied Computational Electromagnetic Society (ACES). He received many awards for excellence in research, teaching and service to the profession and has delivered numerous invited lectures at scientific organizations around the world.

Professor Mohammed has been the general chair of several international conferences including; ACES 2006, IEEE-CEFC 2006, IEEE-IEMDC 2009, IEEE-ISAP 1996 and COMPUMAG-1993. He has also chaired technical programs for other major international conferences including; IEEE-CEFC 2010, IEEE-CEFC-2000 and the 2004 IEEE Nanoscale Devices and System Integration. Dr. Mohammed also organized and taught many short courses on power systems, Electromagnetics and intelligent systems in the U.S.A and abroad. Professor Mohammed has served ACES in various capacities for many years. He also serves IEEE in various Boards, committees and working groups at the national and international levels.

Design, Full-Wave Analysis, and Near-Field Diagnostics of Reflectarray Antennas

Payam Nayeri[1], Atef Z. Elsherbeni[1], and Fan Yang[1, 2]

[1] Center of Applied Electromagnetic Systems Research
Department of Electrical Engineering
University of Mississippi, University, MS 38677-1848, USA
pnayeri@olemiss.edu, atef@olemiss.edu, fyang@olemiss.edu

[2] Microwave and Antenna Institute
Electronic Engineering Department
Tsinghua University, Beijing 100084, China

Abstract **─** This article presents a detailed procedure for design, modeling, full-wave simulation, and near-field diagnostics of reflectarray antennas, through a case study of a Ka-band reflectarray antenna with 437 elements. A comparison between analytical approaches and full-wave simulations for reflectarray radiation analysis is also presented, illustrating the necessity of full-wave approaches for an accurate analysis. Furthermore, the phase shift provided by the phasing elements, in the real reflectarray configuration, is analyzed by using the near-field data from the full-wave simulation. This provides a means to diagnose a designed reflectarray, and identify phasing elements that are not providing the required phase shift. The effectiveness of the diagnostic approach is demonstrated through numerical examples.

Index Terms – Far-field, near-field, radiation pattern, and reflectarray.

I. INTRODUCTION

Reflectarray antennas combine some of the best features of reflectors and array antennas, and create a hybrid design, which is well suited for high-gain applications [1-8]. The flat aperture of the reflectarray antenna consists of phase changing elements, which mimic the parabolic reflector curved surface, and create the collimated beam. In comparison with an array antenna, the feed network is replaced by a space feed, which is simple, and moreover eliminates the distribution losses associated with large arrays [1]. With the rapid advancement of printed circuit technology, reflectarray antennas can offer a low profile, low mass, and low cost solution for high-gain antennas in deep space communication systems.

Different approaches for analysis of reflectarray radiation pattern have been developed over the years [1-5]. These numerical approaches provide a fast method to compute the radiation pattern of the reflectarray antenna with a good accuracy; however, several approximations are made in the analysis. With these approaches usually a good agreement between measured and simulated results is observed in the pattern shape, but in most cases there are some discrepancies in side-lobe level and cross-polarization levels [5]. In general, an accurate analysis of a reflectarray antenna radiation performance requires a full-wave simulation; however, this is quite challenging. The electrically large size of the reflectarray antenna aperture, combined with hundreds of elements with dimensions smaller than a wavelength, demands an efficient full-wave technique. Considering the planar geometry of the reflectarray antenna aperture, a surface meshing approach will be more appropriate for this problem. As such, the method of moment (MoM) technique will be more advantageous than other full-wave techniques such as finite element or finite difference, which require volume meshing.

Submitted On: Sept. 30, 2012
Accepted On: Feb. 11, 2013

In this paper we present a detailed procedure for design, modeling, and full-wave simulation of a reflectarray antenna through a case study of a 437-element Ka-band design. In addition, the near-field data is obtained by the full-wave simulation, and the performance of the phasing elements is studied in the real reflectarray configuration. This illustrative field visualization can serve as a useful diagnostic tool for antenna engineers to observe the performance of each element on the reflectarray aperture and potentially correct the phasing elements that are not providing the necessary phase shift.

II. REFLECTARRAY ANTENNA SYSTEM DESIGN

Designing a reflectarray antenna is usually carried out in several stages, and as such, it can be viewed as a system design. The main stages in this process are: designing the aperture, feed positioning, phasing element design, and designing or selecting a feed antenna. The geometry of the reflectarray antenna system is given in Fig. 1.

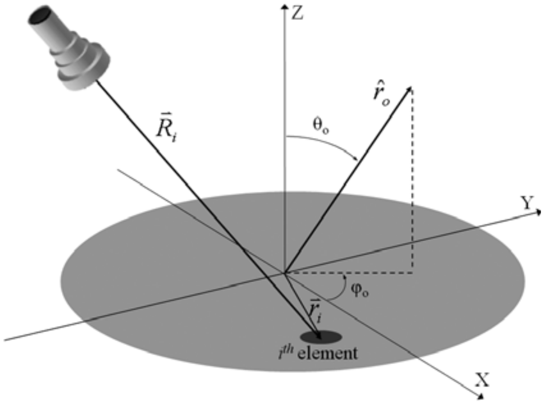

Fig. 1. Basic geometry of a reflectarray antenna system.

A. Aperture design and feed positioning

In aperture type antennas such as reflectarrays, the antenna gain is proportional to the electrical size of the aperture [9]. Therefore, if the required gain is specified for the antenna, one only needs to determine the aperture size that can achieve such a gain level. Aperture efficiency however plays a major role here, and to achieve high aperture efficiency [2], several factors must be taken into account in the design. Here we will outline the design process for a 32 GHz Ka-band reflectarray for a 30 dB gain.

A circular geometry is selected for the reflectarray aperture, since it can attain higher aperture efficiency in comparison with rectangular geometries. The diameter of the aperture (D) is set to be 12.5 λ at the design frequency of 32 GHz, which has a maximum directivity of 31.88 dB. With this relatively small aperture, an offset feed would be necessary to avoid blockage effects, thus a tilt angle of 25° is selected for the feed. The next task is to determine the feed position. In reflector antennas this is usually specified by the F/D ratio. One generally has two options for the design. If a specific feed is to be used, one has to determine the optimum F/D. On the other hand, one can choose the F/D, and design a feed antenna that achieves the optimum radiation performance. This is quite advantageous, since increasing F/D improves several characteristics of the reflectarray. In any case, the optimum values are determined based on efficiency analysis [10]. Here we chose the latter approach. An F/D of 0.75 was selected for the system, and the task was to determine the optimum feed radiation pattern that achieves maximum aperture efficiency.

The radiation pattern of the feed is usually modeled as a $\cos^q(\theta)$ function with no azimuth dependence, therefore one only needs to determine the optimum value of q [11]. The optimum value of q was determined to be 6.5, which corresponds to an aperture efficiency of 74.14 %. These results are given in Fig. 2. Here η_i, η_s, and η_a, are the illumination, spillover, and aperture efficiencies, respectively.

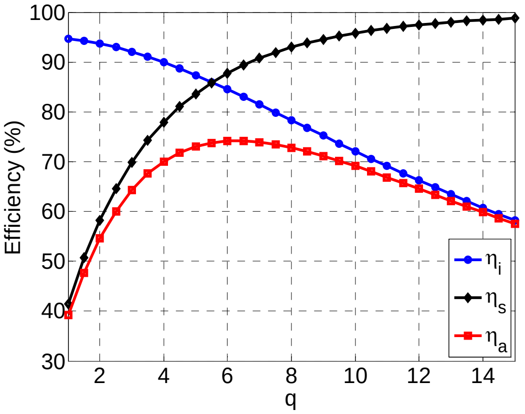

Fig. 2. Aperture efficiency of the reflectarray antenna as a function of feed cosine q power.

As discussed earlier, an offset system is used for the feed here. To minimize beam squint in offset reflectarrays, the beam direction should be equal to the offset feed angle, thus the beam direction is set to 25° [12]. This projected aperture size reduction (cos 25°) corresponds to a loss of 0.43 dB. Combined with the losses due to aperture efficiency (74.14 % or 1.3 dB), the estimated gain of the aperture designed here is 30.15 dB, which is quite close to the desired value.

B. Phasing element design

The phase shift distribution on a reflectarray aperture is designed to compensate for the spatial delay associated with the feed antenna, and provide a progressive phase shift on the aperture that points the collimated beam at a specific direction. Mathematically, the required phase shift of the i^{th} element on the aperture in Fig. 1 is given by,

$$\psi_i = k(R_i - \bar{r}_i \cdot \hat{r}_o) + \psi_0 . \qquad (1)$$

The phase constant ψ_0 indicates that a relative phase rather than an absolute phase is required in reflectarray design. The key concept however is how these individual elements are designed to scatter electromagnetic waves with the desired phases. Different methods have been demonstrated over the years to control the reflection phase of the elements, which can be categorized into three general groups: 1) phase/time delay lines, 2) variable size elements, and 3) rotated elements. For our design here we use the variable size technique, where a small shift in the resonant frequency of an element is introduced by changing the dimension that has the effect of changing the phase of the reflected field.

The reflectarray aperture is excited with a feed antenna that in general, may be positioned at an arbitrary angle and distance from the reflectarray, but is assumed to be far enough so that the incident field can be approximated by a plane wave. As such, the conventional approach for analysis and design of reflectarray phasing elements is to use a plane wave excitation. The infinite-array approach is often used for analysis of reflectarray elements, which takes the mutual coupling between the elements into account by means of the periodic boundary conditions [13]. While it is implicit that some approximation is made in this element analysis approach, i.e., ignoring the quasi-periodic nature of the reflectarray elements, as long as the variation of the element geometry is not significant between adjacent elements, this is quite acceptable in most cases [1, 2].

The phasing elements used in our design are variable size square patches, and the unit-cell size is 4.7 × 4.7 mm^2. The substrate has a thickness of 0.508 mm, and the dielectric constant is 2.2. The patch sizes vary from 1 mm to 4.5 mm with a resolution of 0.1 mm. The reflection phase responses of the elements are obtained using the commercial software Ansoft Designer [14], which is based on the MoM. Note that for reflectarray element designs, the reference plane for reflection phase calculation is the top surface of the element. It is worthwhile to point out that while full-wave simulation of the elements is usually very fast for simple geometries such as the single-layer patch element designed here, if necessary one may limit the number of simulated element dimensions and use a fitted curve for the element design. The reflection phase response of variable size elements usually forms an S-curve; therefore it can also be approximated with an inverse tangent function. The function used for the interpolation is

$$\psi = -b_l \frac{180}{\pi} \tan^{-1}\left(a_l (L - L_0)\right) + c_l . \qquad (2)$$

For this design a_l = 4.814, b_l = 1.868, c_l = -14.72, and L_0 = 2.722, where these parameters were evaluated using the curve fitting toolbox in Matlab [15].

Both simulated and interpolated reflection phase response of the elements, under normal incidence excitation, are given in Fig. 3. Also the simulated reflection phase response for 30° oblique excitation is given for comparison, where it can be seen that a normal incidence approximation is quite acceptable for this angular range.

C. Feed antenna design

Based on the efficiency analysis presented earlier, a feed antenna with an azimuthally symmetric radiation pattern and $\boldsymbol{q}$ = 6.5 is required for this reflectarray system. Typically horn antennas are used as reflector feeds [11]; however, the conventional pyramidal and conical horn antennas cannot achieve a symmetric radiation performance. One of the most fundamental methods to achieve a symmetric radiation pattern with a horn antenna is to excite higher-order modes in the horn waveguide that is done by introducing a step change into the diameter of the horn. Therefore, the Potter horn antenna [16] was selected as the feed, where the waveguide steps generate the TM_{11} mode. Combined with the fundamental TE_{11} mode, this will generate azimuthally symmetric fields at the horn aperture, which in turn corresponds to azimuthally symmetric radiation patterns for the horn. A cross sectional geometry of the Potter horn antenna is given in Fig. 4.

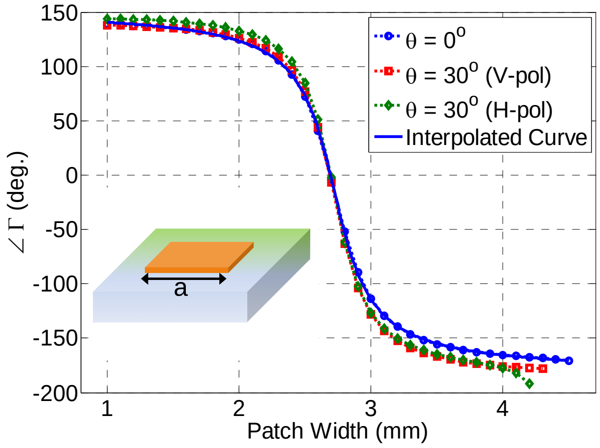

Fig. 3. Reflection phase versus patch size for the reflectarray elements.

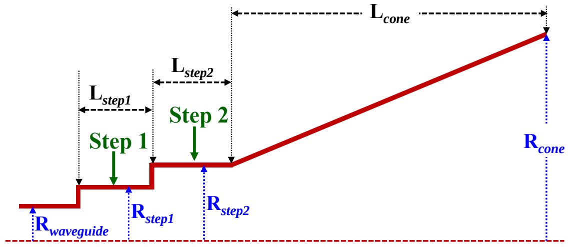

Fig. 4. Cross sectional view of a Potter horn antenna.

To achieve a symmetric radiation pattern with a Potter horn antenna, one has to determine the required portion of power that is transferred to the TM_{11} mode, thus the conventional design approach is to use a mode matching technique [17]. While this approach will ensure a symmetric radiation pattern, it will generally not allow one to control the shape of the pattern. On the other hand, several design parameters are available in a Potter horn antenna; therefore another design approach is to tune these parameters to achieve the desired radiation performance. In our design, full-wave simulation of the horn antenna was done using FEKO [18], and the particle swarm optimizer [19] was used to tune the parameters, and achieve the desired pattern. In total, 7 parameters were optimized for this design. These are the radius of the waveguide feed ($R_{waveguide}$), the radius and length of two waveguide steps (R_{step1}, L_{step1}, R_{step2}, L_{step2}), and the radius and length of the cone (R_{cone}, L_{cone}). At each fitness evaluation during the optimization, the radiation pattern is computed at a number of discrete points chosen to match the required $\cos^q(\theta)$ pattern and achieve a symmetric pattern in both *E*- and *H*- planes. The radiation pattern of the optimized horn antenna is given in Fig. 5, while the optimized dimensions of the Potter horn are given in Table 1 at 32 GHz.

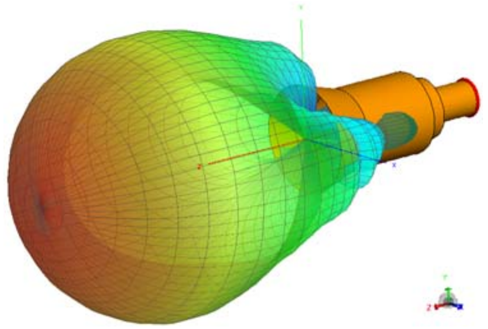

Fig. 5. Radiation pattern of the Potter horn antenna.

Table 1: Optimized dimensions of the Potter horn antenna (λ = 9.37 mm).

Parameter	Dimension (λ)
$R_{waveguide}$	0.323
R_{step1}	0.571
L_{step1}	0.386
R_{step2}	0.763
L_{step2}	1.539
R_{cone}	1.009
L_{cone}	0.848

As discussed earlier, the important consideration in our design here was not only to achieve a symmetric pattern, but also to match it with the ideal $\boldsymbol{cos^{6.5}}(\theta)$ model. A comparison between the ideal model and the optimized horn pattern is given in Fig. 6, where it can be seen that the optimized horn antenna completely matches the required pattern up to 40º, which is sufficient for the excitation of the reflectarray antenna.

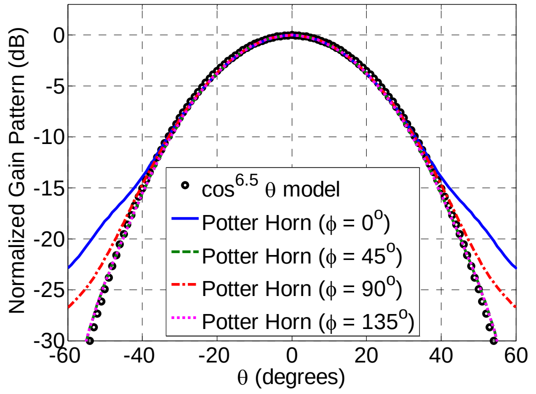

Fig. 6. Comparison between the radiation pattern of an ideal feed and the Potter horn antenna.

III. FULL-WAVE SIMULATION OF THE REFLECTARRAY ANTENNA

A. Full-wave simulation using FEKO

The next stage in the design is modeling the entire reflectarray antenna system. As discussed earlier, the electrically large size of the reflectarray antenna aperture, combined with hundreds of elements with electrically small dimensions, makes the full-wave simulation a challenging task. Here we use the commercial software FEKO v.6.1 for full-wave simulation of the reflectarray antenna.

The Ka-band reflectarray antenna has a circular aperture with a diameter of 12.5 λ at the design frequency of 32 GHz. The feed horn is positioned at X_{feed} = -37.1 mm, Y_{feed} = 0 mm, Z_{feed} = 79.6 mm based on the coordinate system in Fig. 1, and is pointing toward the geometrical center of the array. The patch dimensions are designed to generate a beam in the direction of (θ, φ) = (25°, 0°). In total 437 square patch elements are to be placed on the aperture. Modeling the feed horn, substrate layer, and ground plane is straightforward; however modeling the patches requires further attention. Considering the large number of variable size patches in a reflectarray antenna, it would be efficient if one imports the patch elements with a geometry file, which contains the location and dimension of each patch. For this design, a dxf file was created using Matlab© and imported into FEKO. The mask of the reflectarray phasing elements, and the geometry of the reflectarray system modeled in FEKO are shown in Fig. 7. For this design 434,450 unknown basis functions need to be calculated by the FEKO method of moments (MoM) solver. Considering the large number of unknowns, the multilevel fast multi-pole method (MLFMM) solver in FEKO was selected for this simulation. In total, the full-wave simulation here required 22.25 GB of memory with a CPU time of 19.94 hours on an 8 core 2.66 GHz Intel(R) Xeon(R) E5430 computer. The simulated radiation pattern of the reflectarray antenna is shown in Fig. 8.

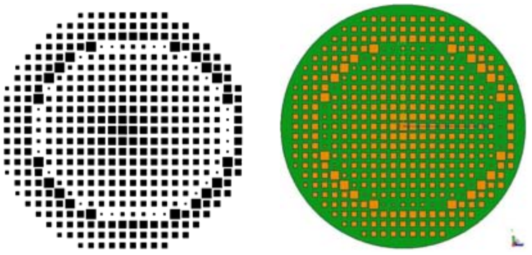
(a) (b)

Fig. 7. (a) Mask of the reflectarray phasing elements and (b) model of the reflectarray antenna in FEKO.

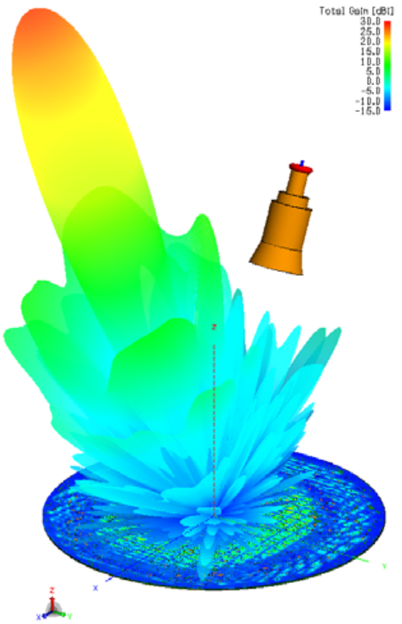

Fig. 8. Simulated radiation pattern of the 437 element Ka-band reflectarray antenna.

The main beam is correctly scanned to 25º off-broadside, which indicates that the phasing elements are providing the necessary phase shift on the reflectarray aperture. The computed maximum gain of the reflectarray antenna is 28.22 dB, which corresponds to an aperture efficiency of 43.05 %. The side-lobe and cross-polarization levels are -23.5 dB and -28.6 dB, respectively. It should be pointed out that the full-wave simulation takes into account all approximations in reflectarray element design as well as the edge diffraction effects. Therefore the full-wave simulation here can provide a good measure to observe the performance of the reflectarray elements in the real reflectarray application environment.

B. Comparison with analytical solution

Different analytical approaches are available to calculate the radiation characteristics of the reflectarray antennas. However in general, several approximations are made in these methods. Therefore, some discrepancies are usually observed in comparison with full-wave or measured results. This is primarily due to element design approximations, mutual coupling, and edge diffraction effects, which are not taken into account in these methods. Furthermore, for smaller reflectarrays the approximations in the analysis are less accurate, and as such they show a larger discrepancy with the measured results. Nonetheless, the analytical approaches can serve as a fast and comparable method to verify the full-wave simulation results presented in the previous section.

For the study here we used the aperture field approach [4], where the radiation pattern of the reflectarray antenna is calculated using the tangential fields on the reflectarray aperture. To compare the radiation patterns of the two approaches, we study the radiation patterns in the 2-D planes that best capture the radiation features of the antenna, i.e., the principal planes (P.P.), which are defined according to [20]. For this configuration, P.P.1 is the *xz*-plane and P.P.2 is the *yz'*-plane in the *xyz'*-coordinate system. This *xyz'*-coordinate system is obtained by rotating the *xyz*-coordinate system, 25º about the *y*-axis. The radiation patterns in the principal planes are shown in Fig. 9. It can be seen that a good agreement in the co-polarized radiation pattern shape is observed between the analytical and full-wave approach. In addition, the main beam direction, beam-width, side-lobe, and cross-polarization level in the main beam area show a close agreement. The discrepancies however, which are mainly observed outside the main beam areas, are due to the approximations in the aperture field approach. This study also reveals that analytical approaches have limited accuracy, and when accurate radiation pattern computation in the entire 3-D space is required, full-wave simulation of the reflectarray system is necessary.

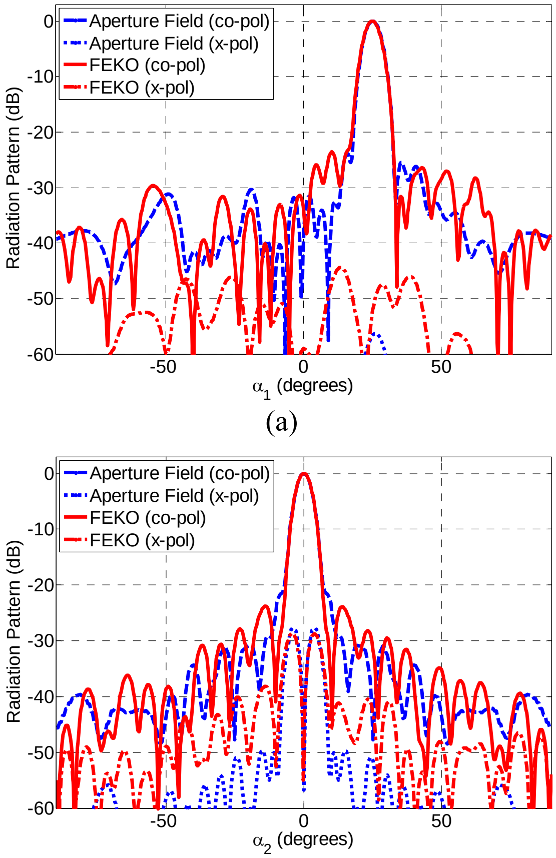

(a)

(b)

Fig. 9. Radiation pattern of the reflectarray antenna: (a) P.P.1 and (b) P.P.2.

It is worthwhile to point that the aim of the study here was to analyze the accuracy of the reflectarray radiation pattern computed using analytical approaches, thus comparison with full-wave simulations is more advantageous than measurements, since measurement results are susceptible to both fabrication and measurement errors. However, it is worth mentioning that our analytical approach has been confirmed by successful fabrication and experimental verification of several reflectarrays, as demonstrated in [20, 21].

IV. NEAR-FIELD ANALYSIS AND ELEMENT DIAGNOSTICS

A. Phase shift of reflectarray elements

A detailed procedure and a successful design of a Ka-band reflectarray antenna were presented in the previous sections. One of the notable advantages of a full-wave simulation is that in addition to calculating the far-field radiation performance, it can also provide the electromagnetic field quantities in the near field of the reflectarray system. For a reflectarray antenna this can be quite advantageous, since as discussed in section II, several approximations are made in the element design and in general, performance evaluation of the elements would require a near-field analysis. It should be noted that the near-field study here requires analysis of the scattered field. Therefore in addition to the full-wave simulation in section III, which provides the total field, one must also perform another simulation for the feed antenna alone, to obtain the incident fields. The phase of the incident and total electric fields on the reflectarray aperture are given in Fig. 10. It should be noted that since the feed horn antenna is *x*-polarized, the phase is only given for the $\boldsymbol{E_x}$ component.

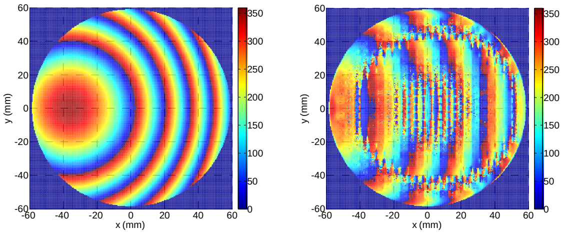

(a) (b)

Fig. 10. Phase of the electric field on the aperture: (a) incident and (b) total.

The aim of this study is to observe the phase shift provided by the phasing elements of the reflectarray antenna. From the total and incident fields, the scattered fields are calculated using

$$\vec{E}_{scattered} = \vec{E}_{total} - \vec{E}_{incident}\,. \tag{3}$$

The phase of the scattered electric fields (for the $\boldsymbol{E_x}$ component) on the reflectarray aperture is given in Fig. 11. The phase shift provided by the reflectarray elements can then be calculated as

$$\text{Element Phase Shift} = \angle\vec{E}_{scattered} - \angle\vec{E}_{incident}\,. \tag{4}$$

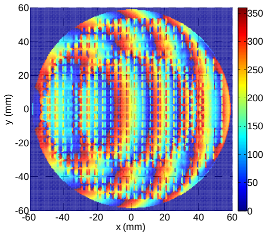

Fig. 11. Phase of the scattered electric field on the aperture.

This provides a useful visualization to determine if the phasing elements are designed correctly and are providing the necessary phase shift. Comparison between the elements ideal phase shift and the quantized phase shift resulted from the full-wave simulation of the reflectarray is given in Fig. 12. These results clearly indicate that for this design, the phasing elements on the reflectarray aperture are generating a phase shift that creates the collimated beam. In terms of performance diagnostics, if any errors are made in the phasing element design and placement, this study will be able to detect the elements that are not providing the necessary phase shift.

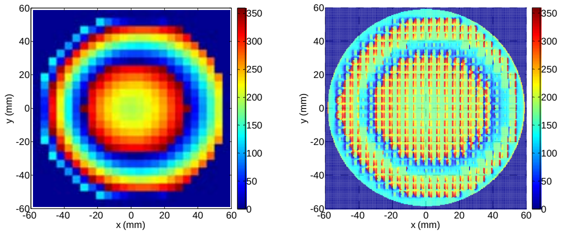

(a) (b)

Fig. 12. Phase shift on the reflectarray aperture: (a) ideal phase shift and (b) phase shift obtained from full-wave simulation.

B. Random phase error and diagnostic

To better illustrate this near-field diagnostic technique, we also designed a reflectarray antenna with randomly distributed patch dimension error in a small segment on the aperture. The error, with a maximum of 1 mm, is randomly distributed in a circle at the top right quadrant of the array. It is worthwhile to note here that in practice these errors could be due to fabrication, wear, or even design errors. The mask of the reflectarray phasing elements, and the phase shift on the aperture are shown in Fig. 13.

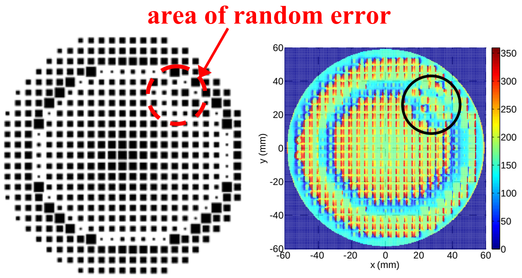

(a) (b)

Fig. 13. (a) Mask of the reflectarray antenna with randomly distributed error and (b) phase shift on the aperture of the reflectarray antenna based on full-wave simulation.

It can be seen that, while it is quite difficult to observe these small dimensional errors in Fig. 13 (a), the computed phase shift on the aperture can clearly show the elements that are not providing the necessary phase shift, thus illustrating the advantages of full-wave near-field diagnostics proposed in this paper. It is worthwhile to point out that while in the study here only 30 elements, i.e., less than 7 % of the total number of elements, exhibit phase error, the radiation performance also shows notable degradation. A comparison between the radiation patterns of both designs is given in Fig. 14.

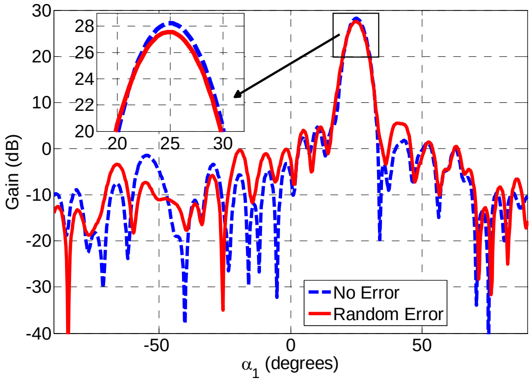

Fig. 14. Radiation pattern of the reflectarray antenna.

It can be seen that in addition to some beam deterioration, the maximum gain of the antenna has also been reduced from 28.22 dB to 27.56 dB. Furthermore, while the gain reduction here is about 0.66 dB, if such a phase error shall be observed in a strongly illuminated region, i.e., the geometrical center of the array, it would correspond to a greater loss.

V. CONCLUSION

A detailed procedure for design, modeling, and full-wave simulation of reflectarray antennas was presented. This was demonstrated through a case study of a 437-element Ka-band reflectarray antenna with comprehensive details on aperture, phasing element, and feed antenna design. In addition, comparison between analytical solution and full-wave simulation is also presented, which clearly illustrates the necessity of full-wave approaches for an accurate radiation analysis of reflectarray antennas. Moreover, the performance of each individual element of the reflectarray antenna was obtained in the real reflectarray configuration through the computed near-field. This is a useful tool for diagnosing and providing corrections when defected elements are observed.

ACKNOWLEDGMENT

The authors acknowledge EM Software & Systems (USA) Inc. for providing us with a full evaluation version of FEKO v.6.1. This work was supported by NASA EPSCoR program under the contract number NNX09AP18A.

REFERENCES

[1] J. Huang and J. A. Encinar, *Reflectarray Antennas*, by Institute of Electrical and Electronics Engineers, John Wiley & Sons, 2008.

[2] D. M. Pozar, S. D. Targonski, and H. D. Syrigos, "Design of millimeter wave microstrip reflectarrays," *IEEE Trans. Antennas Propag.*, vol. 45, no. 2, pp. 287-296, Feb. 1997.

[3] J. Huang and R. J. Pogorzelski, "A Ka-band microstrip reflectarray with elements having variable rotation angles," *IEEE Trans. Antennas Propag.*, vol. 46, no. 5, pp. 650-656, May 1998.

[4] P. Nayeri, F. Yang, and A. Z. Elsherbeni, "Radiation analysis of reflectarray antennas: array theory approach versus aperture field approach," *presented at the 27th International Review of Progress in Applied Computational Electromagnetics*, Virginia, USA, Mar. 2011.

[5] P. Nayeri, F. Yang, and A. Z. Elsherbeni, "Radiation analysis of reflectarray antennas: numerical approaches versus full-Wave simulations," *presented at the National Radio Science Meeting,* Colorado, USA, Jan. 2012.

[6] B. Devireddy, A. Yu, F. Yang, and A. Z. Elsherbeni, "Gain and bandwidth limitations of reflectarrays," *Appl. Comp. Electro. Society (ACES) Journal*, vol. 26, no. 2, 2011.

[7] S. H. Zainud-Deen, S. M. Gaber, A. M. Abd-Elhady, K. H. Awadalla, and A. A. Kishk, "Perforated dielectric resonator antenna reflectarray," *Appl. Comp. Electro. Society (ACES) Journal*, vol. 26, no. 10, 2011.

[8] M. Arrebola, E. Carrasco, and J. A. Encinar, "Beam scanning antenna using a reflectarray as sub-reflector," *Appl. Comp. Electro. Society (ACES) Journal*, vol. 26, no. 6, 2011.

[9] C. A. Balanis, *Antenna Theory: Analysis and Design*, 3rd Edition, John Wiley & Sons Inc., 2005.

[10] A. Yu, F. Yang, A. Z. Elsherbeni, J. Huang, and Y. Rahmat-Samii, "Aperture efficiency analysis of reflectarray antennas," *Microwave and Optical Technology Lett.*, vol. 52, pp. 364-372, 2010.

[11] Y. Rahmat-Samii, "Reflector Antennas," in *Antenna Handbook: Theory, Applications, and Design*, Y. T. Lo and S. W. Lee, Van Nostrand Reinhold, 1988.

[12] S. D. Targonski and D. M. Pozar, "Minimization of beam squint in microstrip reflectarrays using an offset feed," *presented at the IEEE Antennas and Propagation Society International Symposium*, MD, USA, July 1996.

[13] A. K. Bhattacharyya, *Phased Array Antennas: Floquet Analysis, Synthesis, BFNs, and Active Array Systems*, John Wiley & Sons, 2006.

[14] Ansoft Designer v6.1, ANSYS Inc., 2012.

[15] Matlab v R2011a, MathWorks Co., 2011.

[16] P. D. Potter, "A new horn antenna with suppressed sidelobes and equal beamwidths," *JPL Technical Report,* no. 32-354, 1963.

[17] A. D. Olver, P. J. B. Clarricoats, A. A. Kishk, and L. Shafai, *Microwave Horns and Feeds*, by The Institution of Electrical Engineers, 1994.

[18] FEKO v 6.1, EM Software & Systems Inc., 2012.

[19] J. Robinson and Y. Rahmat-Samii, "Particle swarm optimization in electromagnetics," *IEEE Trans. Antennas Propag.*, vol. 52, no. 2, pp. 397-407, Mar. 2004.

[20] A. Yu, "Microstrip reflectarray antennas: Modeling, design and measurement," Ph.D. dissertation, Department of Electrical Engineering, University of Mississippi, Oxford, MS, 2010.

[21] P. Nayeri, F. Yang, and A. Z. Elsherbeni, "A broadband microstrip reflectarray using sub-wavelength patch elements," *presented at the IEEE Antennas and Propagation Society International Symposium*, SC, USA, June 2009.

Efficient Method of Optimizing Reverberation Chamber Using FDTD and Genetic Algorithm Method

Yao Z. Cui, Guang H. Wei, Song Wang, and Li S. Fan

Institute of Electrostatic and Electromagnetic Protection
Mechanical Engineering College, Shijiazhuang, 050003, China
cuiyaozhongcui@163.com, wei-guanghui@sohu.com, wangsongde@gmail.com, fanlisi@189.cn

Abstract **–** An efficient method combining the finite-difference time-domain (FDTD) method and genetic algorithm (GA) is proposed for the reverberation chamber (RC) optimization. In this method, the GA is utilized to optimize the parameters of RC model built by the FDTD method, such as the stirrer position and stirrer shape. Since the application of GA in the RC optimization and the RC model is automatically varied along with the optimization process, this method improves the accuracy and efficiency of the RC optimization. In addition, the influence of transmitting antenna position on the field uniformity around the lowest usable frequency is also investigated by this method. This method has been verified by comparing with the experiment results.

Index Terms **–** Field uniformity, finite-difference time-domain, genetic algorithm, reverberation chamber, stirrer, and transmitting antenna.

I. INTRODUCTION

The reverberation chamber (RC) is an electrically large and highly conductive enclosed cavity used for electromagnetic compatibility (EMC) measurements. Mechanical stirring is the most common technique used in the RC in order to produce fields that are statistically uniform and isotropic, and is accomplished by using rotating stirrers, which are made up of metal paddles inside the chamber. Consequently, the stirrer plays a key role in defining the RC performance. More precisely, the field uniformity inside the chamber can be enhanced by optimizing the stirrer position and stirrer shape. In [1], the optimization of the stirrer shape is investigated to improve the field uniformity of the RC. In [2, 3], the optimal stirrer position is found by studying the influence of different stirrer positions on the field uniformity of the RC. However, the optimal stirrer shape in [1] is chosen from the finite stirrer shapes given by the authors, and the optimal stirrer position in [2, 3] is chosen in the same way. Thus, since the optimization mechanism is artificial selection, the accuracy of the optimization results is limited, and the really optimal stirrer shape or the stirrer position may not be precise.

In order to improve the optimization accuracy, an efficient RC optimization method is proposed in this paper, which combines the FDTD method with the genetic algorithm (GA). Based on the standard deviation of the electric filed inside the RC, the GA is utilized to optimize the parameters of the RC model built by the FDTD method, such as the stirrer position and stirrer shape; thereby the optimization accuracy is improved. Furthermore, this method makes the RC model automatically varied along with the optimization process, which saves time and workload. In addition, the eigenmode density (number of modes per frequency interval) is low and the performance of the RC is not good when the RC operates around the lowest usable frequency (LUF) [4]. The transmitting antenna position will also slightly affect the performance of the RC, but there is less attention to this point. In this contribution, the influence of transmitting antenna position on the field uniformity around the LUF is also investigated by using our proposed method.

Submitted On: Nov. 14, 2012
Accepted On: Feb. 6, 2013

II. MODELING OF REVERBERATION CHAMBER

Numerical modeling of the RC is a very useful tool to analyze the electric field. The obvious goal of the simulation would be the complete design, evaluation, and optimization of the RC until all target specifications are met prior to physical construction. The RC test systems are designed to cover a broad frequency range. For a broad simulation response, frequency-domain methods, such as the method of moments (MoM) [5, 6] and the finite element method (FEM) [7], are at a disadvantage compared to time-domain methods such as FDTD [8, 9], the finite-volume time-domain (FVTD) [10], and the transmission line matrix (TLM) method [11]. While the latter requires only one simulation run to calculate the field in a large frequency band with the use of a Fourier transform, the former necessitate one simulation at each frequency point.

After evaluating the pros and cons of different numerical methods, we use the 3-D FDTD method as it is suited to the determination of all resonance frequencies and field properties in a frequency band. The RC model in this study is a rectangular cavity with dimensions 10.5 m × 8.0 m × 4.3 m (length × width × height), which is identical with the prototype RC. The first resonance frequency of the RC with this size is 24 MHz, and the LUF can be evaluated by multiplying the first resonance frequency by a constant whose value varies between 3 and 6 [12, 13]. Hence, the LUF of the RC analyzed in this paper is between 72 MHz and 144 MHz. Since the performance of the RC is poor around the LUF, it is of interest to optimize the performance of the RC around the LUF. Therefore, we have chosen to study the frequency band from 80 MHz to 150 MHz. The transmitting antenna model is a log-periodic operating between 60 MHz to 2 GHz, and a Gaussian pulse up to 300 MHz in the frequency domain is excited by this antenna. According to the FDTD principles defined in [14], the space and time increments are set equal to $\Delta h = 0.1$ m and $\Delta t = 1.7\times10^{-10}$ s, respectively (the space step is assumed to be the same for the three directions). In order to reduce the simulation time, an ideal wall is considered and air losses can be used to replace wall losses [8]. For the RC in this paper, the conductivity of the air is $\sigma = 2\times10^{-5}$ S/m obtained from the experimental analysis, and 25,000 time steps are needed to ensure that the FDTD algorithm converges to the steady state. In Fig. 1 the temporal electric field z-component signal ($x = 5.0$ m, $y = 6.9$ m, $z = 2.15$ m) reaches the equilibrium after 25,000 time steps.

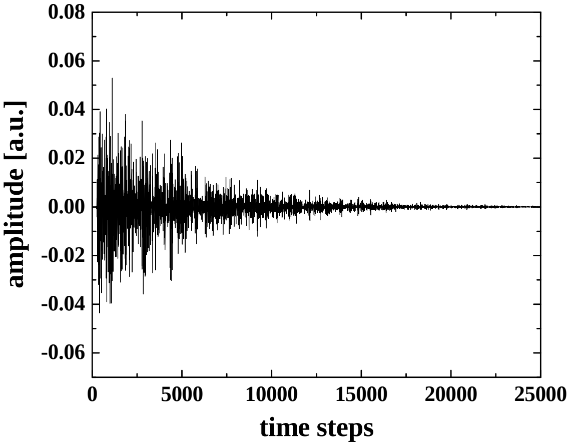

Fig. 1. Temporal electric field z-component signal inside the RC.

Figure 2 shows the internal structure of the prototype RC, with a log-periodic antenna, the horizontal stirrer, and the vertical stirrer. Since fifty angle positions may be required for the lower frequencies according to [15], the model needs to run fifty separate times for each investigated stirrer. The horizontal and vertical stirrers are stepped in fifty positions (10 × 5) in interleaved mode in this paper.

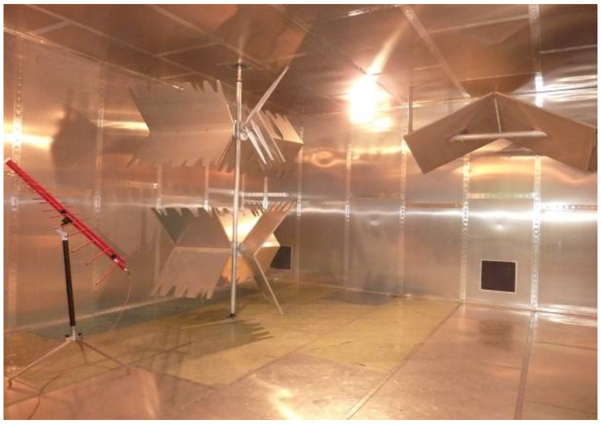

Fig. 2. Photo of the reverberation chamber prototype, showing a part of the horizontal stirrer on the right, the vertical stirrer, and a log-periodic transmitting antenna.

III. OPTIMIZATION PROCESS

Many empirical criteria and the classical statistical laws characterizing the RC electrical behavior have been proposed to ensure satisfactory functioning of the RC [16-20]. The standard deviation measurement is usually used to evaluate the field uniformity [15, 19]. In this case, the standard deviation σ_r (with $r = x, y, z$) of the eight maximal values over a stirrer rotation of each field component ($E_{r\max}$) calculated at eight points within the working volume, and the standard deviation σ_{24} of $E_{r\max}$ of three field components (24 values) are calculated, respectively (a more detailed presentation of calculating the standard deviation can be found in [15]). According to the norm IEC61000-4-21 [15], the smaller the standard deviation is, the better the field uniformity is. Furthermore, the σ is much easier to be used to evaluate the performance of the RC, since comparing several sets of graphs by eye, such as those depicted in Fig. 3, is very difficult. Hence, the σ_x, σ_y, σ_z and σ_{24} are taken as the objective functions, and the σ is defined as the average standard deviation over frequencies 80 MHz – 150 MHz in this paper.

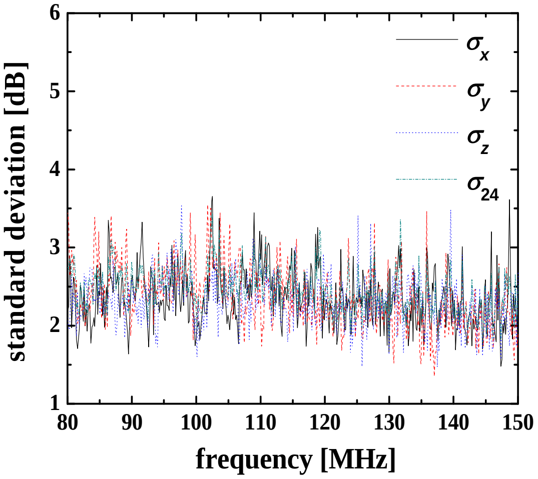

Fig. 3. Standard deviation of the RC model.

By letting the fitness function $F = \sigma_x + \sigma_y + \sigma_z + \sigma_{24}$, the multi-objective optimization problem becomes a single-object problem. Again, the field uniformity is getting better with the decrease of F. The GA is used to optimize the field uniformity of the RC model. The specific optimization process is as follows: (1) Generating an initial population of the optimization variables defining the transmitting antenna position (the stirrers shape or the stirrer position). The population size is 30. (2) Every individual of the optimization variable is assigned to the RC model, and the model is calculated by the FDTD method. (3) Calculating the fitness function F. (4) Selection takes place, where a stochastic universal sampling (SUS) is applied to select the quality individuals. (5) Crossover is followed, where a uniform crossover is applied to make individuals matched pairs in a crossover probability P_c that is 0.8. (6) Mutation, Gaussian mutation is applied to make the selected individuals stochastically vary gene in a mutation probability P_m that is 0.1. (7) The condition of termination; if the generation t is less than the maximum generation 30, program jumps to step number (2), or else the individual with the minimum fitness is exported.

It should be noted that the RC model is automatically modified by the program after the optimization variable is assigned to the RC model, which saves time and workload.

IV. OPTIMIZATION RESULTS

The transmitting antenna position, the stirrer shape, and the stirrer position are optimized by using our proposed method, respectively. The optimization variable is set as follows: (1) The coordinates of the transmitting antenna tail $x = a$, $y = b$, $z = c$, are the optimization variables when the antenna position is optimized, as shown in Fig. 4. (2) The angle φ and θ between the paddles are the optimization variables when the stirrer shape is optimized, as shown in Fig. 4. (3) The distance d_1 between the horizontal stirrer and the right wall of the chamber is the optimization variable when the stirrer position is optimized, as shown in Fig. 5 (N.B. the reason why the horizontal stirrer position is only optimized is that the vertical stirrer takes too much space and has to keep a distance from the transmitting antenna, so the range of the vertical stirrer position is small). (4) The a, b, c, φ, θ, and d_1 are the optimization variables when the global RC is optimized.

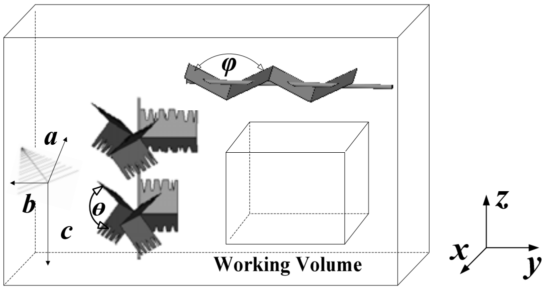

Fig. 4. Drawing of the RC model showing the horizontal stirrer with 'V' angle φ on the right, the vertical stirrer on the left with '<' angle θ and the transmitting antenna. The $x = a$, $y = b$, $z = c$, are the coordinates of the transmitting antenna tail. The working volume is $x \in [2.9, 7.0]$; $y \in [4.3, 9.5]$; $z \in [1.0, 3.3]$.

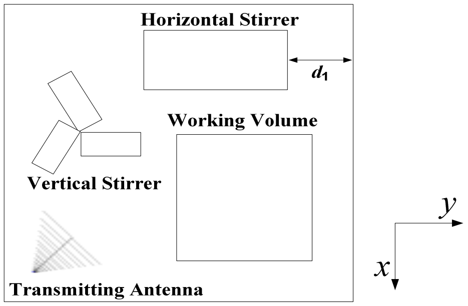

Fig. 5. Platform of the RC model, where d_1 is the distance between the horizontal stirrer and the right wall of the chamber.

Table 1 contains the optimal values of the optimization variables. From Table 1, it can be seen that the optimal values of the optimization variables when optimizing the global chamber are different from the optimal values when optimizing the transmitting antenna position, the stirrer shape and the stirrer position independently, which shows that the optimal values of these parameters are interactional.

It is well known that the stirrer shape and the stirrer position affect the field uniformity of the RC. However, as shown in Fig. 6, the transmitting antenna position also affects the field uniformity around the LUF, but relatively slightly compared with the stirrer shape and the stirrer position.

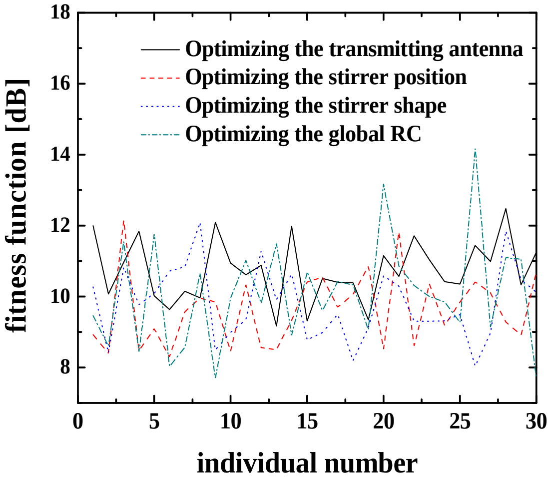

Fig. 6. Fitness functions versus individual number of the first generation.

Table 2 shows the optimization results. The results in Table 2 verify that the optimization improves the field uniformity of RC, but the improvement is small by optimizing the transmitting antenna position, and a much greater improvement in field uniformity is achieved by optimizing the stirrer position or the stirrer shape, which shows that the field distribution inside the RC is more sensitive to the stirrer.

Table 1: Optimal and initial values of the optimization variables.

	***a*/m**	***b*/m**	***c*/m**	**d_1/m**	**φ/°**	**θ/°**
Initial	5.72	2.20	1.13	1.20	128.30	90.00
Optimal antenna position	6.43	2.43	1.87	—	—	—
Optimal stirrer position	—	—	—	4.25	—	—
Optimal stirrer shape	—	—	—	—	168.23	146.54
Optimal the global RC	6.35	2.26	2.08	3.33	127.48	161.62

Table 2: Optimization results.

	σ_x/dB	σ_y/dB	σ_z/dB	σ_{24}/dB	F/dB
Initial	2.35	2.37	2.30	2.46	9.48
Optimal antenna position	2.33	2.31	2.27	2.32	9.23
Optimal stirrer position	2.19	2.21	2.17	2.17	8.74
Optimal stirrer shape	2.16	2.15	2.14	2.18	8.63
Optimal the global RC	2.09	2.07	2.10	2.12	8.38

V. VERIFICATION OF THE OPTIMIZATION METHOD

The optimization method is verified by optimizing the transmitting antenna position to save the experiment resource. The field uniformity of the RC (see Fig. 1) is measured separately when the transmitting antenna is at initial and optimal positions. The horizontal and vertical stirrers are moved in 10 × 5 positions, in interleaved mode, using a stepper motor that is controlled by computer software. An optical fiber transmission field strength meter EMR-200 produced by Narda STS is used to measure the electric fields at the eight positions within the working volume.

Table 3 shows the standard deviation obtained from the measurement data for both the optimal and the initial position of the transmitting antenna. There is an improvement of 0.17 in the value of F between the optimal and the initial transmitting antenna position, which shows that the optimization does improve the field uniformity of the RC although, the modeled optimization results predicted a slightly larger improvement of 0.25 (see Table 2). The differences between the simulation and experiment results can be explained by the numerical dispersion of the FDTD scheme. Moreover, the differences could be reduced by using a more accurate mesh.

In addition, from the optimization results separately obtained by experiment and simulation (see Tables 2 and 3), we can note that, although the optimization does improve the RC's performance, the margin of improvement is not excessive by modifying only those six parameters (a, b, c, d_1, φ, and θ), especially the transmitting antenna position. Using this optimization method proposed in this paper, a much greater improvement in performance could be achieved by modifying more complex parameters that affect the design of the stirrer, rather than keeping the basic shape the same and searching for the best angles.

Table 3: Optimal and initial transmitting antenna position measurement results.

	σ_x/dB	σ_y/dB	σ_z/dB	σ_{24}/dB	F/dB
Initial	2.23	2.27	2.19	2.30	8.99
Optimal	2.17	2.18	2.23	2.24	8.82

VI. CONCLUSION

By applying the GA in the RC optimization design, an efficient RC optimization method is presented which improves the RC optimization accuracy and saves time and workload. Measurements have been performed to verify that the optimization within the GA does actually produce an improvement within a real chamber. The optimization results of simulation and experiment show that the field uniformity of the RC has been improved by optimizing the transmitting antenna position, the stirrer shape and the stirrer position, and the improvement obtained by optimizing the stirrer is larger compared with optimizing the transmitting antenna position.

Although the optimization does improve the RC's performance, the improvement is small by modifying only those six simple parameters (a, b, c, d_1, φ, and θ). As we all know, the larger the rotation volume of stirrer and the more complex the stirrer structure, the better the RC's performance. Consequently, in the future work, on the basis of the constant working volume, some more complex parameters that affect the design of the stirrer (e.g., the rotation volume and structure of the stirrer) could be optimized by using the optimization method proposed in this paper, instead of keeping the basic shape the same and searching for the best angles.

In addition, since the performance of the RC is poor around the LUF, the performance of the RC around the LUF (from 80 MHz to 150 MHz) is investigated in this paper. When the RC operates around the higher frequency of the RC, the RC's performance will also be improved by optimization, but the improvement will be relatively small since the eigenmode density is high and the RC's performance is inherently good at high frequency. Consequently, it is of small significance to optimize the RC at high frequency.

REFERENCES

[1] J. I. Hong and C. S. Huh, "Optimization of stirrer with various parameters in reverberation chamber," *Progress In Electromagnetic Research*, vol. 104, pp. 15-30, 2010.

[2] L. Bai, L. Wang, B. Wang, and J. Song, "Effects of paddle configurations on the uniformity of the reverberation chamber," *IEEE Int. Symp. Electromagnetic Compatibility*, Seattle, WA, pp. 12-16, 1999.

[3] D. Zhang and J. Song, "Impact of stirrers' position on the properties of a reverberation chamber with two stirrers," *IEEE Int. Symp. Electromagnetic Compatibility*, Washington, DC, pp. 7-10, 2000.

[4] M. L. Crawford and G. H. Koepke, "Design, evaluation and use of a reverberation chamber for performing electromagnetic susceptibility /vulnerability measurements," *NBS Technical note 1092*, 1986.

[5] G. Freyer, T. Lehman, J. Ladbury, G. Koepke, and M. Hatfield, "Verification of fields applied to an EUT in a reverberation chamber using statistical theory," *IEEE Int. Symp. Electromagnetic Compatibility*, Denver, CO, pp. 34-38, 1998.

[6] C. Bruns and R. Vahldieck, "A closer look at reverberation chambers-3-D simulation and experimental verification," *IEEE Trans. Electromagn. Compat.*, vol. 47, no. 3, pp. 612-626, 2005.

[7] C. F. Bunting, "Statistical characterization and the simulation of a reverberation chamber using finite-element techniques," *IEEE Trans. Electromagn. Compat.*, vol. 44, no. 1, pp. 214-221, 2002.

[8] F. Moglie and V. M. Primiani, "Reverberation chambers: Full 3D FDTD simulations and measurements of independent positions of the stirrers," *IEEE Int. Symp. Electromagnetic Compatibility*, Rome,Italy, pp. 226-230, 2011.

[9] G. Orjubin, F. Petit, E. Richalot, S. Mengue, and O. Picon, "Cavity losses modeling using lossless FDTD method," *IEEE Trans. Electromagn. Compat.*, vol. 48, no. 2, pp. 429-431, 2006.

[10] F. Paladian, F. Diouf, S. Girard, P. Bonnet, and S. Lallechere, "Evaluation of FVTD dissipation and time-domain hybridization for MSRC studies," *23rd Annual Review of Progress in Applied Computational Electromagnetics (ACES)*, Verona, Italy, March 2007.

[11] A. Coates, H. G. Sasse, D. E. Coleby, A. P. Duffy, and A. Orlandi, "Validation of a three-dimensional transmission line matrix (TLM) model implementation of a mode-stirred reverberation chamber," *IEEE Trans. Electromagn. Compat.*, vol. 49, no. 4, pp. 734-744, 2007.

[12] M. Hatfield, M. Slocum, E. Godfrey, and G. Freyer, "Investigations to extend the lower frequency limit of reverberation chambers," *IEEE Int. Symp. Electromagnetic Compatibility*, Denver, CO, pp. 20-23, 1998.

[13] A. K. Mitra and T. F. Trost, "Statistical simulations and measurements inside a microwave reverberation chamber," *IEEE Int. Symp. Electromagnetic Compatibility*, Austin, TX, pp. 48-53, 1997.

[14] A. F. Peterson, S. L. Ray, and R. Mittra, *Computational Methods for Electromagnetics*, IEEE Press New York, 1998.

[15] *Electromagnetic Compatibility (EMC) - Part 4-21: Testing and measurement techniques - Reverberation Chamber Test Methods*, International Electrotechincal Commission, IEC61000-4-21 Draft, 2003.

[16] F. Moglie and V. M. Primiani, "Analysis of the independent positions of reverberation chamber stirrers as a function of their operating conditions," *IEEE Trans. Electromagn. Compat.*, vol. 53, no. 2, pp. 288-295, 2011.

[17] S. Mengué, E. Richalot, and O. Picon, "Comparison between different criteria for evaluating reverberation chamber functioning using a 3-D FDTD algorithm," *IEEE Trans. Electromagn. Compat.*, vol. 50, no. 2, pp. 237-245, 2008.

[18] C. Lemoine, P. Besnier, and M. Drissi, "Investigation of reverberation chamber measurements through high-power goodness-of-fit tests," *IEEE Trans. Electromagn. Compat.*, vol. 49, no. 4, pp. 745-755, 2007.

[19] N. Kouveliotis, P. Trakadas, and C. Capsalis, "Examination of field uniformity in vibrating intrinsic reverberation chamber using the FDTD method," *Electronics Lett.*, vol. 38, no. 3, pp. 109-110, 2002.

[20] D. A. Hill, “Plane wave integral representation for fields in reverberation chambers,” *IEEE Trans. Electromagn. Compat.*, vol. 40, no. 3, pp. 209-217, 1998.

Yaozhong Cui was born in Hebei province, China, in 1986. He received the B.Eng. from Xidian University, Shanxi, China, in 2008, the M.Eng. from Mechanical Engineering College, Shijiazhuang, China, in 2010. He is currently working toward the Ph.D. degree at Mechanical Engineering College, Shijiazhuang, China. His research interests include computational electromagnetic and electromagnetic measurement in reverberation chamber.

Guanghui Wei was born in Hebei province, China, in 1964. He received the B.Sc. and the M. Sc. Degree from Nankai University, Tianjin, China in 1984 and 1987, respectively. He is Professor of Institute of Electrostatic and Electromagnetic Protection at the Mechanical Engineering College. His research interests include computational electromagnetic, EMC test environments and EMC measurement techniques.

Song Wang was born in Hebei province, China, in 1987. He received the B.Sc. from Beihang University, Beijing, China, in 2010. He is currently working toward the Ph.D. degree at Mechanical Engineering College, Shijiazhuang, China. His research interests include computational electromagnetic and electromagnetic measurement in reverberation chamber.

Three New Rat-Race Couplers with Defected Microstrip and Ground Structure (DMGS)

Ma. Shirazi [1], R. Sarraf Shirazi [1], Gh. Moradi [1], and Mo. Shirazi [2]

[1] Microwave Measurement Lab., Department of Electrical Engineering,
Amirkabir University of Technology, Tehran, 158754413, Iran
Mahmoudshirazi@aut.ac.ir, Sarraf@aut.ac.ir, Ghmoradi@aut.ac.ir

[2] Digital Communication Research Lab., Department of Electrical Engineering,
Amirkabir University of Technology, Tehran, 158754413, Iran
Mojtabashirazi@aut.ac.ir

Abstract **─** In this paper, three new types of rat-race ring couplers with defected microstrip and ground structure (DMGS) are presented and one type is fabricated to validate the simulation results. The proposed structures have the advantages of size reduction as well as 3rd harmonic suppression. Embedding the DMGS section increases the slow-wave factor (SWF) and as a result the resonant frequency of the coupler decreases, which sets the stage for size reduction. In addition, insertion losses of the 3rd harmonic of the proposed couplers are reduced to 35 dB. After optimizing with genetic algorithm (GA), one type is fabricated. Good agreement between the simulation and measurement results is observed. Simulations are carried out using HFSS 13 and the designed coupler is validated by measurement.

Index Terms – Defect on microstrip, defect on ground, DMGS, and hybrid ring rat-race coupler.

I. INTRODUCTION

Microstrip rat-race ring couplers are important structures in microwave engineering. Among all couplers, rat-race couplers are widely used due to their simplicity and wide bandwidth in dividing power. They are used in power amplifiers, mixers, and antenna systems [1]. Hybrid ring couplers are also used in isolated power dividers where high level of isolation between the ports is required. However, this isolation is generally limited in bandwidth by the phase balance performance of the hybrid. The conventional 180º hybrid ring coupler has several shortcomings. It is inherently narrow band, large in size, and it requires impractically high impedance line sections for large power-split ratios. Therefore, many techniques have been proposed to improve the frequency characteristic of rat-race couplers and attempts are continually made to reduce their size, suppress their spurious harmonics, increase their bandwidth, and make a dual band coupler [2, 3].

Wireless communication systems usually require smaller device size in order to meet circuit miniaturization and cost reduction. Thus, size reduction is becoming a major design consideration for practical applications. However, in the low microwave frequency range, even a small size conventional hybrid coupler is still too large for some applications. Therefore, reduced size couplers are continually proposed for MMIC (Monolithic Microwave Integrated Circuit) applications [3-7].

Recently, there has been an increasing interest in microwave and millimeter-wave applications of the PBG (photonic band gap) [5, 6] and the DGS (defected ground structure) [2, 7-9]. In the case of 2-dimensional PBG structure [5], a lot of PBG cells increase the circuit size, which leads to feedline losses. Also, the slow-wave effect in [5] is sensitive to the location and direction of the line with respect to the principal axes of the periodic defected holes on the ground. In [7] a rat-race coupler with DGS sections has been proposed that is not optimum neither in size nor in shape. In

Submitted On: Sept. 30, 2012
Accepted On: Feb. 6, 2013

1054-4887 © 2013 ACES

addition, several defected microstrip structures (DMS) have been proposed for suppression of spurious responses in the microstrip filters [10-12]. In this paper, we apply the novel idea of embedding defects on the strip and ground plane of a rat-race coupler, simultaneously. As a result we achieve the goal of very small size coupler as well as deep suppression of third harmonic signal that are very important in the MMIC applications. For all proposed structures, the used substrate is of relative dielectric constant equal to 3.55 and thickness of 31 mil.

II. MICROSTRIP LINE WITH DMGS SECTION

Figure 1 shows a microstrip line with DMGS section and S-parameters of the line. The width and length of the microstrip line are 3 mm and 16.65 mm, respectively. As shown in Fig. 1 (b), these lines with DMGS section acts as a lowpass filter [10]. Therefore, the DMGS can be modeled with an RLC circuit and the circuit parameters are achieved according to equation (1).

$$L=\frac{1}{4\pi^2 f_0^2 C}mH, C=\frac{f_c}{2Z_0}\cdot\frac{1}{2\pi(f_0^2-f_c^2)}nf$$

$$R=\frac{2Z_0}{\sqrt{\frac{1}{|S_{11}(\omega)|^2}-(2Z_0(\omega C-\frac{1}{\omega L}))^2-1}}, \qquad (1)$$

in which f_0 and f_c are the attenuation pole and cut-off frequencies, respectively. From Fig. 1 (b) it is seen that the microstrip line with DMGS has a cut-off frequency at 1.07 GHz and an attenuation pole at 7.4 GHz. The parameters of defects on the microstrip and ground plane are: u = 8 mm, v = 1.2 mm, c = 1.5 mm, a = 5 mm, b = 5 mm and the narrow gap distance is g = 0.2 mm.

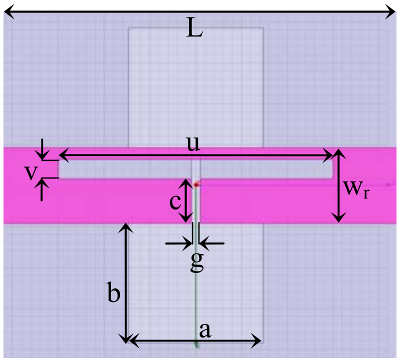

(a)

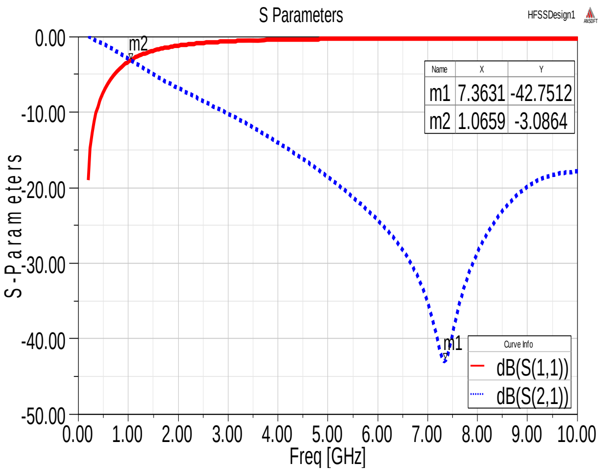

(b)

Fig. 1. Configuration of the microstrip line with DMGS: (a) parameters of microstrip line with DMGS and (b) the return loss (solid line) and insertion loss (dotted line) of the microstrip line with the DMGS section.

To compare the effect of three types of defects on the phase response of a microstrip line, we simulate four different types of microstrip lines: the conventional microstrip line, microstrip line with DGS section, line with DMS section and line with DMGS section in Fig. 2. As shown by Fig. 2, the frequency at which the phase of S21 becomes -90° is different for each type of defect. Fig. 2 illustrates that the line with the DMGS sections has the most effect on the phase of a microstrip line and reduces the resonant frequency from 2.1 GHz to 1.12 GHz. This decrease in the resonant frequency of the microatrip line with DMGS is due to the slow-wave effect. In fact, embedding a defect on a microstrip line changes the inductance and capacitance of the line and subsequently the resonant frequency of the line. The effect of embedding a DMGS section on the inductance of the line is much more than other types of defects. Furthermore, according to (1), the increase in the inductance of the microstrip line results in decrease in the resonant frequency of the line. Note that we use this property of the DMGS, which affects the phase of microstrip line, to reduce the size of rat-race coupler, as well as to suppress the 3rd harmonic signal.

III. THREE TYPES OF RAT-RACE COUPLERS WITH DMGS SECTIONS

The shapes of the proposed couplers have been illustrated in Figs. 3, 6, and 8. For each proposed coupler, six DMGS sections are used and the DGS sections are exactly under the DMS sections.

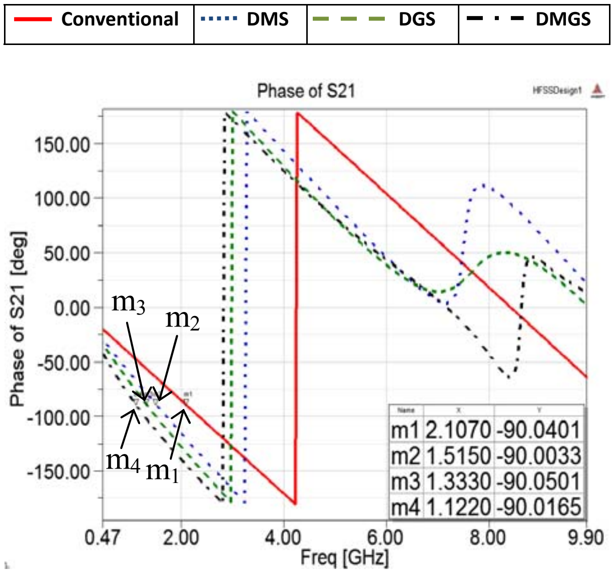

Fig. 2. Phase of the S21 for the conventional microstrip line (red solid line), microstrip line with DMS (blue dotted line), microstrip line with DGS (green dashed line), and microstrip line with DMGS (black dotted-dashed line).

A. Rat-race coupler α

The coupler α is shown in Fig. 3. We use GA as the optimization method [13, 14]. The properties of the substrate as well as the coupler dimensions remain unchanged during the optimization. Dimensions of the defects and the width of the strip line are optimized using GA. The optimum parameters of this type of coupler are obtained as u = 7 mm, v = 1.7 mm, c = 1.5 mm, g = 0.2 mm, a = 4 mm, b = 7.5 mm, and W_r = 4 mm. The simulated S-parameters of the proposed coupler α have been depicted in Fig. 4. For comparison, we simulated a conventional coupler and the simulated results have been shown in Fig. 5.

As shown in Figs. 4 and 5, the central frequency of coupler α has been lowered from 2.7 GHz to 1.35 GHz. The central frequency of the proposed coupler is half that of the conventional coupler (1.35/2.7). Therefore, the wavelength in coupler α is twice the wavelength in the conventional coupler. Due to direct relation between wavelength and the perimeter of the ring ($P = 6\lambda/4$), the perimeter and radius of the ring of coupler α are twice the perimeter and radius of the conventional coupler, respectively. Hence, the occupation area of coupler α is 0.25 that of the conventional one. In other words, the proposed coupler with central frequency 1.35 GHz acts as the conventional coupler with central frequency 1.35 GHz, but the proposed coupler α is 75 % smaller than the other one (note that the conventional rat-race coupler with central frequency 1.35 GHz is four times larger in size than the conventional coupler with central frequency 2.7 GHz). Additionally, Fig. 4 shows that the 3rd harmonic of the conventional rat-race coupler has been suppressed to more than 35 dB.

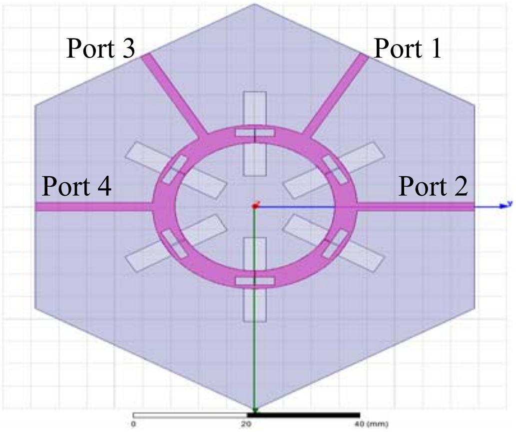

Fig. 3. Configuration of the proposed rat-race ring couplers α.

The S-parameters of the conventional rat-race coupler in Fig. 5 show strong passband near the 3rd harmonic frequencies, which has a bad effect on the overall performance of the RF systems. Therefore, a lowpass or bandpass filter is required to lessen the effect of the spurious signal, which leads to an increase in the insertion loss and RF front-end size. In the proposed coupler, there is no need to insert any filter because it rejects harmonics intrinsically, and as a result the performance of the overall system will be improved.

The bandwidth of the conventional rat-race coupler is 15.9 % at 2.7 GHz. For the proposed coupler, the bandwidth is 13.7 % at 1.35 GHz. Therefore, the new coupler has just 2 % narrower bandwidth than the conventional rat-race coupler. Return loss and isolation between input and output ports of the proposed coupler α, in the bandwidth, are less than -20 dB and the insertion losses are better than -3.4 dB. In addition, phase and amplitude imbalance of the coupler α are better than 1 dB and 5^0, respectively.

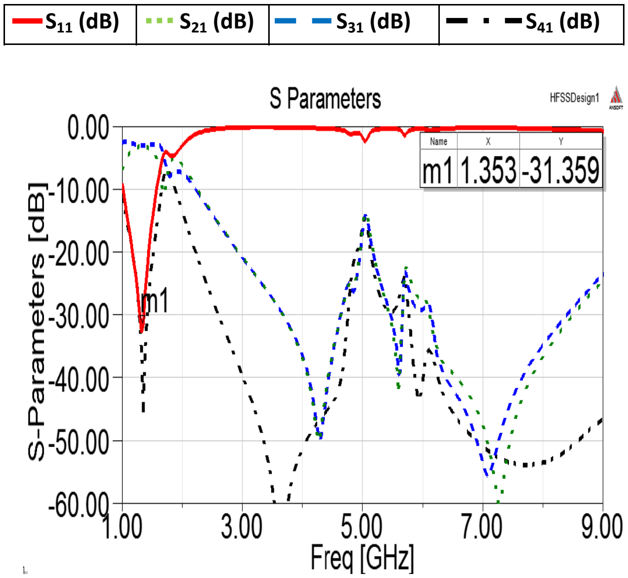

Fig. 4. Simulated S-parameters of the proposed rat-race coupler α.

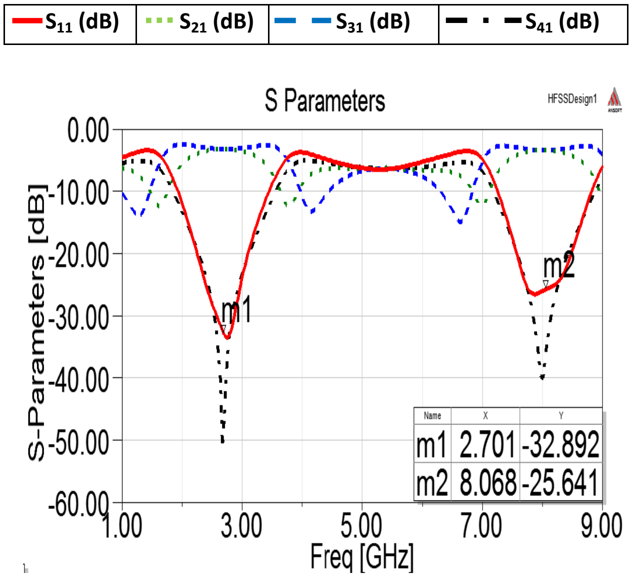

Fig. 5. Simulated S-parameters of the conventional rat-race coupler.

B. Rat-race coupler β

The schematic view of the proposed coupler β has been shown in Fig. 6. We used fractal DGS and T-shape DMS sections in this type of coupler. After optimization with GA, we obtained the optimum values as u = 8 mm, v = 1.5 mm, c = 1.5 mm, g = 0.2 mm, a = 5.5 mm, b = 7.5 mm, and W_r = 4 mm.

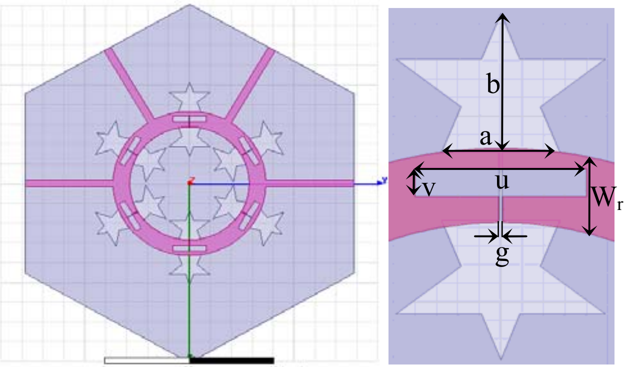

(a) (b)

Fig. 6. The proposed rat-race ring coupler β. (a) Configuration of the coupler β and (b) the parameters of the coupler β.

Figure 7 shows the S-parameters of coupler β. Central frequency has been reduced to 1.32 GHz, hence the size of the proposed coupler β is 0.239 that of conventional coupler (note to the procedure followed in section III A for coupler α). In one hand, the occupation area of coupler β is 4.6 % less than that of coupler α and it has wider bandwidth as well. On the other hand, coupler β has more return loss and less suppression of the 3^{rd} harmonic in comparison to coupler α.

C. Rat-race coupler γ

The coupler γ has been shown in Fig. 8. In [12] a spiral defected microstrip structure is proposed to make a dual band microstrip antenna. We use this type of defect on the microstrip ring line of a rat-race coupler with dumbell-shape DGS. The width of the ring is chosen to be W_r = 4 mm. The optimum parameters of the coupler γ are w1 = 0.5 mm, L1 = 10.5 mm, w2 = 0.8 mm, L2 = 11 mm, w3 = 0.4 mm, L3 = 1.1 mm, a = 5 mm, b = 8.5 mm, and g = 0.2 mm.

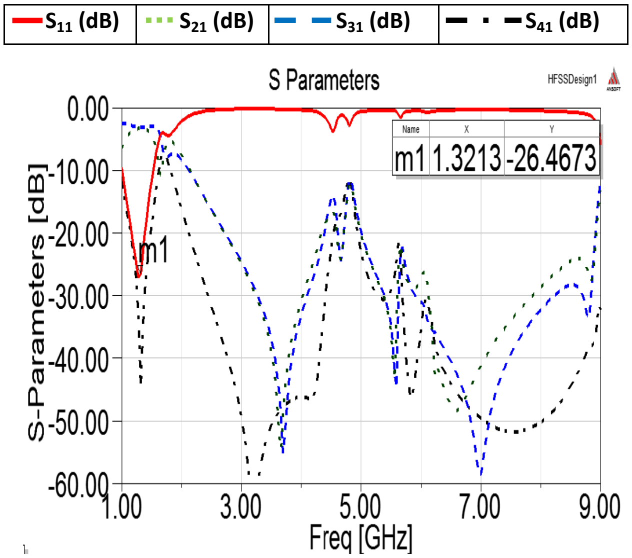

Fig. 7. Simulated S-parameters of the proposed rat-race coupler β.

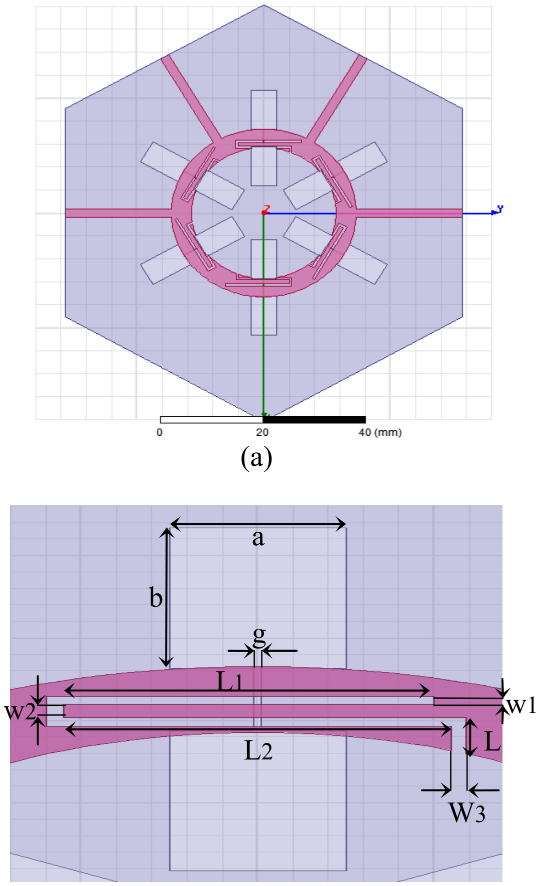

(a)

(b)

Fig. 8. The proposed rat-race ring coupler γ. (a) Configuration of coupler γ and b) parameters of coupler γ.

The S-parameters of coupler γ are depicted in Fig. 9. It is evident that the central frequency of coupler γ has been reduced to 1.29 GHz. Therefore, coupler γ decreases the occupation area by 77.1 % in comparoison to the conventional rat-race coupler. Coupler γ has smaller size, but it has weak response in suppressing the 3rd harmonic. In other words, unlike the two previous couplers, coupler γ can not suppress spurios harmonics.

Table 1 shows the advantages and disadvantages of the three new proposed couplers relative to the conventional coupler. Size, bandwidth, and the ability of coupler to suppress the third harmonic are compared in Table 1.

Table 1: Properties of the three proposed couplers.

Type of coupler	**Size**	**Suppression of 3rd harmonic**	**Bandwidth**
Conventional coupler	1	No	15.9%
Coupler α	0.25	35dB	13.7%
Coupler β	0.239	25dB	14.3%
Coupler γ	0.228	5dB	15%

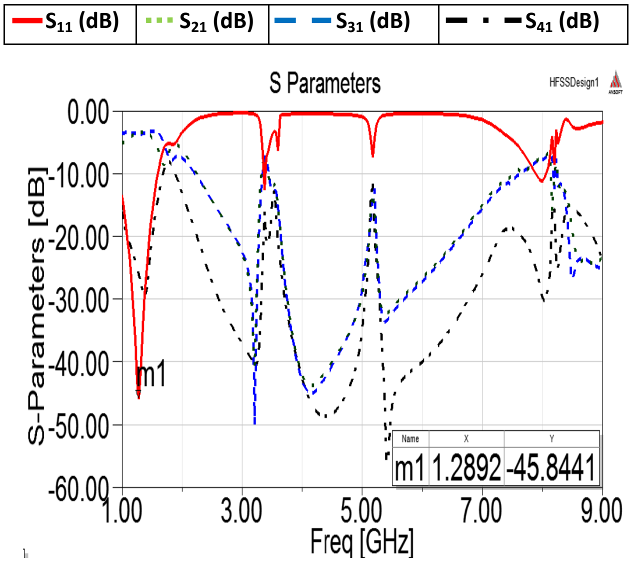

Fig. 9. Simulated S-parameters of the proposed rat-race coupler γ.

IV. EXPERIMENTAL RESULTS

To validate our novel idea, a rat-race coupler with DMGS sections has been fabricated and measured based on the optimum values we obtained from the simulations. Figure 10 shows the top and bottom view of the fabricated new coupler. Measurement of the fabricated coupler has been carried out with R&S ZVB vector network analyzer.

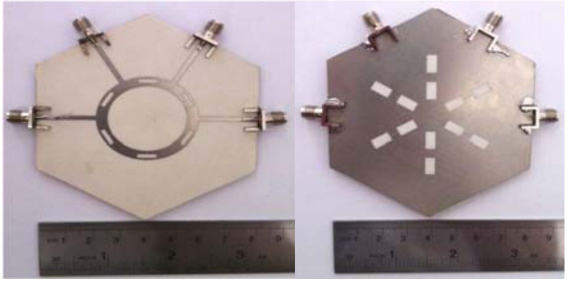

(a) (b)

Fig. 10. Fabricated rat-race coupler with DMGS sections, (a) top view and (b) bottom view.

The measured S-parameters of the fabricated coupler have been shown in Figs. 11 and 12. Simulated and measured return loss and insertion loss between ports 1 and 2 are depicted in Fig. 11 (a), simultaneously. Simulated and measured isolation between ports 1 and 4 as well as insertion loss between ports 1 and 3 are shown in Fig. 11 (b). First, the insertion loss of the proposed coupler (S_{21}, S_{31}) is -3.8 dB around central frequency. There is always 0.3 dB to 0.5 dB loss due to the connectors. Without considering connector losses, the insertion loss of coupler is almost -3.4 dB around the central frequency that concedes the simulation results. Additionally, as shown by Fig. 11, insertion losses are less than -30 dB around the 3rd harmonic frequencies. Deep insertion loss ensures us about suppressing the 3rd harmonic signal. Finally, in Fig. 11 (a), it is obvious that the central frequency of the new coupler has been lowered to 1.35 GHz. Based on very good agreement between simulations and measurements of coupler α, it is evident that all simulation results for all the three proposed couplers are completely reliable.

To ensure the phase balance of the output signals, the phase difference between output ports (phase of S_{21} minus phase of S_{31}) has been depicted in Fig. 12. Good agreement between simulation and measurement, especially in the bandwidth, is obtained and this will again validate the simulated results. It is seen that around the central frequency of the proposed coupler, phase difference between the output ports is less than 5 degrees.

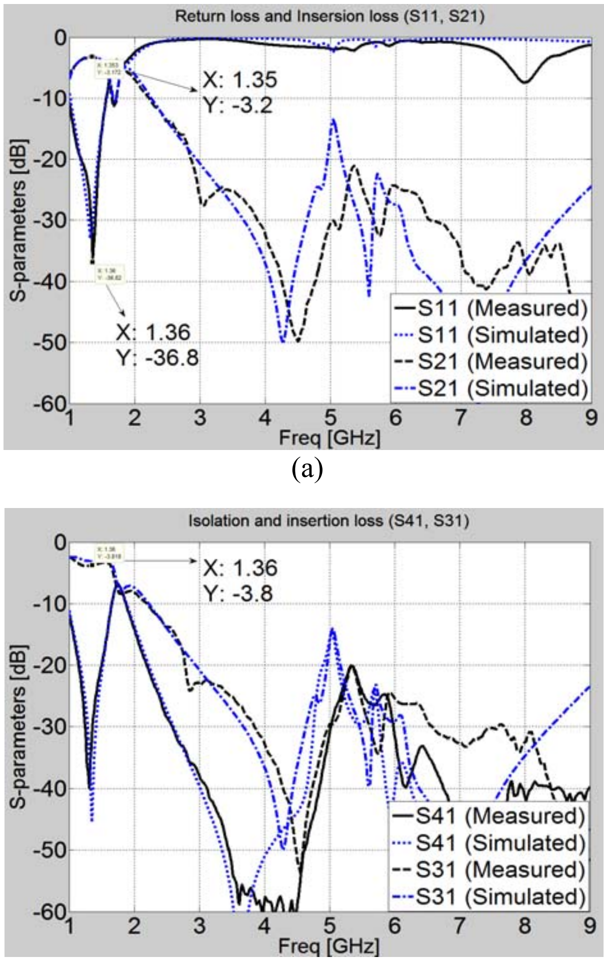

(a)

(b)

Fig. 11. Measured S-Parameters of the fabricated coupler, (a) simulated and measured S_{11} and S_{21} and (b) simulated and measured S_{41} and S_{31}.

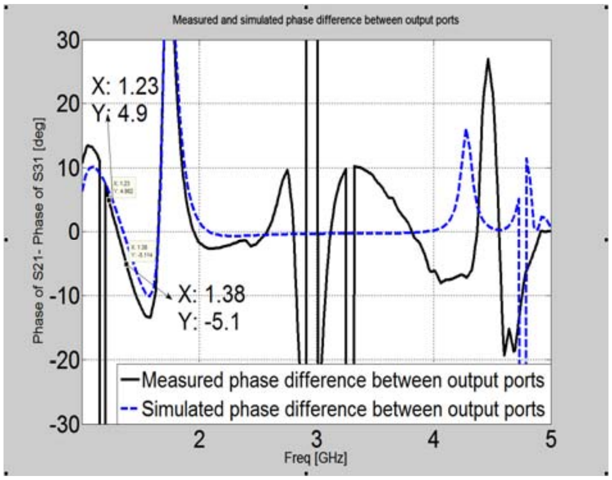

Fig. 12. Simulated and measured phase difference between output ports of the fabricated coupler.

V. CONCLUSION

In this paper, three new miniaturized rat-race couplers having harmonic suppression have been expressed. First, a microstrip line with DMGS section was examined, and then new couplers with DMGS sections were simulated. Finally, one type of the proposed couplers was fabricated and measured. The optimum parameters for all three couplers have been obtained using GA. In the proposed couplers, the central frequency has been lowered significantly and the 3rd harmonic has been suppressed to more than 30 dB. Due to compactness, low cost, and harmonic suppression, rat-race couplers with DMGS sections may be used widely in microwave and millimeter-wave integrated circuits.

ACKNOWLEDGMENT

The authors would like to sincerely acknowledge the institute of Iran Telecommunication Research Center (ITRC) for their financial support.

REFERENCES

[1] D. M. Pozar, *Microwave Engineering*, New York: Wiley, 1998.

[2] A. S. Al-Zayed, Z. M. Hehjazi, and A. S. Mohra, “A microstrip directional coupler with tight coupling and relatively wideband using defected ground structure,” *Appl. Comp. Electro. Society (ACES) Journal*, vol. 25, no. 10, pp. 877-887, Oct. 2010.

[3] H. –X. Xu, G. –M. Wang, and K. Lu, “Microstrip rat-race couplers,” *IEEE Microwave Magazine*, pp. 117-129, June 2011.

[4] A. Mohra, A. F. Sheta, and S. F. Mahmoud, “New compact 3 dB 0°/180° microstrip coupler configurations,” *Appl. Comp. Electro. Society (ACES) Journal*, vol. 19, no. 2, pp. 108-112, July 2004.

[5] C. Caloz and T. Itoh, “Multilayer and anisotropic planar compact PBG structures for microstrip applications,” *IEEE Trans. Microwave Theory Tech.*, vol. 50, pp. 2206-2208, Sept. 2002.

[6] F. R. Yang, Y. Qian, and T. Itoh, “A novel uniplanar compact PBG structures for filter and mixer applications,” *IEEE Microwave Theory and Tech. Symp.*, pp. 919-922, 1999.

[7] Y. J. Sung, C. S. Ahn, and Y. S. Kim, “Size reduction and harmonic suppression of rat-race hybrid ring coupler using defected ground structure,” *IEEE Microwave Wireless Comp. Lett.*, vol. 14, no. 1, pp. 7-9, Jan. 2004.

[8] M. Shirazi, R. Sarrafshirazi, and G. Moradi, “Optimized rat-race coupler with different shapes of defected ground structure,” *PIERS Conference*, Moscow, RUSSIA, pp. 849-852, 19-23 August 2012.

[9] J. S. Park, J. Kim, J. Lee, and S. Myung, “A novel equivalent circuit and modeling method for defected ground structure and its application to optimization of a DGS low-pass filter,” *IEEE Microwave Theory and Tech. Symp.*, pp. 417-420, 2002.

[10] M. Kazerooni, A. Cheldavi, and M. Kamarei, “A novel bandpass defected microstrip structure (DMS) filter for planar circuits,” *PIERS Proceeding,* Moscow, Russia, pp. 1214-1217, 18-21 August 2009.

[11] S. Fallahzadeh, H. Bahrami, A. Akbarzadeh, and M. Tayarani, “High-isolation dual-frequency operation patch antenna using spiral defected microstrip structure,” *IEEE Antennas and Wireless Propagation Letters,* vol. 9, pp. 122-124, 2010.

[12] M. Shirazi, R. Sarrafshirazi, Gh. Moradi, and S. Shirazi, “Size reduction and harmonic suppression of a rat-race coupler with different Types of defected microstrip structure (DMS),” *20th Telecommunications Forum TELFOR*, SAVA Center, Belgrade, Serbia, 20-22 November, 2012.

[13] R. L. Haupt and D. H. Werner, *Genetic Algorithms in Electromagnetics*, IEEE Press/Wiley Interscience Publication, 2007.

[14] M. –I. Lai and S. –K. Jeng, “Compact microstrip dual-band bandpass filters design using genetic-algorithm techniques,” *IEEE Trans. Microwave Theory Tech.*, vol. 54, pp. 160-168, 2006.

Printed Prototype of a Wideband S-Shape Microstrip Patch Antenna for Ku/K Band Applications

M. Habib Ullah[1,2], M. T. Islam[2], and J. S. Mandeep[1,2]

[1]Department of Electrical, Electronic, and System Engineering
Faculty of Engineering and Built Environment,
University Kebangsaan Malaysia, Bangi, Selnagor, Malaysia 43600
habib_ctg@yahoo.com, mandeep@eng.ukm.my

[2]Institute of Space Science (ANGKASA),
University Kebangsaan Malaysia Bangi, Selnagor, Malaysia 43600.
titareq@yahoo.com

Abstract ─ Design and analysis of a printed prototype of an S-shape slotted patch antenna for 16.8 GHz Ku band application is proposed in this paper. The proposed miniaturized S-shape patch antenna has been designed and analyzed by using market available Ansoft high frequency electromagnetic simulator and fabricated on a printed circuit board. The measured -10 db return loss bandwidth ranges from 15.35 GHz to 19.65 GHz (25.59 %) with achieved gain of 6.2 dBi at the resonant frequency 16.8 GHz. A radiation efficiency of 88.2 % and 80° (320°-40°) 3 dB beam width has been testified. The symmetric and almost steady radiation pattern of the proposed antenna has been made suitable for the frequency range from 15.35 GHz to 19.65 GHz. Furthermore, the current distribution over the radiating patch is examined and a parametric study of the ground plane size has been conducted in this study.

Index Terms ─ Anechoic measurement chamber, finite element method, printed circuit board, microstrip patch antenna, and wideband.

I. INTRODUCTION

With the rapid growth of wireless technology antenna miniaturization has become a vital concern for the development of compact communication terminal [1-3]. Nowadays, all electronic communication devices are compulsory to be compact, smaller size, lightweight, and low cost with multiband operation capability [4-7]. Antennas are needed to be small enough to be integrated with compact communication module. Due to low profile, low cost, easy integration, and manufacturability; the demand of planar microstrip patch antenna has been increased to be integrated with more than one communication system into a compact module [8-12]. In order to design such small multifunctional wireless devices, antenna modules are required to be miniaturized accordingly [13-15]. To design miniaturized patch antennas for multiband operation, radiation efficiency, wide bandwidth, low manufacturing cost, steady radiation patterns, and consistent gain are required to be taken in to account. A number of studies on multiband antenna design have been reported, including DNG ZOR based antenna for multiband operation [16], switch fed reconfigurable antenna structure [17], flat-plate inverted-F antenna [18], step-shaped microstrip line fed printed monopole slot antenna [19], and folded 3D monopole multiband antenna [20].

A considerable amount of research effort has been given to design small antennas for Ku/K band applications. Due to scarcity of the bandwidth in lower bands and availability in higher band, Ku/K band has become very popular for radar applications. Recently, numerous small

Submitted On: May 30, 2012
Accepted On: Feb. 6, 2013

patch antennas are investigated for Ku/K band applications. A comprehensive analysis of MIMO SAR, virtual antenna has been done [21], wideband EBG antenna using double-layer frequency selective surfaces [22], an active phased array antenna for Ku-Band for mobile satellite [23], linearly polarized omnidirectional planar filtenna Ku-band [24], dual-polarized low-profile hemispherical luneburg lens antennas [25] etc.

An 8×10 mm^2 S-shape planar microstrip line fed slotted patch antenna has designed and configured for Ku/K band SAR remote sensing applications. The designed antenna has been fabricated on a printed circuit board (PCB). The low cost, long lasting, market available 1.5 mm thick FR4 material used as antenna substrate with dielectric constant (ε_r) of 4.6. The proposed antenna has been measured in far field environment and measured -10 dB return loss bandwidth 4.3 GHz from 15.35 GHz to 19.65 GHz with peak gain 8.77 dBi and 90.8 % of radiation efficiency. The symmetric and nearly steady and omnidirectional radiation pattern has also been measured. Furthermore, the effects of the length of ground plane have analyzed.

II. PROPOSED ANTENNA DESIGN AND CONFIGURATION

The proposed S-shape antenna has been designed and analyzed by using finite element method (FEM) based market available high frequency electromagnetic simulator [26-27]. Figure 1 shows the schematic diagram of the proposed antenna design geometry. S-shape is obtained by cutting slots from the rectangle plate. The design of the microstrip radiating patch element of the proposed antenna comprises of the configuration of its dimensions. The basic idea of the patch dimension was taken from the established mathematical formulation [27]. Although, the available mathematical modeling is based on the conventional rectangular patch for the slotted S-shape radiating patch the dimension is determined using test and modify method,

$$W = \frac{c}{2f_0}\sqrt{\frac{\varepsilon_r + 1}{2}} \tag{1}$$

$$L = \frac{c}{2f_0\sqrt{\varepsilon_r}} - 2\Delta l\,. \tag{2}$$

In the above equations (1) and (2), W is the width and L is the length of the patch, f_0 is the center resonant frequency, c is the speed of light in vacuum. The effective dielectric constant can be calculated by using the following equation [27],

$$\varepsilon_e = \frac{1}{2}(\varepsilon_r + 1) + \frac{1}{2}(\varepsilon_r - 1)\sqrt{\left(1 + \frac{10h}{W}\right)} \tag{3}$$

where ε_r is the relative dielectric constant and h is the thickness of the substrate. Due to the fringing field around the periphery of the patch, the antenna electrically looks larger than its physical dimensions. The increment to the length, Δl due to the fringing field and can be expressed as [28],

$$\Delta l = 0.412h\frac{(\varepsilon_e + 0.3)\left[\frac{w}{h} + 0.8\right]}{(\varepsilon_e - 0.258)\left[\frac{w}{h} + 0.8\right]}\,. \tag{4}$$

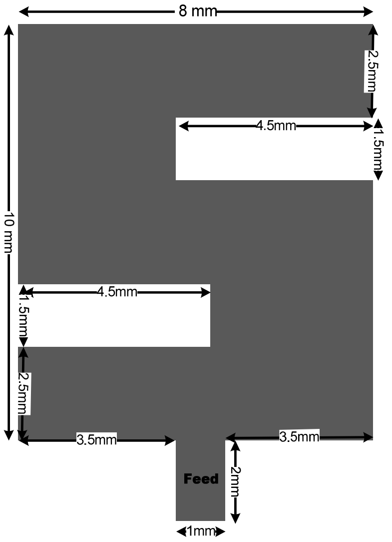

Fig. 1. Schematic diagram of the proposed antenna.

The patch width (W) has a minor effect on the resonance and it has been determined by using the mathematical modeling [29]. The length of the radiating patch (L), location of the feeding point and the slots has a dominant effect on the resonance. The length of the patch (L) is 0.44 λ and the width (W) is 0.56 λ, where λ is the corresponding wavelength at the resonance 16.8 GHz. By carefully tuning the dimension and location of the two 2.5×1.5 mm^2 slots the desired frequency band has been determined. The photograph of the proposed antenna prototype is shown in Fig. 2. A 2 mm long 1 mm wide microstrip line has been used for the feeding to meet the 50 ohm impedance characteristics. An SMA connector has been used at the end of the microstrip feed line for excitation.

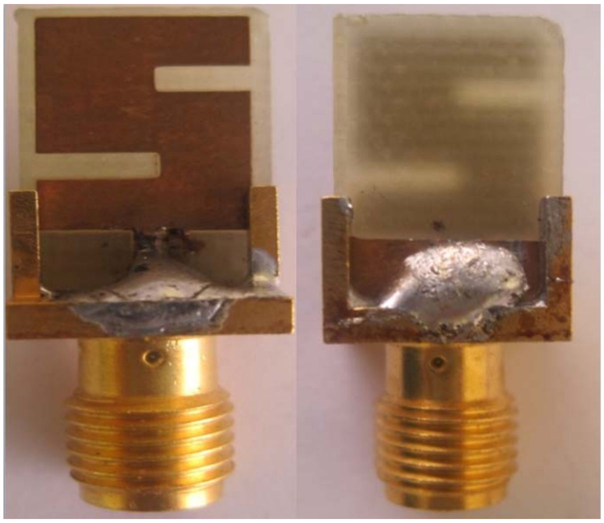
(a) (b)

Fig. 2. Printed prototype (a) patch and (b) ground plane of the proposed antenna.

The proposed antenna is modeled as resistors with a standard 50 Ω, when designing the interface circuits at the operating frequencies. Figure 3 has illustrated the equivalent RLC circuit model of the proposed antenna. For equivalent circuit configurations such as the C- and Π- network topologies, for which the circuit branch functions are uniquely given in terms of the associated network parameters, each branch can be separately augmented by parallel and series branch elements. The Z-parameter responses of this antenna are obtained using IE3D EM simulator based on method of moments (MoM) and from the equivalent circuit modeling using only a single augmentation. A satisfactory agreement is also observed between SPICE and MoM simulations at the resonant frequencies. The RLC parameter is frequency dependent, the resonant frequencies have been determined by a conducting element L. The circuit parameters are R1 = 704.031 Ohm, R2 = 122.382 Ohm, R3 = 36.411 Ohm, C1 = 0.0516 PF, C2 = 0.0809 PF, C3 = 0.477 PF, and L = 0.0335 nH. The circuit shows high pass filter characteristics without inductor L. The resonant frequency has been determined by a conducting element L.

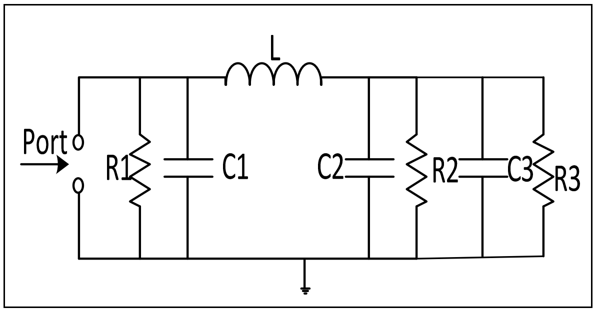

Fig. 3. Equivalent RLC circuit of the proposed antenna.

III. RESULTS AND ANALYSIS

The results of the proposed antenna prototype have been measured in a rectangular shape 5.5 m × 5 m × 3.5 m anechoic measurement chamber. A double ridge guide horn antenna is used as a reference antenna. The photograph of the anechoic measurement chamber is shown in Fig. 4. Pyramidal shape electrically-thick foam absorber with less than -60 dB reflectivity at normal incidence is used on the wall, ceiling, and floor. A turn table of 1.2 m diameter is used to rotate the measuring antenna with specification, 1 rpm rotation speed; 360° rotation angle connected with a 10 meter cable between controllers. An Agilent vector network analyzer (VNA) range up to 20 GHz is used for measurement procedures.

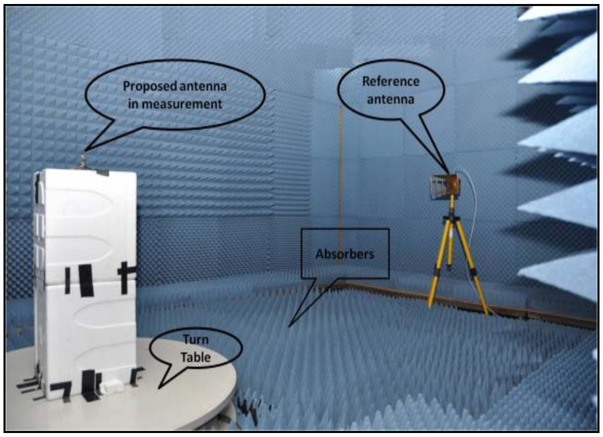

Fig. 4. Illustration of the anechoic measurement chamber.

The return loss of the proposed antenna with three different lengths of the ground plane is shown in Fig. 5. It can be clearly seen that, the return loss value is much lower and a wider bandwidth is achieved from the proposed antenna with 4.5 × 2 mm^2 ground plane. The simulated and measured return loss of the proposed antenna is shown in Fig. 6. It can be observed from the graph that, 4.3 GHz (15.35 GHz – 19.65 GHz) -10 dB bandwidth has been measured from the proposed antenna prototype. The measured bandwidth covers 2.65 GHz of Ku band and 1.65 GHz of K band. Figure 7 shows the achieved radiation efficiency and gain of the proposed antenna. The average gain of the proposed antenna is 5.39 dBi and the average radiation efficiency is 88.25 %, which have been obtained over the entire operating frequency from 15.35 GHz to 19.65 GHz. A 6.20 dBi gain with 88.21 % radiation efficiency has been achieved at the of 16.8 GHz.

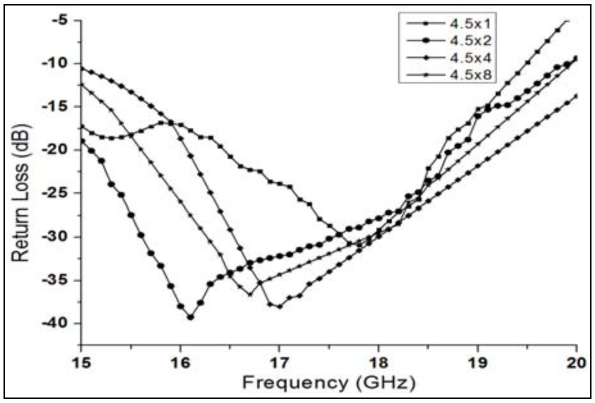

Fig. 5. Return loss of the antenna with four different ground plane sizes.

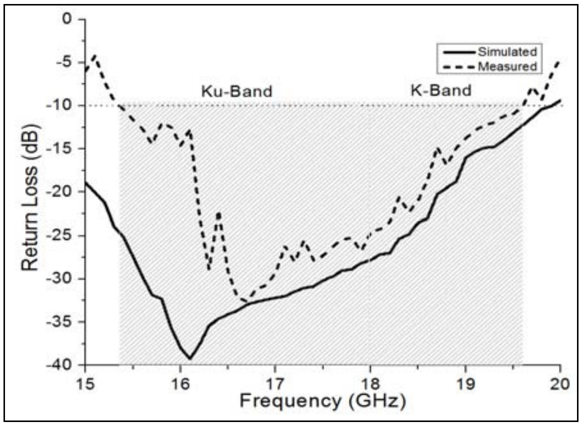

Fig. 6. Simulated and measured return loss of the proposed antenna.

The simulated and measured radiation pattern of the proposed antenna prototype are shown in Fig. 8. The measured 3 dB beam width 80° (320°-40°) can be clearly seen from the E-plane radiation pattern. It can also be observed from the radiation pattern, that the proposed antenna can operate as omnidirectional. In both radiation pattern of E- and H-planes, the cross-polar effect is much lower than the co-polar effect, which is desired. The measured co-polar value is not less than -10 dB from 290° to 90°, from 160° to 210° in E-plane and in H-plane from 260° to 80° and from 190° to 240°. The symmetric and almost steady radiation pattern makes the proposed antenna suitable for smooth operation in part of the K/Ku band application.

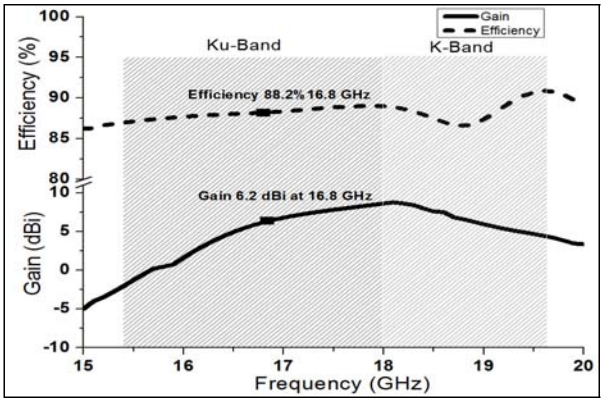

Fig. 7. Gain and efficiency of the proposed antenna.

Table 1: Comparison between the proposed antenna and some existing antennas.

Author	Proposed	[30]	[31]	[32]
Frequency (GHz)	16.8	2.08	2.0	1.309
Size (mm^2)	20x14	79x38	58x58	40x40
Bandwidth (GHz)	4.3	0.440	1.03	0.009
Gain (dBi)	6.2	9.5	9.3	1.9

The current distribution along the radiating patch is shown in Fig. 9. The current flows stronger near the feeding point and around the cutting edge and weaker in the upper side farthest from the feed line. Comparison between the proposed antenna and some existing antennas is shown in Table 1. It can be clearly seen that, the proposed antenna is smaller in size with wider bandwidth and high gain. Conversely, some of reported antennas achieved higher gain compromising the overall size. These antennas would need bigger space to be integrated with small devices, which is not preferred.

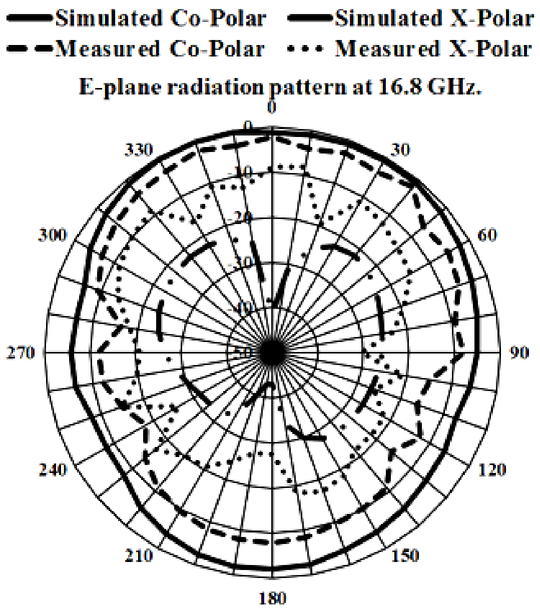

E-plane radiation pattern at 16.8 GHz.

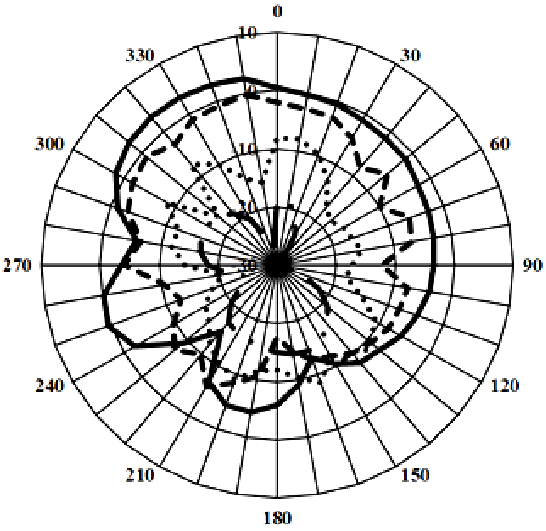

H-plane radiation pattern at 16.8 GHz

Fig. 8. E- and H-planes radiation pattern of the proposed antenna.

IV. CONCLUSION

A 0.44 λ × 0.56 λ microstrip line fed S-shape electrically small patch antenna has been designed, analyzed, and measured in this paper. The proposed slotted patch antenna has been fabricated on a 1.6 mm thick commonly available FR4 substrate. A parametric study of the proposed antenna has been conducted with four different lengths of ground plane and an optimized dimension is chosen. The measured -10 dB return loss bandwidth 4.3 GHz operating frequency from 15.35 GHz to 19.65 GHz with maximum gain 8.77 dBi of the proposed antenna prototype. The measured bandwidth covers 2.65 GHz of Ku band and 1.65 GHz of K band. The radiation efficiency of 88.21 % and gain 6.20 dBi has been achieved at the resonant frequency 16.8 GHz. The proposed antenna shows the omnidirectional pattern of a steady radiation characteristics.

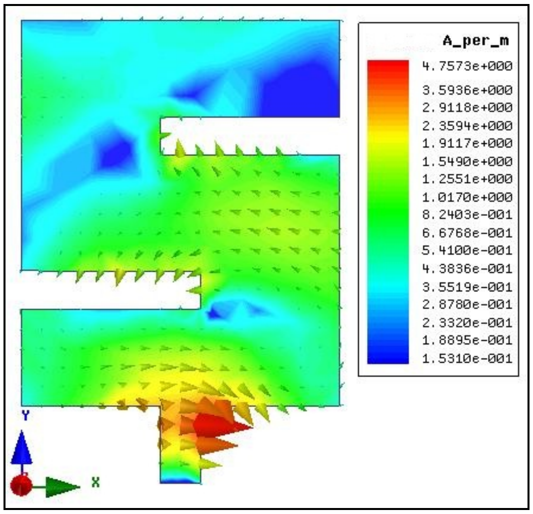

Fig. 9. Current distribution along the radiating patch of the proposed antenna.

REFERENCES

[1] M. Mighani, M. Akbari, and N. Felegari, "A novel SWB small rhombic microstrip antenna with parasitic rectangle into slot of the feed line," *Appl. Comp. Electro. Society (ACES) Journal*, vol. 27, no. 1, pp. 74-79, Jan. 2012.

[2] M. Mighani, M. Akbari, and N. Felegari, "A CPW dual band notched UWB antenna," *Appl. Comp. Electro. Society (ACES) Journal*, vol. 27, no. 4, pp. 352-359, April 2012.

[3] R. Azim, M. T. Islam, and N. Misran, "Design of a planar UWB antenna with new band enhancement technique," *Appl. Comp. Electro. Society (ACES) Journal*, vol. 26, no. 10, pp. 856-862, Oct. 2011.

[4] A. T. Mobashsher, M. T. Islam, and N. Misran, "Wideband compact antenna with partially radiating coplanar ground plane," *Appl. Comp. Electro. Society (ACES) Journal*, vol. 26, no. 1, pp. 73-81, Jan. 2011.

[5] D. Yang, Y. C. Jiao, P. Fei, B. Li, and Q. T. Zhang, "Design of a multiband quasi-yagi-type antenna with CPW-to-CPS transition," *IEEE Antennas Wirel. Propag. Lett.*, vol. 10, pp. 1120-1123, 2011.

[6] J. William and R. Nakkeeran, "A new UWB slot antenna with rejection of WiMax and WLAN bands," *Appl. Comp. Electro. Society (ACES) Journal*, vol. 25, no. 9, pp. 787-793, Sep. 2010.

[7] R. Azim, M. T. Islam, and N. Misran, "Compact tapered shape slot antenna for UWB applications," *IEEE Antennas Wirel. Propag. Lett.*, vol. 10, pp. 1190-1193, 2011.

[8] D. S. Javan and O. H. Ghouchani, "Cross slot antenna with U-shaped tuning stub for ultra wideband applications," *Appl. Comp. Electro. Society (ACES) Journal*, vol. 24, no. 4, pp. 427-432, August 2009.

[9] M. N. –Jahromi and N. K. -Barchloui, "Analysis of the behavior of Sierpinski carpet monopole antenna," *Appl. Comp. Electro. Society (ACES) Journal*, vol. 24, no. 1, pp. 32-36, Feb. 2009.

[10] C. Y. D. Sim, F. R. Cai, and Y. P. Hsieh, "Multiband slot-ring antenna with single- and dual-capacitive coupled patch for wireless local area network/worldwide interoperability for microwave access operation," *IET Microwaves, Antennas & Propag.*, vol. 5, no. 15, pp. 1830-1835, 2011.

[11] M. N. Shakib, M. T. Islam, and N. Misran, "High gain W-shaped microstrip patch antenna," *IEICE Electron. Express*, vol. 7, no. 20, pp. 1546-1551, 2010.

[12] A. A. L. Neyestanak, F. H. Kashani, and K. Barkeshli, "W-shaped enhanced-bandwidth patch antenna for wireless communication," *Wireless Personal Communications*, vol. 43, no.4, pp. 1257-1265, 2007.

[13] D. K. Ntaikos, N. K. Bourgis, and T. V. Yioultsis, "Metamaterial-based electrically small multiband planar monopole antennas," *IEEE Antennas Wirel. Propag. Lett.*, vol. 10, pp. 963-966, 2011.

[14] W. -C. Liu, W. -R. Chen, and C. -M. Wu, "Printed double S-shaped monopole antenna for wideband and multiband operation of wireless communications," *IEE Proceedings Microwaves, Antennas and Propag.*, vol. 151, no. 6, pp. 473-476, 2004.

[15] R. Azim, M. T. Islam, and N. Misran, "Dual polarized microstrip patch antenna for Ku-band application," *Informacije MIDEM*, vol. 41, no. 2, pp. 114-117, June 2011.

[16] J. K. Ji, G. H. Kim, and W. M. Seong, "A compact multiband antenna based on DNG ZOR for wireless mobile system," *IEEE Antennas Wirel. Propag. Lett.*, vol. 8, pp. 920-923, 2009.

[17] A. C. K. Mak, C. R. Rowell, R. D Murch, and M. Chi-Lun, "Reconfigurable multiband antenna designs for wireless communication devices," *IEEE Trans. Antennas Propag.*, vol. 55, no.7, pp. 1919-1928, 2007.

[18] L. Pazin, N. Telzhensky, and Y. Leviatan, "Multiband flat-plate inverted-F antenna for Wi-Fi/WiMAX operation," *IEEE Antennas Wirel. Propag. Lett.,* vol. 7, pp. 197-200, 2008.

[19] K. –L. Wong and L. –C. Lee, "Multiband printed monopole slot antenna for WWAN operation in the laptop computer," *IEEE Trans. Antennas Propag.*, vol. 57, no. 2, pp. 324-330, 2009.

[20] H. Kanj and S. M. Ali, "Compact multiband folded 3-D monopole antenna," *IEEE Antennas Wirel. Propag. Lett.*, vol. 8, pp. 185-188, 2009.

[21] W. –Q. Wang, "Virtual antenna array analysis for MIMO synthetic aperture radars," *International Journal of Antennas and Propag.*, ID 587276, vol. 2012, pp. 1-10, 2012.

[22] L. Moustafa and B. Jecko, "Design of a wideband highly directive EBG antenna using double-layer frequency selective surfaces and multifeed technique for application in the Ku-band," *IEEE Antennas Wirel. Propag. Lett.*, vol. 9, pp. 342-346, 2010.

[23] S. Vaccaro, D. Llorens, J. Padilla, and R. Baggen, "Low cost Ku-band electronic steerable array antenna for mobile satellite communications," *in Proc.5th European Conference on Antennas and Propagation (EUCAP)*, Rome, Italy, pp. 2362-2366, 11-15 April 2011.

[24] C. Yu, W. Hong, Z. Kuai, and H. Wang, "Ku-band linearly polarized omnidirectional planar filtenna," *IEEE Antennas Wirel. Propag. Lett.*, vol. 11, pp. 310-313, 2012.

[25] A. R. Weily and N. Nikolic, "Dual-polarized planar feed for low-profile hemispherical luneburg lens antennas," *IEEE Trans. Antennas Propag.*, vol. 60, no. 1, pp. 402-407, 2012.

[26] M. Habib Ullah, M. T. Islam, J. S. Mandeep, and N. Misran, "A new bouble L shape multiband patch antenna on polymer resin material substrate," *Appl. Phys. A-Mater. Sci. Process.*, vol. 110, no. 1, pp. 199-205, 2012.

[27] M. H. Ullah, M. T. Islam, M. S. Jit, and N. Misran, "A three-stacked patch antenna using high-dielectric ceramic material substrate," *J. Intell. Mater. Syst. Struct.*, vol. 23, no. 16, pp. 1827-1832, 2012.

[28] M. Habib Ullah, M. T. Islam, J. S. Mandeep, and N. Misran, "A compact wideband antenna on dielectric material substrate for K band," *Electronics and Electrical Engineering*, vol. 123, no. 7, pp. 75-78, 2012.

[29] Q. Rao and W. Geyi, “Compact multiband antenna for handheld devices,” *IEEE Trans. Antennas Propag.*, vol. 57, no.10, pp. 3337-3339, 2009.
[30] M. T. Islam, M. N. Sakib, and N. Misran, “Design analysis of high gain wideband L-probe FED microstrip patch antenna,” *Progress In Electromagnetics Research (PIER)*, vol. 95, pp. 397-407, 2009.
[31] B. Li, Y. Z. Yin, W. Hu, Y. Ding, and Y. Zhao, “Wideband dual-polarized patch antenna with low cross polarization and high isolation,” *IEEE Antennas Wirel. Propag. Lett.*, vol. 11, pp. 427-430, 2012.
[32] S. L. C. Xiao, Y. X. Guo, Y. -Y. Bai, M. -C. Tang, and B. -Z. Wang, “Compact circularly-polarised microstrip antenna with symmetric-slit,” *Electron. Lett.*, vol. 48, no. 4, pp. 195-196, 2012.

Mohammad Habib Ullah was born in Chittagong, Bangladesh in 1980. He has awarded his B.Sc Honors in Computer and Communication Engineering from International Islamic University Chittagong (IIUC), Bangladesh and M.Sc. degree in Communication Engineering from International Islamic University Malaysia (IIUM) in 2003 and 2011, respectively. He has worked several national and international companies in Bangladesh, Kingdom of Saudi Arabia and Malaysia as engineer and academician. He worked as research assistant in several research project funded by government and non-government organization. Currently, he is pursuing his Ph.D. degree at Universiti Kebangsaan Malaysia and worked as research assistant at Institute of Space Science (ANGKASA) in a research project funded by Malaysian government. He has authored and co-authored 26 International refereed journal articles and 5 conference papers. His research interest focuses on telecommunication, wireless communication, MIMO, CDMA, antenna & propagation, networking etc. He is editor and reviewer of several reputed indexed peer reviewed journals.

Mohammad Tariqul Islam was born in Dhaka, Bangladesh in 1975. He received his B.Sc. and M. Sc. Degrees in Applied Physics and Electronics from the University of Dhaka, Dhaka, Bangladesh in 1998 and 2000, respectively and a Ph.D. degree in Telecommunication Engineering from the Universiti Kebangsaan Malaysia (UKM) in 2006. In August 2000, he became an Adjunct Research Fellow at Bose Research Center, University of Dhaka, Dhaka. From September 2000 until June 2002, he worked as a lecturer at International Islamic University Chittagong (IIUC), Dhaka. In August 2006, he became an Assistant Professor at IIUC. He has been very promising as a researcher, with the achievement of several International Gold Medal awards, a Best Invention in Telecommunication award and a Special Award from Vietnam for his research and innovation. He has filled 6 patent applications. He has authored or co authored 102 international journal papers and 90 international and local conference papers and 3 books. Thus far, his publications have been cited 560 times, and the H-index is 15 (Source: Scopus). He has been awarded “Best Researcher Award” in 2010 and 2011 at UKM. He served as a faculty member at the Multimedia University (MMU), Malaysia from May 2007 until May 2008. He is currently a Professor at the Institute of Space Science (ANGKASA), UKM, Malaysia. He is also an associate fellow of the Institute of Visual Informatics. His research interests concern enabling technology for RF, antenna technology, electromagnetic absorption and radio astronomy instruments. He is now handling many research projects from the Ministry of Science, Technology and Innovation (MOSTI), Ministry of Higher Education Malaysia (MOHE) and some International grants from Japan.

Mandeep Jit Singh received his B.Eng. (with honors) and Ph.D. degrees in Electrical and Electronic Engineering from the University of Notrhumbria, UK, and Universiti Sains Malaysia, in 1998 and 2006, respectively. From 2006 up to June 2009, he was attached at Universiti Sains Malaysia as a Lecturer. Currently, he is attached to the Universiti Kebangsaan Malaysia as a Senior Lecturer. His areas of specialization are radiowave propagation in satellite communication system, radar, antenna design, RF, and microwave. His current research collaboration is with the Association of Radio Industries and Business (ARIB) Japan to analyze the rain fade at Ku-band in tropical climate using satellite involving countries such as Thailand, Philippines, Indonesia, and Fiji. Singh has published 30 papers in journals, most in his special field radiowave propagation. He has reviewed more than 40 articles from IEEE Journals to PIERS Journals.

Broadband CPW-Fed Circularly Polarized Square Slot Antenna with Arc-Shaped and Inverted-L Grounded Strips

A. Mousazadeh [1], M. Naser-Moghaddasi [1], F. Geran [1], S. Mohammadi [2], and P. Zibadoost [2]

[1]Department of Engineering, Science and Research branch,
Islamic Azad University, Tehran, 14778-93855, Iran
asgar.musazadeh@yahoo.com, mn.moghaddasi@srbiau.ac.ir, geran_e@yahoo.com

[2]Department of Electrical Engineering, Urmia University, Urmia, 57561-51818, Iran
aslelectco@gmail.com, payam.zibadoost@yahoo.com

Abstract **─** This paper presents a new wideband circularly polarized square slot antenna (CPSSA) with a coplanar waveguide (CPW) feed. The proposed antenna is composed of two arc-shaped and inverted-L grounded strips around opposite and mirror corners of the square slot. In this antenna the impedance bandwidth and the axial ratio bandwidth (ARBW) are increased compared to the previous CPSSA structures. For the optimized antenna prototype, the measured 3 dB axial ratio bandwidth is 76 % (3 GHz - 6.7 GHz) and the measured VSWR < 2 impedance bandwidth is as large as 108 % (3 GHz - 10.1 GHz). Throughout this paper, the improvement process of the axial ratio (AR) and S_{11} properties are presented and discussed in detail.

Index Terms **─** Axial ratio (AR), broadband, circularly polarized (CP), and square slot antenna.

I. INTRODUCTION

In the past few years, circularly polarized (CP) antennas have become more popular due to their importance in wireless communications, radar, radio frequency identifier (RFID), and sensor systems. For deploying a transmitter and a receiver without causing a polarization mismatch between them, circular polarization (CP) is becoming popular in wireless communications to enhance system performance, providing better mobility, and weather penetration, more than the linearly polarized (LP) antennas [1, 2] and also reduction in multi-path reflections. In addition, the channel capacity of a communication link can be doubled in a frequency reuse system by using circular polarization [3]. To create circular polarization, the antenna must radiate from two orthogonal modes with equal amplitude that are in phase quadrature. For generating CP radiation, various structures and designs of broadband CP antennas have been produced. A microstrip slot antenna may be a good choice as it is low profile, low cost, lightweight, and can be easily integrated with monolithic microwave integrated circuits (MMICs) [4].To improve the operating bandwidth and not increase the antenna size, using the printed slot antenna is a possible method. Since the printed slot antenna is a dual of the microstrip antenna, it is also possible that by introducing some perturbations to the slot antenna, CP radiation of slot antenna can be achieved [5]. Some of the techniques that are used to design these kinds of antennas with broad CP bandwidth include the following: embedding two inverted-L grounded strips around two opposite corners of the slot [1], embedding T-shaped grounded metallic strip, which is perpendicular to the axial direction of the CPW feed-line [2], using an asymmetric CPW fed from a corner of the slot with an additional pair of grounded strips implanted in the slot [6], corrugated slot antenna with meander line loaded [7], utilizing the embedded arc-shaped grounded metallic strip for circular and linear polarization [8], and embedding a lightning-shaped feed line and inverted-L grounded strips [9].

Submitted On: Oct. 22, 2012
Accepted On: Feb. 6, 2013

This paper presents a novel design of a CPW-fed circularly polarized square slot antenna. According to measured results, the impedance bandwidth is about 108 %, entirely covering the 3 dB AR bandwidth, which is about 76 %. This antenna is suitable for IEEE 802.11a, (5150–5350 MHz / 5725–5825 MHz) and for IEEE 802.16, (3200–3800 MHz / 5200–5800 MHz).

II. ANTENNA DESIGN

Figure 1 shows the configuration of the proposed CPW-fed circularly polarized square slot antenna (CPSSA).

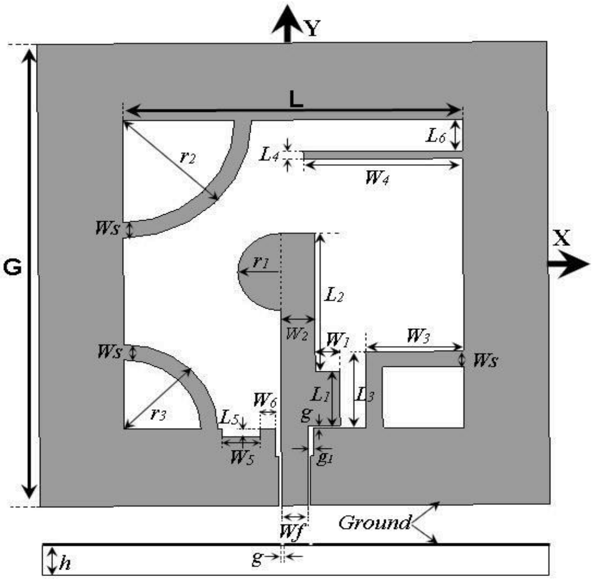

Fig. 1. Geometry of the proposed CP square slot antenna with G = 60, L = 40, h = 0.8, $W_f = 3.1$, g = 0.3, $g_1 = 0.7$, $r_1 = 5$, $r_2 = 15.2$, $r_3 = 11$, Ws = 2, $L_1 = 7$, $W_1 = 2.9$, $L_2 = 18$, $W_2 = 4.05$, $L_3 = 9.9$, $W_3 = 11.6$, $L_4 = 1$, $W_4 = 18.75$, $L_5 = 1.1$, $W_5 = 4.5$, $L_6 = 4.1$, and $W_6 = 1.75$ (All units are in millimeters).

The proposed CPSSA is printed on a commercially cheap FR4-epoxy substrate with $\varepsilon_r = 4.4$, tan (δ) = 0.024, and dimensions of 60 × 60 × 0.8 mm^3. The feed line of the proposed antenna is CPW and is connected to a 50 Ω SMA connector. The gap between the feed line and the ground is 0.3 mm, which is widened at the end to improve the impedance bandwidth. The length and width of the feed line are, respectively, 35.3 mm and 3.1 mm, which is connected to a semi-circular patch. A tuning vertical stub has been embedded in the feeding structure. The CP operation of the proposed antenna is greatly related to the two arc-shaped and an inverted-L grounded strips in opposite and mirror corners placed around the corners of the square slot. The structure of the inverted-L grounded metal strips was first proposed in [1]. For increasing ARBW a tuning horizontal grounded strip at the top right corner and a tuning slit at the left side of the feed line on the ground plane have been employed. The structure shown in Fig. 1 will generate right-hand and left-hand circularly polarized (RHCP and LHCP) radiations in the +z and -z directions, respectively.

III. RESULTS AND DISCUSSION

The performance of the CPSSA at parametric studies has been investigated to find the optimized parameters using the Ansoft high frequency structure simulator software (HFSS, ver.12) based on the finite element method (FEM). An Agilent 8722ES vector network analyzer has been used to measure the return loss (S_{11}). In the simulation setup perfect electric conductor (PEC) and an ideal excitation port are assumed. For simplification in the antenna design G = 60 mm, L = 40 mm, h = 0.8 mm were preselected. For describing the design process, five prototypes of the proposed antenna are defined as follows (Fig. 2): Ant. I includes only a feed line connected to semi-circular patch and ground plane; Ant. II contains two arc-shaped grounded strips around left side corners and inverted-L grounded strip at the bottom right side corner. In Ant. III a vertical tuning stub ($L_1 \times W_1$) is embedded in the feed structure and the gap between the signal strip and the ground plane is widened at the end. Ant. IV has a horizontal grounded strip ($L_4 \times W_4$) at top right corner and Ant. V has a tuning slit ($L_5 \times W_5$) that has been cut and removed from the ground plane at the left side of the feed line.

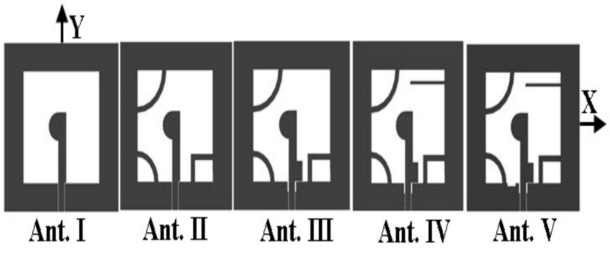

Fig. 2. Five improved prototypes of the proposed CPSS antenna.

Figure 3 (a) and (b) present the simulated frequency responses of 10 dB return loss and 3 dB axial ratio variations for the five designed prototypes of the proposed antenna. From Fig. 3 (b), it can be observed that Ant. I has a linear polarization. By embedding two arc-shaped and an inverted-L grounded strip around the corners of the square slot, the AR is greatly improved, which reaches 3 % (5.27 GHz–5.44 GHz) and 4 % (5.92 GHz–6.17 GHz) (Ant. II). Nevertheless, in this case the AR is not guaranteed by -10 dB return loss.

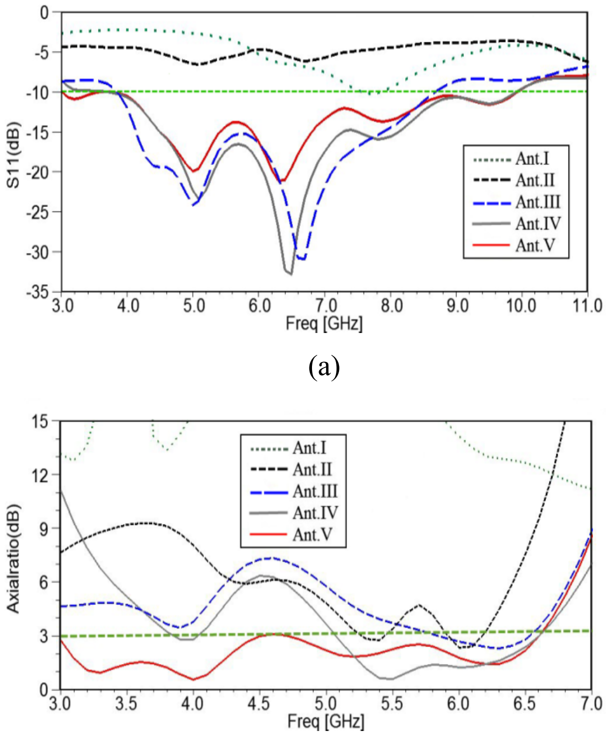

(a)

(b)

Fig. 3. Simulated (a) S_{11} and (b) AR for antennas I-V (for CPSS antennas with optimized values of the design parameters shown in Fig. 1).

To improve the impedance matching, a vertical tuning stub is added to the feed structure and the gap of CPW feed is formed to a step shape. As shown in Fig. 3 (b), these structures (the embedding of vertical tuning stub to the feed line and widening the gap between the feed line and the ground plane) have great effect on the impedance bandwidth of Ant. II (called Ant. III). The 3 dB ARBW achieved for Ant. III is about 11 % (5.84 GHz – 6.53 GHz). By adding a horizontal strip at the top right corner of the ground plane the AR bandwidth will reach 26 % (5.07 GHz – 6.6 GHz), (Ant. IV). At last, by embedding the rectangular slit at the left side of the feed, not only AR bandwidth is increased to 75 % (3 GHz – 6.6 GHz) but also the impedance bandwidth can be increased to cover the whole CP bandwidth. The simulated results in Fig. 3 (a) indicate that including the horizontal strip and the rectangular slit, greatly influence the ARBW.

Figure 4 (a) and (b) indicate the measured and simulated return loss and AR characteristics for the proposed antenna. Close correspondence between the simulated and measured results is observed and the little difference between them is attributed to factors such as SMA connector effects, fabrication imperfections, and inappropriate quality of the microwave substrate. As also indicated in Fig. 4, the measured impedance bandwidth of the proposed antenna is from 3 GHz up to 10.1 GHz (3.33:1, 108 %) for VSWR < 2 and the measured 3 dB ARBW is extended from 3 GHz to 6.7 GHz (2.2:1, 76 %) that is about 3700 MHz. Considering the AR and the impedance bandwidth, it is clear that this proposed antenna is suitable for IEEE 802.11a, (5150–5350 MHz / 5725–5825 MHz) and for IEEE 802.16, (3200–3800 MHz / 5200–5800 MHz).

In Table 1 the impedance bandwidth and AR bandwidth of the proposed antenna (designed based on the ideas, which are presented in [1, 2, 6-11]) has been compared with prototypes in [1, 9, 10]. It is observed that the proposed antenna has wider AR bandwidth than the other ones. All these antennas were fabricated on an FR4 substrate with a loss tangent of tan (δ) = 0.024, permittivity of ε_r = 4.4. A photograph of the realized CPSSA antenna is shown in Fig. 5.

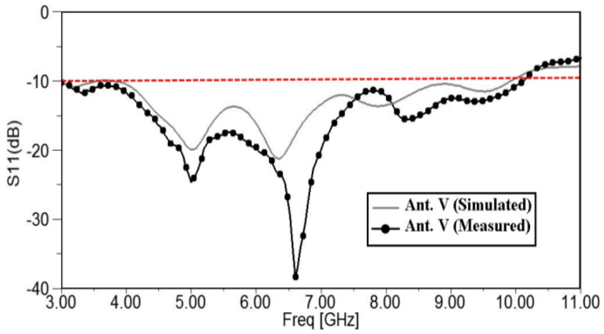

(a)

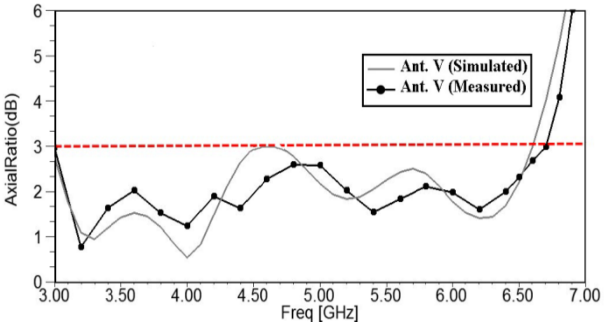

(b)

Fig. 4. Measured and simulated diagrams of (a) the return loss and (b) the axial ratio of the proposed antenna.

Table 1: Summary of the measured characteristics of some CPSS antennas, where f_c refers to the center frequency of the 3 dB AR bandwidth.

Ref.	Impedance Band (MHz)	f_c (MHz)	3 dB ARBW (MHz, %)
Ref. [1]	1600-3055	2665	2300-3030, 27.4%
Ref. [9]	2023-3421	2754	2075-3415, 48.8%
Ref. [10]	2674-13124	5969	4995-6945, 32.2%
Proposed antenna	3000-10100	4850	3000-6712, 76%

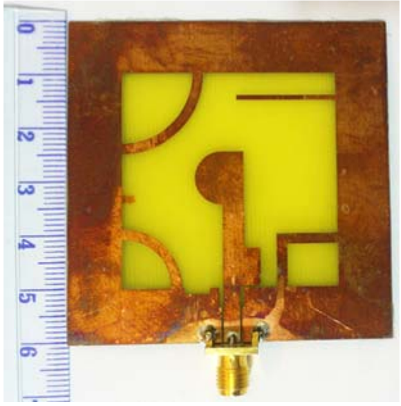

Fig. 5. Photograph of the realized CPSS antenna with standard SMA connector.

Figure 6 shows the surface current distributions of the proposed antenna at 4 GHz at the minimum point of the simulated AR for four different time instants, i.e., ωt = 0˚, 90˚, 180˚, and 270˚. It is observed that the current distribution in 180˚ and 270˚ are equal in magnitude and opposite in phase to that of 0˚ and 90˚. The proposed CP slot antenna is able to generate RHCP in the +z direction, whereas LHCP is produced in the –z direction.

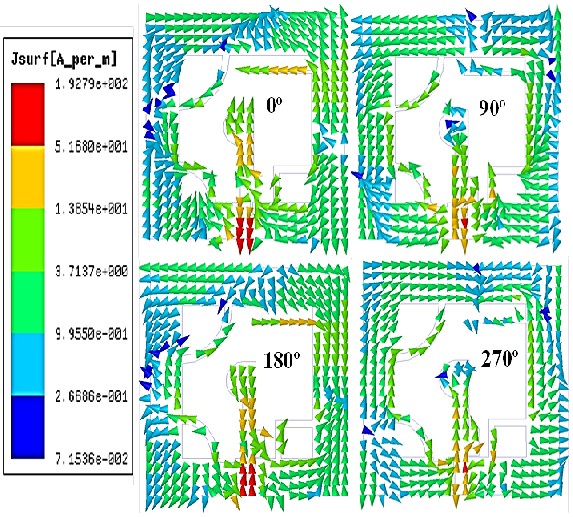

Fig. 6. Distribution of the surface current on the feed and ground of the proposed antenna at 4 GHz in 0˚, 90˚, 180˚, and 270˚ phases.

The simulated and measured gain in +z direction is plotted in Fig. 7. For measuring the gain of the fabricated antenna, one LP antenna is used in two orientations, the partial gains, G_{TV} and G_{TH} are combined to yield the total gain as in [11],

$$G_T = 10 \log (G_{TV} + G_{TH}) . \qquad (1)$$

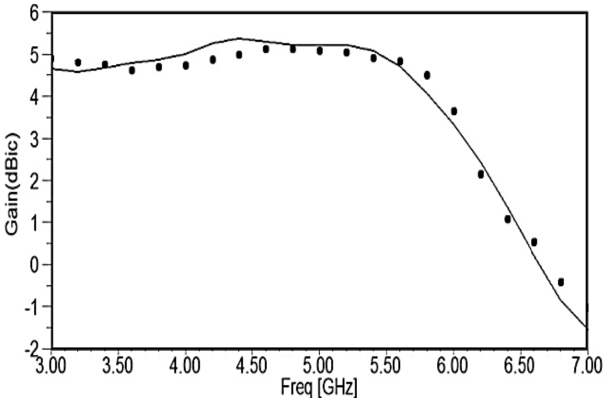

Fig. 7. Measured and simulated antenna gains in the +Z-direction.

Figure 8 shows the normalized radiation patterns of the proposed antenna simulated and measured at two sample frequencies of 4.2 GHz and 6.5 GHz. The results include RHCP and LHCP in the XZ and YZ planes.

.

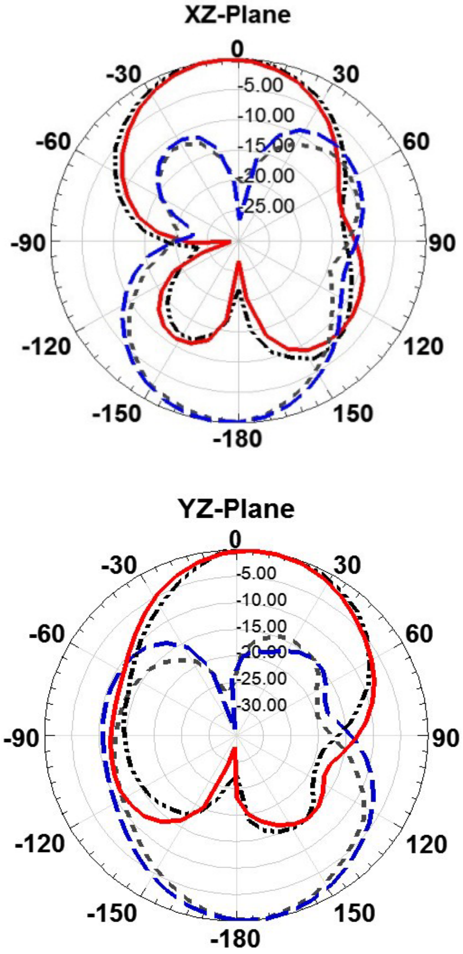

(a)

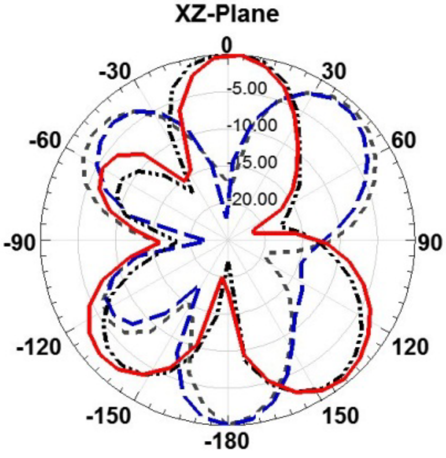

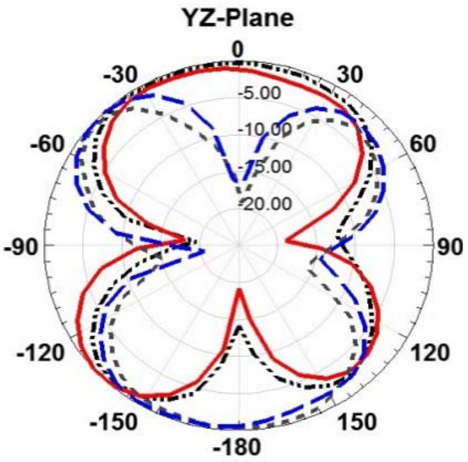

(b)

Simulated RHCP. ━━ Measured RHCP. ━ · ·
Simulated LHCP. ▬ ▬ Measured LHCP. ······

Fig. 8. Simulated and measured radiation patterns of the proposed antenna at (a) 4.2 GHz and (b) 6.5 GHz.

IV. CONCLUSION

A new wideband CPW-fed CPSSA has been proposed and implemented. By employing two arc-shaped and an inverted-L grounded strips CP radiation can be realized. The vertical tuning stub and step-shape gap between the feed line and the ground plane improved the impedance bandwidth. The horizontal grounded strip and the rectangular slit that are embedded in the left side of the feed line have effectively widened the 3 dB AR bandwidth apart from broadening impedance bandwidth. Experimental results show that the present proposed antenna has an impedance bandwidth of about 7 GHz (108 %) and a 3 dB AR bandwidth of about 3.7 GHz (76 %), which are greater than those obtained for similar designs. This antenna is suitable for IEEE 802.11a, (5150–5350 MHz / 5725–5825 MHz) and for IEEE 802.16, (3200–3800 MHz / 5200–5800 MHz).

REFERENCES

[1] J. Y. Sze and C. C. Chang, "Circularly polarized square slot antenna with a pair of inverted-L grounded strips," *IEEE Antennas Wireless Propag. Lett.*, vol. 7, pp. 149-151, 2008.

[2] J. Y. Sze, K. L. Wong, and C. C. Huang, "Coplanar waveguide-fed square slot antenna for broadband circularly polarized radiation," *IEEE Trans.*

Antennas Propag., vol. 51, no. 8, pp. 2141-2144, Aug. 2003.

[3] B. Yen Toh, R. Cahill, and V. F. Fusco, "Understanding and measuring circular polarization," *IEEE Trans. on Education*, vol. 46, no. 3, pp. 313-318, Aug. 2003.

[4] D. S. Javan and O. H. Ghouchani, "Cross slot antenna with u-shaped tuning stub for ultra wideband applications," *Appl. Comp. Electro. Society* (*ACES) Journal*, vol. 24, no. 4, pp. 427-432, Aug. 2009.

[5] Y. Lin, Y. Kao, S. Pan, and H. Chen, "Bidirectional radiated circularly polarized annular-ring slot antenna for portable RFID reader," *Appl. Comp. Electro. Society* (*ACES) Journal*, vol. 25, no. 3, pp. 182-189, Mar. 2010.

[6] J. Y. Sze, J. C. Wang, and C. C. Chang, "Axial-ratio bandwidth enhancement of asymmetric CPW-fed circularly-polarized square slot antenna," *Electronics Lett*., vol. 44, pp. 1048-1049, 2008.

[7] C. H. Chen, E. K. N. Yung, and B. J. Hu, "Miniaturized CPW-fed circularly polarized corrugated slot antenna with meander line loaded," *Electronics Lett.*, vol. 43, no. 25, pp. 1404-1405, Dec. 2007.

[8] M. J. Chiang, T. F. Hung, and S. S. Bor., "Dual-band circular slot antenna design for circularly and linearly polarized operations," *Microw. Opt. Technol. Lett*., vol. 52, no. 12, pp. 2717-2721, Dec. 2010.

[9] J. Y. Sze, C. I. G. Hsu, Z. W. Chen, and C. C. Chang, "Broad band CPW-fed circularly polarized square slot antenna with lightening-shaped feed line and inverted-L grounded strips," *IEEE Trans. Antennas Propag*., vol. 58, no. 3, pp. 973–977, Mar. 2010.

[10] J. Pourahmadazar, C. Ghobadi, J. Nourinia, N. Felegari, and H. Shirzad., "Broadband CPW-Fed circularly polarized square slot antenna with inverted-L strips for UWB applications," *IEEE Antennas Wireless Propag. Lett*., vol. 10, pp. 369-372, 2011.

[11] W. L. Stutzman and G. A. Thiele, *Antenna Theory and Design*, Wiley, New York, 1998.

Asghar Mousazadeh was born in Naghadeh, Iran in 1985. He received his B.Sc. degree in Electrical Engineering (Telecommunication) from Urmia University, Urmia, Iran, in 2010 and M.Sc. degree in Electrical Engineering (Telecommunication) from Islamic Azad University, Science and Research Branch, Tehran, Iran, in 2012. His primary research interests are in antenna design, and microwave components.

Mohammad Naser-Moghadasi was born in Saveh, Iran, In 1959. He received the B.Sc. degree in Communication Eng. in 1985 from the Leeds Metropolitan University (formerly Leeds polytechnic), UK. Between 1985 and 1987 he worked as an RF design engineer for the Gigatech Company in Newcastle Upon Tyne, UK. From 1987 to 1989, he was awarded a full scholarship by the Leeds educational authority to pursue an M. Phil. Studying in CAD of Microwave circuits. He received his Ph.D. in 1993, from the University of Bradford, UK. He was offered then a two years Post Doc. To pursue research on Microwave cooking of materials at the University of Nottingham, UK. From 1995, Dr. Naser-Moghadasi joined Islamic Azad University, Science & Research Branch, Iran, where he currently is head of postgraduate studies and also member of Central Commission for Scientific Literacy & Art Societies. His main areas of interest in research are Microstrip antenna, Microwave passive and active circuits, RF MEMS. Dr. Naser-Moghadasi is member of the Institution of Engineering and Technology, MIET and the Institute of Electronics, Information and Communication Engineers (IEICE). He has so far published over 130 papers in different journals and conferences.

Fatemeh Geran was born in Ghaemshar, Iran in 1977. She received her B.Sc. degree in Electrical Engineering (Telecommunication) from Tehran University, Tehran, Iran in 1999. Also, she received her M.Sc. and PhD degrees in Electrical Engineering (Telecommunication) from TarbiatModares University, Tehran, Iran, in 2003 and 2009, respectively. Her main areas of interest in research are antenna design, microwave passive and active circuits and filters. She is currently as an Assistant Professor in Electrical Engineering at Islamic Azad University- Science and Research Branch, Tehran, Iran.

Saeid Mohammadi was born in Urmia, Iran 1984. He received his B.Sc. and M.Sc. degrees in Electrical Engineering (Telecommunication) from Urmia University Urmia, Iran in 2008 and 2010, respectively. His primary research interests are in antenna design, numerical methods in electromagnetic, microwave components.

Payam Zibdoost was born, in khoy, Iran in 1985. He received his B.Sc. degree in Electrical Engineering (Telecommunication) from Urmia University Urmia, Iran, in 2009 and now he is a postgraduate student of Electrical Engineering (Telecommunication) in this university. His primary research interests are in antenna design, and microwave components.

Compact Broadband Printed Monopole Antenna

Amir Jafargholi [1] **and Ali Jafargholi** [2]

[1]Institute of Space Science and Technology
Amirkabir University of Technology, 424 Hafez Ave., P.O. Box: 15875-4413, Tehran, Iran
jafargholi@ieee.org

[2]Department of Electrical Engineering
Sharif University of Technology, Azadi Ave., P.O. Box: 11365-11155. Tehran, Iran
jafargholi@sharif.edu

Abstract **─** A compact printed monopole antenna for broadband application is presented. The proposed antenna, having a total physical size of 21 × 6.5 mm consists of a patch fed by a coaxial line and an SMA connector as partial finite ground plane. The modified patch plane with a slot in its feed point helps to increase the impedance bandwidth of the proposed antenna. The optimal design may offer an ultra-wide impedance bandwidth from 2.56 GHz to 20 GHz. A prototype is fabricated and tested. The agreement between the simulated and measured results is quite good.

Index Terms **─** Compact printed monopole antenna and ultra-wideband.

I. INTRODUCTION

Recently ultra-wideband (UWB: 3.1 GHz – 10.6 GHz) technology has received much attention and has become the most promising candidate for future short-range high-speed data communications. Designing UWB antennas to match various applications such as the wireless personal area network (WPAN), wireless body area network (WBAN), indoor localization, biomedical imaging, and UWB array applications [1] is still a major challenge and has attracted the interest of many researchers [2, 3].

There are many requirements for the UWB antennas, such as low profile, radiation stability, and constant gain. To obtain these requirements, several compact antennas have been proposed for UWB applications in three dimensional [4], and planar form [5]. However, for miniaturizing the system size, the UWB antenna must be small enough as an internal antenna to be easily embedded in a portable device. In such miniaturized structures, to overcome the matching problem, someone has to make a special effort [6, 7].

In this paper, a compact and very simple printed monopole antenna with a matching slot has been proposed. To the authors' best knowledge, present suggestion is the smallest antenna that was reported yet. This antenna provides not only an ultra wide operating bandwidth for UWB systems, but also good impedance bandwidth from 2.56 GHz to 20 GHz with acceptable gain throughout the band. This broadband characteristic of the proposed monopole antenna is confirmed in the measurements. The antenna group delay and transmission characteristics are quite stable to satisfy broadband operation.

II. ANTENNA DESIGN, SIMULATION, AND FABRICATION

The geometry of the proposed UWB printed monopole antenna is shown in Fig. 1 (a), which occupies a compact size of only 21 (*L*) × 6.5 (*W*) × 0.762 mm. The fabricated antenna, printed on an RT5880 substrate with a dielectric constant of 2.2, is composed of a simply rectangular-shaped radiator, optimally etched lateral slot and fed by a 50 Ω coaxial line through an SMA connector. The designed antenna was successfully implemented as shown in Fig. 1(b). The length of the planar monopole was chosen to be 21 mm, which easily

Submitted On: May 9, 2012
Accepted On: March 28, 2013

makes the obtained impedance bandwidth have a lower edge frequency f_L less than 2.56 GHz. The parameters of the feeding strips were also optimized to achieve a maximum impedance bandwidth.

By adjusting "*d*", the coupling between the ground plane and the lower edge of the planar monopole is varied, which effectively introduces a variation in the input reactance of the antenna. Thus, impedance matching of the antenna can be fine-tuned, and optimized impedance bandwidth can be obtained for the antenna. The effects of slot and patch truncation have been shown in Fig. 2. The optimized antenna is capable of tuning from 2.56 GHz to 20 GHz providing an impedance bandwidth of about 7.8:1. Experimental results are also presented in Fig. 2. In this figure, we labeled the truncated slotted planar monopole antenna as Type I, while the slotted antenna is labeled as Type II (without truncation), and the antenna with nor the slot neither the truncation as Type III.

The measured results are in good agreement with those of the simulation. Despite its very small size, the proposed antenna has achieved wider bandwidth than the antennas reported in [3] and is able to tune over a wide bandwidth to cover the entire range 3.1 GHz to 10.6 GHz assigned for UWB applications. For UWB antenna systems, the group delay is a useful parameter to measure the variation of the phase response against frequency. The group delay of an antenna can be calculated from the derivative of the phase response of the transfer function with respect to frequency.

Figure 2 also shows the group delay results as calculated from the time domain responses, in CST Microwave Studio, which reveals less than 0.8 ns fluctuations in the group delay across the UWB, [8-10]. Apparently, smaller variations of the group delay occur for the truncated slotted antenna. It seems clearly that the slot is mainly affecting the impedance tuning condition while the patch truncation modifies the group delay response. Figure 3 shows the simulation results for the E- and H-planes radiation pattern at 3 GHz, 5 GHz, 10 GHz, 15 GHz, and 20GHz. It can be observed that the radiation pattern of the proposed antenna is monopole-like while the frequency is below 10 GHz and becomes broadside gradually in the higher frequencies. The measured co- and cross- components of the radiation pattern for some sample frequency only in E-plane for brevity are plotted in Fig. 4.

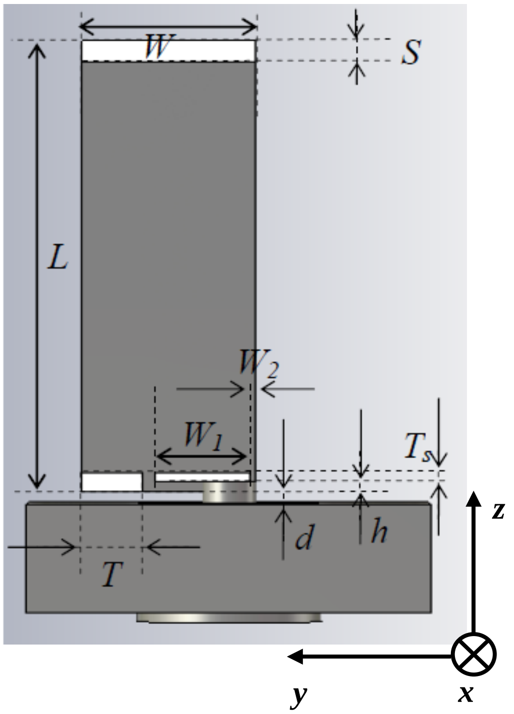

(a)

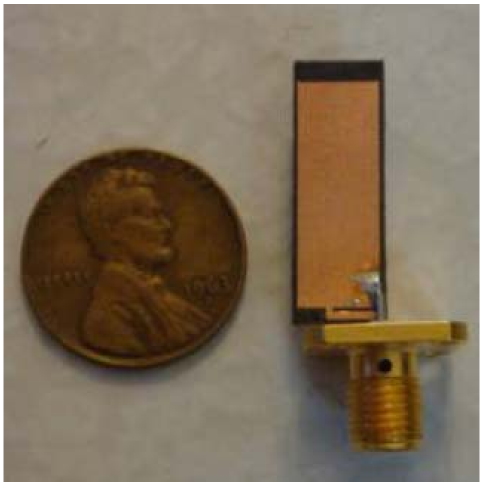

(b)

Fig. 1. (a) Antenna geometry and (b) photograph of measured antenna of dimensions: L = 21 mm, W= 6.5 mm, W_1 = 3.5 mm, W_2 = 0.25 mm, T = 2.25 mm, T_s = 0.4 mm, S = 0.5 mm, and d = 0.25 mm.

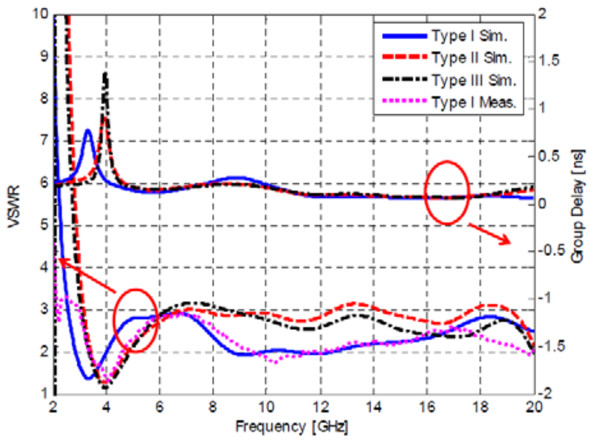

Fig. 2. Measured and simulated VSWR for both proposed and simulated antenna group delay.

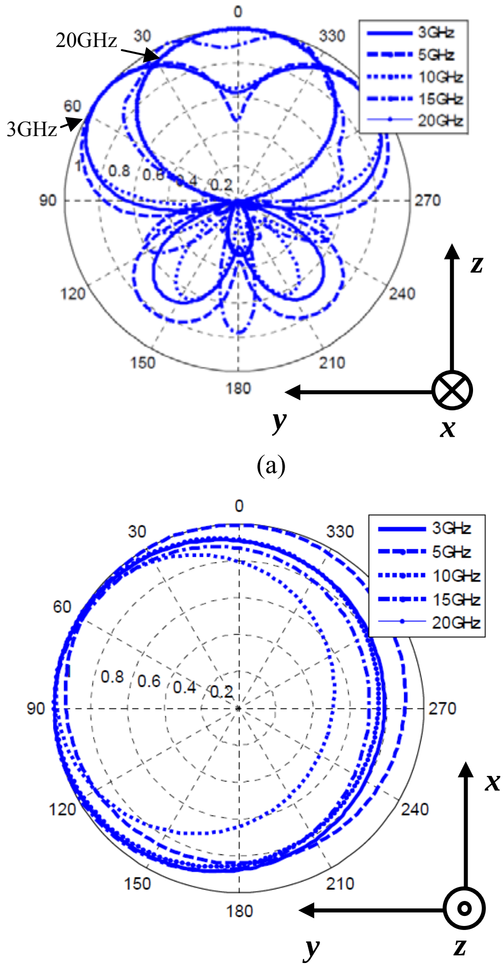

(a)

(b)

Fig. 3. Simulated normalized radiation patterns, (a) E-Plane and (b) H-Plane.

The measurements were made using a meter length of phase stable test cable. Moving a hand along this cable visibly perturbed the return loss display, indicating that the cable supported currents from the antenna. Current traveling from the ground down the feed cable is a very common phenomenon with monopole antenna designs. To achieve high levels of feed cable isolation in monopole-type designs, the use of current-choking techniques and careful placement of the feed cable connector have often been necessary. In commercial use, the antennas are normally operated connected directly to the transceiver PCB, and therefore the feed cable coupling is not an issue, [11].

The radiation pattern looks like a doughnut, similar to a monopole pattern, at the first resonant frequency, as shown in Fig. 4 (a). At the second frequency, the pattern looks like a slightly pinched donut with the gain increase around $\theta=45^0$, Fig. 4 (b). Above the end of the standard UWB band and at the higher frequencies, the patterns are squashed in azimuth and humps form in the up-right directions (gain increasing), as shown in Figs. 4 (d) – 4 (e). The E-plane patterns have large back lobes and look like a doughnut or a slightly pinched doughnut at lower frequencies. With the increase of the frequency, the back lobes become smaller, splitting into many minor ones, while the front lobes start to form humps and notches.

It is also noticed that the patterns on the H-plane are almost omnidirectional at lower frequencies and become distorted at the end of the band. The asymmetry of the patterns for the E- and H-planes components is caused mainly by the asymmetrical feed configuration. Also, the severe asymmetry of the monopole causes degradation of the omnidirectional radiation patterns of the E-plane components in the azimuth plane, as shown in Fig. 4 (c). This degradation becomes worse when the operating frequency increases. As shown in Figs. 4 (a) – 4 (e), the measured radiation patterns are almost close to those obtained in the simulation (i.e., Fig. 3). This has verified the simulated radiation patterns. However, the measured E-plane pattern does not agree well with the simulation. This discrepancy seems to be due to an enhanced perturbing effect on the antenna performance caused by the feeding structure and cable at this frequency.

Moreover, from the comparison of the fabricated prototype to the simulated geometry of Fig. 1, it is clear that some of the asymmetry in the measured patterns as compared to the symmetry in the simulated patterns could be attributed to the offset in the ground plane afforded by the physical SMA connector. The ground plane in the simulation extends beyond the edge of the printed component of the antenna whereas the actual SMA stops at approximately the width of the slot (W_1).

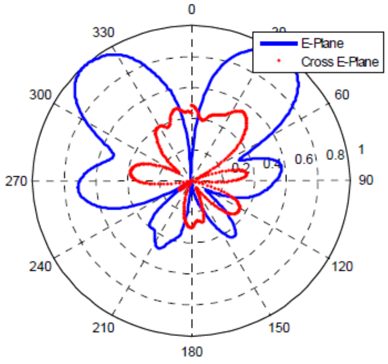

(a)

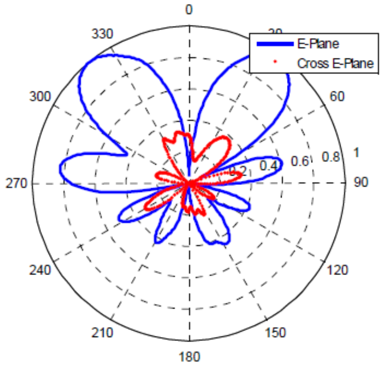

(b)

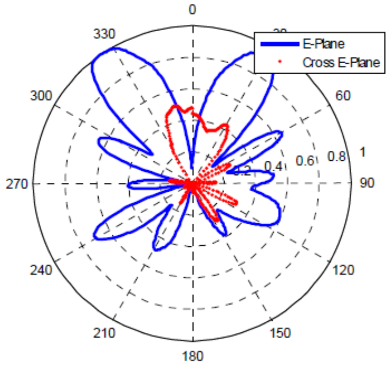

(c)

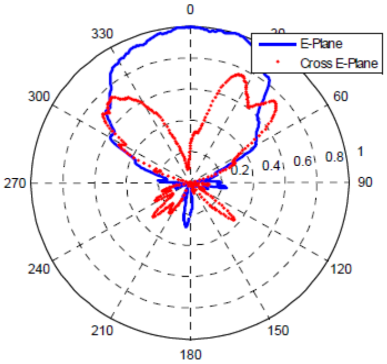

(d)

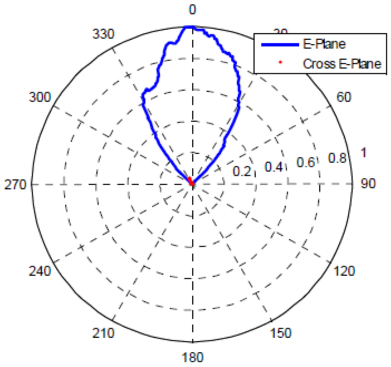

(e)

Fig. 4. Measured normalized E-plane radiation patterns at (a) 3 GHz, (b) 5 GHz, (c) 10 GHz, (d) 15 GHz, and (e) 20 GHz.

The transition of the radiation patterns from a simple doughnut pattern at the first resonance to the complicated patterns at higher harmonics indicates that this antenna must have gone through some major changes in its behavior; however, the antenna gain variation is less than 2 dB through the whole frequency band (simulation results at main lobe direction, $\theta = 60^0$), as shown in Fig. 5.

As it can be seen in Fig. 5, the antenna radiation gain is approximately flat at the antenna main lobe, while its variation is high in both azimuth and elevation angles. This behavior is due to much more uniform current distribution in the lower frequencies versus higher ones (see Fig. 6). In this figure, the poynting vector has been shown at 3 GHz, 5 GHz, 10 GHz, 15 GHz, and 20 GHz. This figure confirms the transition of the radiation patterns as described before.

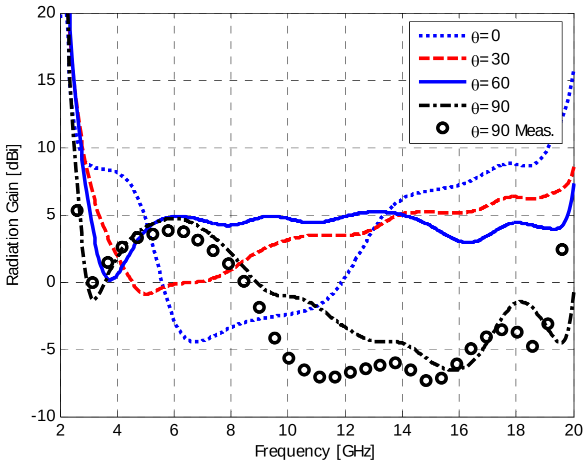

Fig. 5. Antenna gain at different elevation angles.

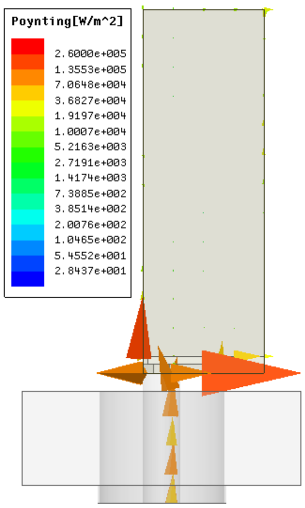

(a)

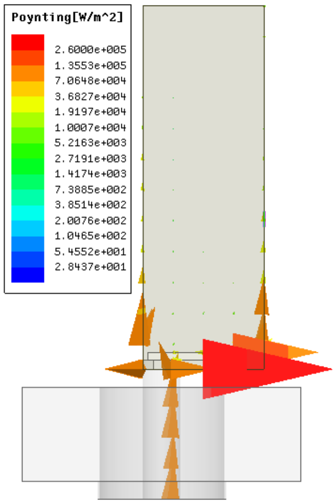

(b)

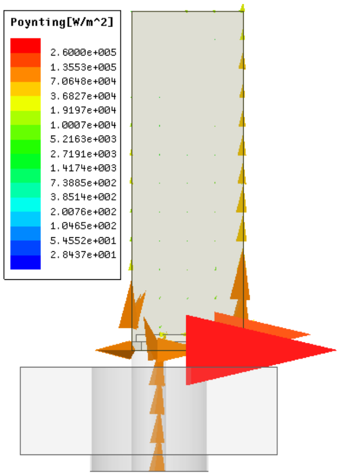

(c)

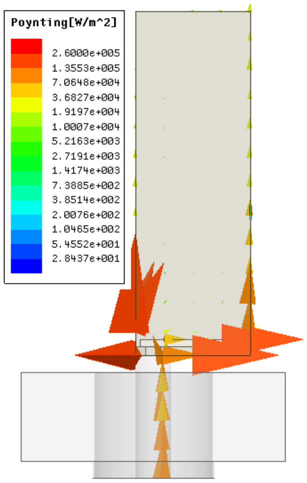

(d)

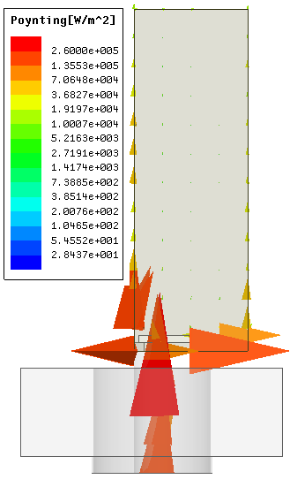

(e)

Fig. 6. Simulation results for normal pointing vector at (a) 3 GHz, (b) 5 GHz, (c) 10 GHz, (d) 15 GHz, and (e) 20 GHz.

III. CONCLUSION

A printed compact monopole antenna has been proposed and fabricated for broadband applications, while the antenna has a total size of 21 mm × 6.5 mm. The antenna composed of patch plane with etched slot on the bottom edge helps to increase the impedance bandwidth. It is observed from measurements that the proposed antenna with the optimally etched slot has achieved an impedance bandwidth of 17.0 GHz (2.56 GHz to 20 GHz), which covers the entire UWB band.

REFERENCES

[1] J. R. Verbiest and G. A. E. Vandenbosch, "A novel small-size printed tapered monopole antenna for UWB WBAN," *IEEE Antennas Wirel. Propag. Lett.*, vol. 5, pp. 377-379, 2006.

[2] A. Jafargholi, M. Kamyab, and M. Veysi, "Spiral array architecture, design, synthesis and application," *IET Microwave Antenna Propag.*, vol. 5, pp. 503-511, 2011.

[3] R. Azim, M. T. Islam, and N. Misran, "Ground modified double-sided printed compact UWB antenna," *Electron. Lett.*, vol. 47, no. 1, pp. 9-11, 2011.

[4] K. L.Wong, C. H. Wu, and S. W. Su, "Ultrawide-band square planar metal-plate monopole antenna with a trident-shaped feeding strip," *IEEE Trans. Antenna Propag.*, vol. 53, no. 4, pp. 1262-1269, 2005.

[5] H. W. Liu and C. F. Yang, "Miniature hook-shaped monopole antenna for UWB applications," *Electron. Lett.*, vol. 46, no. 4, pp. 265-266, 2010.

[6] S. Akira, O. Yuji, H. Kazuhiko, and T. Kouji, "Miniaturized ultra-wideband self-complementary antennas using shunted spiral inductors," *Microwave Symposium Digest, 2008 IEEE MTT-S International*, pp. 1211-1214, 2008.

[7] S. Radiom, H. Aliakbarian, G. A. E. Vandenbosch, and G. G. E. Gielen, "An effective technique for symmetric planar monopole antenna miniaturization," *IEEE Trans. Antennas Propag.*, vol. 57, no. 10, pp. 2989-2996, Oct. 2009.

[8] A. M. Abbosh, "Miniaturization of planar ultrawideband antenna via corrugation," *IEEE Antennas Wirel. Propag. Lett.*, vol. 7, pp. 685-688, 2008.

[9] A. M. Abbosh, "Miniaturized microstrip-fed tapered-slot antenna with ultrawideband performance," *IEEE Antennas Wirel. Propag. Lett.*, vol. 8, pp. 690-692, 2009.

[10] G. Ruvio and M. J. Ammann, "A miniaturized antenna for UWB-based breast imaging," *3rd European Conference on Antennas and Propagation, EuCAP*, pp. 1864-1867, 2009.

[11] C. Icheln, *Method for Measuring RF Radiation Properties of Small Antennas*, Ph.D. Thesis, Helsinki University of Technology, Oct. 2001.

Amir Jafargholi received the PhD degree in Electrical Engineering from K.N. Toosi University of Technology, Tehran, Iran, in 2011. He is the coauthor of about 50 scientific contributions published in international books, journals and peer-reviewed conference proceedings. His research interest includes the applications of metamaterials in the analysis and synthesis of antennas. Dr. Jafargholi was a recipient of a Student's Best Thesis National Festival award for his B.Sc. thesis, on May 2006. He was a recipient of the 22th Khawarizmi International and 13th Khawarizmi Youth Award on Jan. 2009 and Oct. 2011, respectively. He was also the recipient of Research Grant Awarded in Metamaterial 2010.

Ali Jafargholi was born in Tehran, Iran, on November 3, 1989. He received the B.Sc. degree in Electrical Engineering from Sharif University of Technology, Tehran, Iran, in 2012, and is currently working toward the M.Sc. degree in Communication Engineering. His research interests include metamaterial applications to antenna designs.

A Novel Design of Dual Band-Notched Slot Antenna Using a Pair of Γ-Shaped Protruded Strips for UWB Applications

Mohammad Ojaroudi [1], Nasser Ojaroudi [2], and Noradin Ghadimi[1]

[1] Young Researchers Club
Ardabil Branch, Islamic Azad University, Ardabil, Iran
m.ojaroudi@iauardabil.ac.ir and noradin.ghadimi@gmail.com

[2] Department of Electrical Engineering
Ardabil Branch, Islamic Azad University, Ardabil, Iran
n_ojaroudi@srttu.edu

Abstract **─**In this paper, we present a novel design of dual band-notch printed slot antenna for UWB applications. The antenna consists of a square radiating stub and a ground plane structure with an H-shaped slot and a pair of Γ-shaped strips protruded inside rectangular slot, which provides a wide usable fractional bandwidth of more than 145% (2.49 GHz – 15.73 GHz). In order to increase the impedance bandwidth of the ordinary slot antenna, we use an H-shaped slot in the ground plane, through which an UWB frequency range can be achieved. Additionally, by using a protruded Γ-shaped strip in the top edge of the rectangular slot a single frequency band-stop performance can be achieved, also in order to create the second notch frequency, we insert the second protruded Γ-shaped strip in the bottom edge of the rectangular slot. Simulated and measured results obtained for this antenna show that the proposed slot antenna offers two notched bands, covering all the 5.2/5.8 GHz WLAN, 3.5/5.5 GHz WiMAX and 4 GHz C-band range. The antenna has a small dimension of 20×20 mm^2.

Index Terms **─** H-shaped slot, microstrip-fed slot antenna, protruded Γ-shaped strip, and ultra-wideband (UWB) applications.

I. INTRODUCTION

Communication systems usually require smaller antenna size in order to meet the miniaturization requirements of radio-frequency (RF) units [1]. In UWB systems, the improvement of the impedance bandwidth, which does not involve a modification of the geometry of the planar antenna, has been investigated, and growing research activity is being focused on them. As important compact UWB antennas, printed slot antennas have attracted more and more attention. Consequently, a number of planar slots with different geometries have been experimentally characterized [2-6].

In this paper, a new dual band-notched microstrip-fed slot antenna is presented. In the presented antenna, an H-shaped slot was used for bandwidth enhancement and two Γ-shaped strip protruded inside the rectangular slot on the ground plane were applied in order to generate dual bad-notch function. The size of the designed antenna is smaller than the UWB antennas with band-notched function reported recently [4-7]. Simulated and measured results are presented to validate the usefulness of the proposed antenna structure for UWB applications.

II. ANTENNA DESIGN

The presented small slot antenna fed by a 50Ω microstrip line is shown in Fig. 1, which is printed on an FR4 substrate of thickness 0.8 mm, permittivity 4.4, and loss tangent 0.018. The basic slot antenna structure consists of a square stub, a feed line, and a ground plane. The square stub is connected to a 50Ω microstrip feed line. On the

Submitted On: April 28, 2012
Accepted On: Dec. 26, 2012

other side of the substrate, a conducting ground plane is placed. The proposed antenna is connected to a 50 Ω SMA connector for signal transmission. The final dimensions of the proposed designed antenna are shown in Table 1.

In this design, to achieve a new additional resonance frequency and give a bandwidth enhancement performance, we use an H-shaped slot on the ground plane. Based on defected ground structure (DGS), the modified H-shaped slot acts as an impedance matching element that controls the impedance bandwidth of the proposed antenna. This is because it can create additional surface current paths in the antenna; therefore additional resonance is excited and hence much wider impedance bandwidth can be produced, especially at higher bands [8].

Additionally, in this study, the proruded Γ-shaped strips in the ground plane perturb the resonant response and act as half-wave filtering element to generate a new notch frequency, because it can creates additional surface current path in the feed line. At the notch frequency, the current flows are more dominant around the proruded Γ-shaped strips, and they are oppositely directed between the protruded strips and the ground plane [9]. As a result, the desired high attenuation near the notch frequencies can be produced.

Table 1: The final dimensions of the designed antenna.

Param.	mm	Param.	mm	Param.	mm
W_{Sub}	20	L_{Sub}	20	h_{sub}	0.8
L_f	4	W_f	1.5	W	7
L_S	11	W_S	18	W_1	1.5
L_1	6	W_2	0.5	L_2	5
W_3	0.4	L_3	5.5	W_4	0.5
L_4	8	L_5	8.6	L_6	8.5
W_H	2	L_H	4	W_{H1}	1
L_{H1}	1.5	L_{gnd}	4		

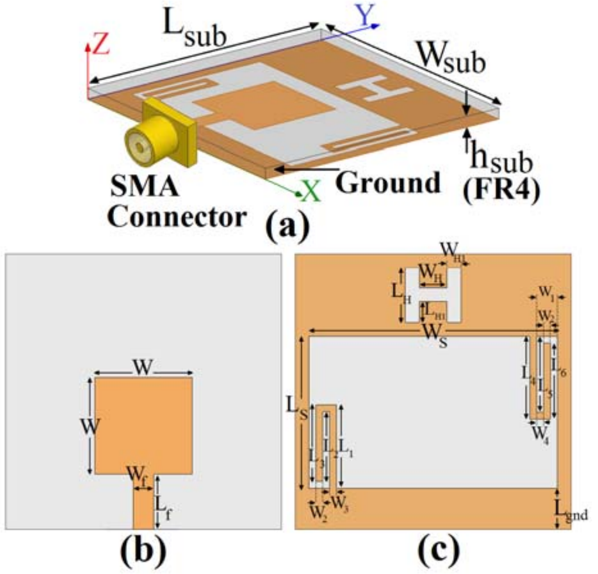

Fig. 1. Geometry of the proposed microstrip-fed slot antenna, (a) side view, (b) top layer, and (c) bottom layer.

III. RESULTS AND DISCUSSIONS

In this section, the microstrip slot antenna with various design parameters was constructed, and the numerical and experimental results of the input impedance and radiation characteristics are presented and discussed. The parameters of this proposed antenna are studied by changing one parameter at a time and fixing the others. The simulated results are obtained using the Ansoft simulation software high-frequency structure simulator (HFSS) [10].

Various antenna structures used for simulation studies are shown in Fig. 2. The VSWR characteristics of the ordinary slot antenna (Fig. 2 (a)), ordinary slot antenna with an H-shaped slot in the ground plane (Fig. 2 (b)), and the proposed antenna structure (Fig. 2 (c)) are compared in Fig. 3. As shown in Fig. 3, in the proposed antenna configuration, the ordinary slot can provide the fundamental and next higher resonant radiation band at 4.1 GHz and 8.5 GHz, respectively. To design a novel antenna, also in order increase the upper frequency bandwidth, an H-shaped slot is inserted in the ground plane as displayed in Fig. 2 (b). As shown in Fig. 3, the upper frequency bandwidth is significantly affected by using the H-shaped slot. It is found that the H-shaped slot itself is radiating at higher frequencies (10.3 GHz). Therefore by using this slot, the third resonance occurs at 10.3 GHz in the simulation. This behaviour is mainly due to the change of surface current path by the dimensions of a pair of H-shaped slots in the ground plane [2]. Also by using two proruded Γ-shaped strips in the ground plane, the dual band-notch function can be achieved, which cover all the 5.2/5.8GHz WLAN, 3.5/5.5 GHz WiMAX, and 4 GHz C-band [11].

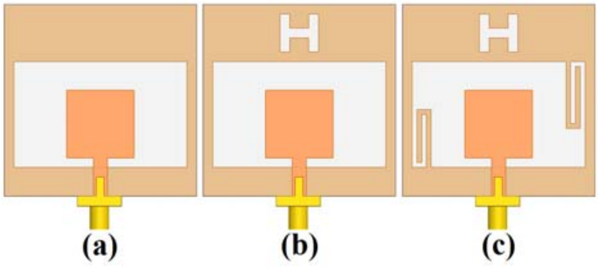

Fig. 2. (a) The basic structure (ordinary slot antenna), (b) antenna with an H-shaped slot in the ground plane, and (c) the proposed antenna.

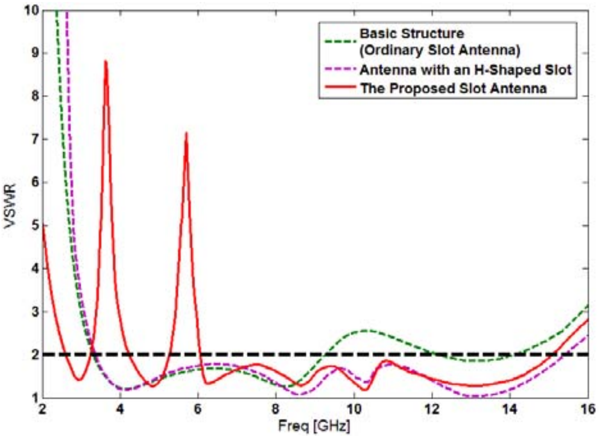

Fig. 3. Simulated VSWR characteristics for the antennas shown in Fig. 2.

In order to know the phenomenon behind this additional resonance performance, the simulated current distributions on the ground plane for the ordinary slot antenna with an H-shaped slot at 10.3 GHz (new additional resonance) are presented in Fig. 4 (a). It can be observed in Fig. 4 (a), that the current is concentrated on the edges of the interior and exterior of the H-shaped slot at the 10.3 GHz. Other important design parameters of this structure are two proruded Γ-shaped strips, used in the rectangular slot. Figures 4 (b) and 4 (c) present the simulated current distributions on the ground plane for the proposed antenna structure at the first notched frequency (3.8 GHz) and the second notched frequency (5.5 GHz), respectively. As shown in Figs. 4 (b) and 4 (c), at these notch frequencies the current flows are more dominant around of the two proruded Γ-shaped strips. As a result, the desired high attenuation near the notched frequencies can be produced [12-13].

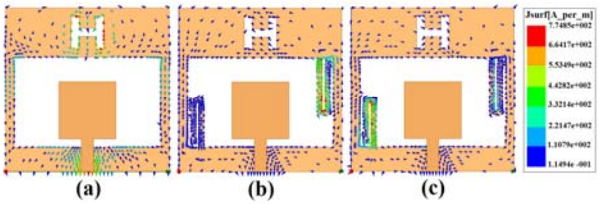

Fig. 4. Simulated surface current distributions on the ground plane for (a) ordinary slot antenna with an H-shaped slot in the ground plane at 10.3 GHz (new additional resonance frequency), (b) for the proposed antenna structure at 3.85 GHz (first notch frequency), and (c) at 5.5 GHz (second notch frequency).

The simulated radiation efficiencies and maximum gains of the proposed antenna are shown in Fig. 5. Results of the calculations using the HFSS software indicated that the proposed antenna features a good efficiency, being greater than 82 % across the entire radiating band except in two notched bands. On the other hand, the simulated radiation efficiencies of the proposed dual band-notched antenna, at 3.85 GHz and 5.5 GHz, are only about 34 % and 27 %, respectively. Also, the simulated maximum gains of the proposed antenna are presented in Fig. 5. It can be observed from Fig. 5 that by using a square radiating patch with proposed slots, two sharp decrease of maximum gain in the notched frequencies band at 3.85 GHz and 5.5 GHz are shown. As shown in Fig. 5, the radiation efficiency has a slight drop at higher frequencies. This drop between low and high frequency patterns' results is mostly due to FR4 substrate loss at high frequencies [14].

Figure 6 shows the measured and simulated VSWR characteristics of the proposed antenna. The fabricated antenna has the frequency band of 2.49 GHz to over 15.73 GHz with two rejection bands around 3.67 GHz – 4.15 GHz and 5.01 GHz

– 5.98 GHz. As shown in Fig. 6, there exists a discrepancy between measured data and simulated results; this could be due to the effect of the SMA port, and also the accuracy of the simulation is due to the wide range of simulation frequencies. In order to confirm the accurate VSWR characteristics for the designed antenna, it is recommended that the manufacturing and measurement process need to be performed carefully.

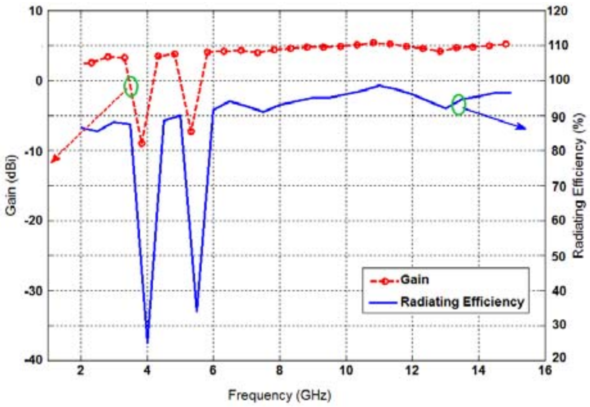

Fig. 5. Simulated radiation efficiency and maximum gain values of the proposed slot antenna.

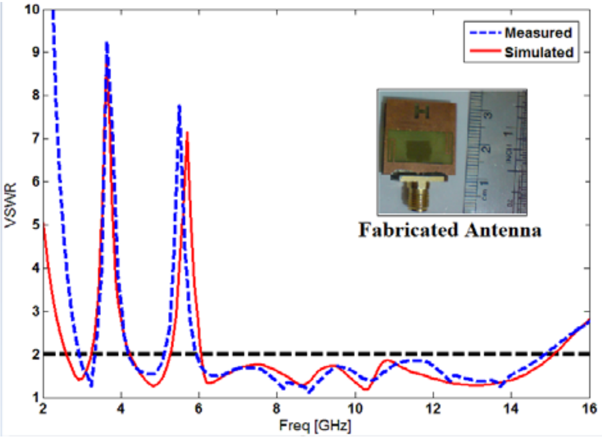

Fig. 6. Measured and simulated VSWR for the proposed antenna with a picture of the fabricated antenna.

Figure 7 shows the measured radiation patterns including the co- and cross-polarizations in the *H*-plane (*x*-*z* plane) and *E*-plane (*y*-*z* plane), respectively. It can be seen that the radiation patterns in *x*-*z* plane are nearly omnidirectional for the three frequencies.

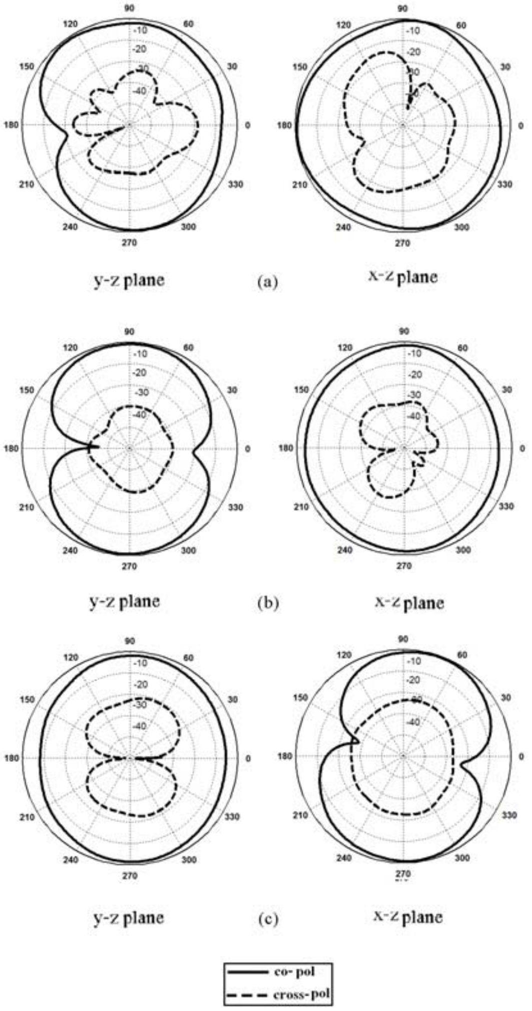

Fig. 7. Measured radiation patterns of the proposed antenna for (a) 4.5 GHz, (b) 7.5 GHz, and (c) 10 GHz.

IV. CONCLUSION

In this paper, a novel compact wideband printed slot antenna (PSA) with single and dual band-notched characteristics has been proposed for various UWB applications. The fabricated antenna has the frequency band of 2.49 GHz to over 15.73 GHz with two rejection bands around 3.67 GHz – 4.15 GHz and 5.01 GHz –5.98 GHz. By cutting an H-shaped slot in the ground plane, additional resonance is excited and hence much wider impedance bandwidth can be produced, especially at the higher band. Moreover, by using two protruded Γ-shaped strips with variable dimensions on the ground plane, dual band notch characteristics are generated. The designed antenna has a small size. Good VSWR and radiation pattern characteristics are obtained in the frequency band of interest. Simulated and experimental results show that the proposed antenna could be a good candidate for UWB applications.

ACKNOWLEDGMENT

The authors are thankful to Microwave Technology (MWT) company staff for their beneficial and professional help (www.microwave-technology.com).

REFERENCES

[1] H. Schantz, *The art and Science of Ultra Wideband Antennas*, Artech House 2005.

[2] M. Ojaroudi, S. Bashiri, N. Ojaroudi, and M. T. Partovi, "Octave-band, multi-resonance CPW-fed small slot antenna for UWB applications," *Electronic Lett*., vol. 48, no. 16, pp. 980-982, 2012.

[3] J. Y. Sze and K. L. Wong, "Bandwidth enhancement of a microstrip line-fed printed wide-slot antenna," *IEEE Trans. Antennas Propag.*, vol. 49, pp. 1020-1024, 2001.

[4] M. Ojaroudi, N. Ojaroudi, and Y. Ebazadeh, "Dual band-notch small square monopole antenna with enhanced bandwidth characteristics for UWB applications," *Appl. Comp. Electro. Society (ACES) Journal*, vol. 27, no.5, pp. 420-426, May 2012.

[5] B. Hadian, M. Ojaroudi, and N. Ojaroudi, "Enhanced bandwidth small square monopole antenna with band-notched functions for UWB wireless communications," *Appl. Comp. Electro. Society (ACES) Journal*, vol. 27, no. 9, pp. 759-765, Sep. 2012.

[6] R. Azim, M. T. Islam, and N. Misran, "Design of a planar UWB antenna with new band enhancement technique," *Appl. Comp. Electro. Society (ACES) Journal*, vol. 26, no. 10, pp. 856-862, Oct. 2011.

[7] J. William and R. Nakkeeran, "A new UWB slot antenna with rejection of WiMax and WLAN bands," *Appl. Comp. Electro. Society (ACES) Journal*, vol. 25, no. 9, pp. 787-793, Sep. 2010.

[8] Y. W. Jang, "Experimental study of large bandwidth three-offset microstrip line-fed slot antenna," *IEEE Microw. Wireless Comp. Lett*., vol. 11, pp. 425-426, 2001.

[9] D. S. Javan and O. H. Ghouchani, "Cross slot antenna with U-shaped tuning stub for ultra wideband applications," *Appl. Comp. Electro. Society (ACES) Journal*, vol. 24, no. 4, pp. 427-432, August 2009.

[10] Ansoft High Frequency Structure Simulation (HFSS), Ver. 10, Ansoft Corporation, 2005.

[11] N. Ojaroudi and M. Ojaroudi, "Dual band-notch slot antenna by using a pair of Γ-shaped slits and Ω–shaped parasitic structure for UWB applications," *Microw. Opt. Technol. Lett.*, vol. 55, pp. 102-105, 2013.

[12] N. Ojaroudi, M. Ojaroudi, and H. Ebarhimian, "Band-notched UWB microstrip slot antenna with enhanced bandwidth by using a pair of C-shaped slots," *Microw. Opt. Technol. Lett.*, vol. 54, pp. 515-518, 2012.

[13] N. Ojaroudi and M. Ojaroudi, "Dual band-notch square monopole antenna with a modified ground plane for UWB applications," *Microw. Opt. Technol. Lett*., vol. 54, pp. 2743-2747, 2012.

[14] M. N. Jahromi and N. K. Barchloui, "Analysis of the behavior of Sierpinski carpet monopole antenna," *Appl. Comp. Electro. Society (ACES) Journal*, vol. 24, no. 1, pp. 32-36, Feb. 2009.

Mohammad Ojaroudi was born in 1984 in Germi, Iran. He received his B.Sc. degree in Electrical Engineering from Azad University, Ardabil Branch and M.Sc. degree in Telecommunication Engineering from Urmia University. Since 2010, he has been working towards his Ph.D. degree at Shahid Beheshti University. From 2007 until now, he has been a Teaching Assistant with the Department of Electrical Engineering, Islamic Azad University, Ardabil Branch, Iran. Since March 2008, he has been a Research Fellow (Chief Executive Officer) in the Microwave Technology Company (MWT), Tehran, Iran. In 2012, Mr. Ojaroudi became a member of the IEEE Transaction on Antennas and Propagation (APS) reviewer group. His research interests include analysis and design of microstrip antennas, design and modeling of microwave structures, radar systems, and electromagnetic theory. He is the author and coauthor of more than 100 journal and international conferences papers. His papers have more than 300 citations with 10 h-index.

Nasser Ojaroudi was born on 1986 in Germi, Iran. He received his B.Sc. degree in Electrical Engineering from Islamic Azad University, Ardabil Branch. Since 2011, he has been working toward the M.Sc. degree in Telecommunication Engineering at Shahid Rajaee Teacher Training University. Since March 2008, he has been a Research Fellow in the Microwave Technology (MWT) Company, Tehran, Iran. His research interests include ultra-wideband (UWB) microstrip antennas and band-pass filters (BPF), reconfigurable structure, design and modeling of microwave device, and electromagnetic wave propagation. He is author and coauthor of more than fifty journal and international conference papers.

Noradin Ghadimi was born in ardabil-Iran in 1985, and received the B.Sc. degree in Electrical Engineering from the Islamic Azad University, Ardabil Branch, Ardabil, Iran, in 2009 and the M.Sc. degree in Electrical Engineering from the Islamic Azad University Ahar Branch, Ahar, Iran , in 2011. His research interests include power system protection, modeling and analysis of distributed generations, renewable energy and communications systems.

Compact 3-D Multilayer Substrate Integrated Circular and Elliptic Cavities (SICCs and SIECs) Dual-mode Filter with High Selectivity

Z. -G. Zhang, Y. Fan, and Y. -H. Zhang

Fundamental Science on Extreme High Frequency Key Laboratory
University of Electronic Science and Technology of China, Chengdu 611731, China
freemanzg@yahoo.com.cn, fanyong@ee.uestc.edu.cn, yhzhang@ee.uestc.edu.cn

Abstract ─ In this paper a multilayer dual-mode complementary filter is developed based on the substrate integrated circular and elliptic cavity (SICC and SIEC). The filter is constructed with a SICC and double SIECs, and each cavity supports two degenerate modes, which can be generated and controlled by the coupling aperture and the slot located between layers. With multilayer topology, the structures can exhibit vertical coupling between vertically stacked dual-mode cavities. It does not only have the good performance, but also reduces the circuit size much more. Moreover, sharp transition characteristic in both the lower side and the upper side demonstrates high selectivity of the filter. Good agreement is obtained between the simulated and measured results of the proposed structure.

Index Terms ─ Dual-mode filter, elliptic cavity, high selectivity, multilayer, substrate integrated circular cavity (SICC), and transmission zeros (TZs).

I. INTRODUCTION

Compact RF/microwave filters with high performance are key components, which are finding increasing application in modern wireless communication systems. Recently, substrate integrated waveguides (SIW) have been proposed [1-6], and applied to develop many high-quality components. Furthermore, the SIW provides a promising solution to low cost, low profile, and low weight, while high performance is maintained. Usually, SIW filters are made from rectangular cavities [1-3]. In [1], cross-coupling was provided by higher order modes in cavities. Due to the transmission zeros are far away from the passband, steep transition band was hard to realize. A compact SIW filter with defected ground structure (DGS) was proposed in [2]. However, the substrate integrated circular cavity (SICC) and elliptic cavity (SIEC) are both good choices in the design of high performance filter [4-9]. They not only have the same attractiveness as classical SIW filters [10, 11], but also present a higher quality factor and lower loss. In [4], a new topology of coupling between SICCs was designed to produce particular filtering functions. In [8], a planar diplexer was developed based on the dual-mode SICCs. However, the SIW technology faces a new problem about the circuit size. Recently, the dual-mode technology [8, 9, 12] has been introduced in the design of SIW filter to meet the requirements in size reduction. The dual-mode concept consists of using a pair of resonant modes within a single physical cavity, which not only reduces the circuit size more than half but also adds the design flexibility. On the other hand, the multilayer technology has become important, and is also another efficient way to achieve a compact circuit. In a 3-D multilayer substrate, more SIW circuits can be synthesized and accommodated into different layers and the coupling among them can easily be implemented to construct novel functional and compact structures. Therefore, the dual-mode and multilayer techniques can be combined together to achieve more compact SIW circuits. In [5], a fourth-order multilayer cross-coupled circular cavity filter was proposed. A Ka-band band pass filter has been proposed in [9] using dual-mode SICCs. A coupling via placed in the cavities was used to perturb the two degenerate modes. But, the via located in SICCs also

Submitted On: April 10, 2012
Accepted On: Nov. 25, 2012

decreased the quality factor of cavities, and the four layers circuit demonstrated an insertion loss of 2.95 dB and the stop-band rejection is below 25 dB. To achieve higher selectivity, an additional dual-mode SICC can be introduced in the above structure without increasing the circuit size. However, the lower sideband rejection can not be increased significantly because a SICC contributes only to the two transmission zeros (TZs) located at the upper side band. Interestingly, a SIEC exhibits quite different characteristic compared with a SICC. TZs are located in the lower side response of the elliptic cavity. Therefore, the SICC and SIEC techniques can be employed together to achieve multilayer complementary filter with higher performance.

In this paper, dual mode SICC and double SIECs are introduced in the 3-D multilayer SIW circuits and a compact dual-mode complementary filter with low loss, elliptic response and high selectivity have been achieved. The orientations of coupling aperture and slot relative to the major axis of the SIEC can be adjusted to generate two degenerate modes. Meanwhile, it is possible to control the bandwidth and the rejection level by adjusting parameters of the arc-shaped slot. The proposed structure is not only very compact, but has lower insertion loss, high selectivity and better stop-band rejection (> 50 dB). Moreover, it can be found that both the upper and the lower side response of the filter are very steep.

II. FILTER ANALYSIS AND DESIGN

A. Multilayer dual-mode complementary filter

As shown in Fig. 1, a SICC and double SIECs with three layers have been introduced to improve the performance of the filter. The first and last layers are used for input/output port. Three dual mode cavity resonators are coupled through arc-shaped coupling slots in metal layer 2 or layer 3. In these figures, W_C and W_S are the width of the coupling aperture and slot, respectively, θ is the central angle of the coupling slot, R_a and R_b are the semi-major and semi-minor axis of SIEC, respectively. While the symbol W_g is the width of the input and output SIWs. The symbol R is the radius of the SICC.

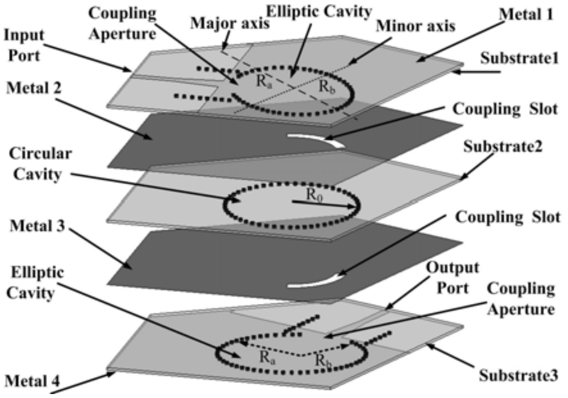

(a) Anatomy view

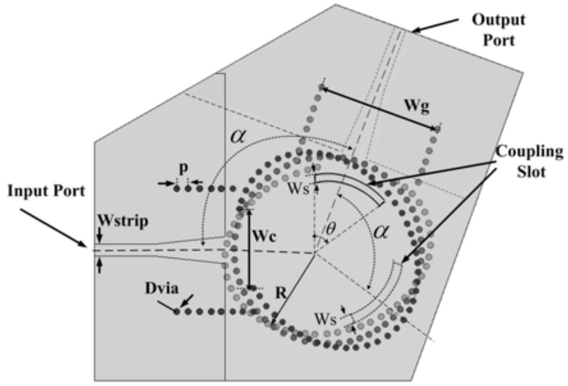

(b) Top view

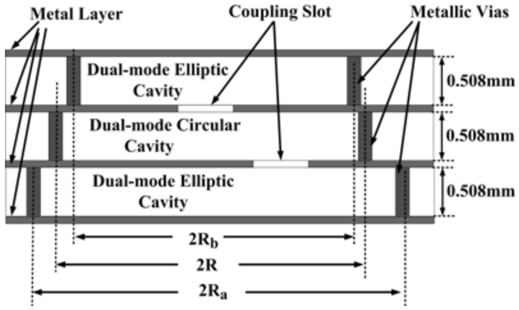

(c) Side view

Fig. 1. Proposed dual-mode SICC and SIEC filter with three layers.

B. Dual-mode SICC and SIEC principle

It is well known that the dual-mode phenomenon exists in a SICC and SIEC. Compared with the traditional rectangular cavity, the SICC and SIEC both are more suitable to be used as dual-mode cavities due to smooth inner surfaces. In a SICC, the degenerate modes are the horizontal and vertical TM_{110} mode. The resonant frequency for the circular cavity with solid wall can be calculated using [13]

$$f_{mnp} = \begin{cases} \dfrac{c}{2\pi\sqrt{\mu_r\varepsilon_r}}\sqrt{\left(\dfrac{\mu'_{mn}}{R}\right)^2+\left(\dfrac{p\pi}{\Delta h}\right)^2} & TE_{mnp} \\ \dfrac{c}{2\pi\sqrt{\mu_r\varepsilon_r}}\sqrt{\left(\dfrac{\mu_{mn}}{R}\right)^2+\left(\dfrac{p\pi}{\Delta h}\right)^2} & TM_{mnp} \end{cases}, \quad (1)$$

where μ_r and ε_r are relative permeability and permittivity of the filling material, respectively, μ_{mn} and μ'_{mn} are the n^{th} roots of the m^{th} Bessel function of the first kind and its derivative. The symbol R is the radius of the circular cavity, Δh is the height of the circular cavity, and c is the speed of light in free space. For $m > 0$, each m represents a pair of degenerate TM and TE modes (cos ($m\varphi$) or sin ($m\varphi$) variation). In circular cavity, TM_{110}, the second order mode, is selected as the working mode. Different directions represent different TM_{110} modes (cos ($m\varphi$) and sin ($m\varphi$) variation). μ_{mn} is 3.832 for the TM_{110} mode. Therefore, the corresponding resonant frequency of TM_{110} mode is,

$$f_{110} = \frac{c}{2\pi\sqrt{\mu_r\varepsilon_r}}\cdot\frac{3.832}{R} = \frac{0.61c}{R\sqrt{\mu_r\varepsilon_r}}. \quad (2)$$

Then, the radius of the SICC can be obtained by,

$$R = \frac{0.61c}{f_{110}\sqrt{\mu_r\varepsilon_r}}. \quad (3)$$

However, in an SIEC, the two TM modes are not degenerated and have different resonant frequencies. They are denoted by TM_{cmnp} and TM_{smnp} modes, respectively. The resonant frequency for elliptic cavity with solid wall can be calculated using [6, 7],

$$f_{mnp} = \frac{c\cdot\sqrt{q_{mnp}}}{R_a\pi e\sqrt{\mu_r\varepsilon_r}} = \frac{c}{\pi\sqrt{\mu_r\varepsilon_r}}\cdot\frac{\sqrt{q_{mnp}}}{\sqrt{R_a^2-R_b^2}} \quad (4)$$

$$\begin{array}{ll} \mathrm{Ce}_m(\xi_o, q) = 0, & \text{for } TM_{cm} \text{ mode} \\ \mathrm{Se}_m(\xi_o, q) = 0, & \text{for } TM_{sm} \text{ mode} \\ \mathrm{Ce}_m'(\xi_o, q) = 0, & \text{for } TE_{cm} \text{ mode} \\ \mathrm{Se}_m'(\xi_o, q) = 0, & \text{for } TE_{sm} \text{ mode,} \end{array} \quad (5)$$

where R_a and e are the semi-major axis and ellipticity of the SIEC, cosh (ξ_o) = 1 / e. R_b is the semi-minor axis. The parameter q is related to the resonant frequency, and there are a series of q values satisfying equation (5). To avoid ambiguity, a third subscript n, corresponding to the n^{th} parametric root, is required in the mode designation, q_{mnp} is the n^{th} parametric zero of the modified Mathieu functions of the first kind of the order m or their derivatives. Because of Mathieu functions' complicated calculation process, it is not very convenient to compute the parameters of a dual mode SIEC from equation (4). Accordingly, the corresponding resonant frequency of quasi TM_{110} also can be computed by following approximate formula,

$$f_{c110} = \frac{c}{2\pi\sqrt{\mu_r\varepsilon_r}}\cdot\frac{1}{R_a}\cdot\sqrt{\frac{120(2e^4-15e^2+28)}{17e^4-114e^2+198}}. \quad (6)$$

The resonant frequencies between the simulated results and the one obtained from equation (6) are compared as illustrated in Table 1. Since of a good agreement between the simulated and calculated results, it is concluded that the approximate formula can be used to determine the initial parameters of a dual-mode SIEC. Next, the solid wall is replaced by metallic vias to form SICC and SIEC under the guideline of [4, 5, 14]. The resonant frequencies of TM_{c110} and TM_{s110} modes are approximately equal for the smaller ellipticity e. Consequently, using equations (3) and (6) the initial dimensions of the cavities are determined for a desired resonant frequency.

Figure 2 shows the electrical fields of the TM_{110} and quasi TM_{110} modes within the SICC and SIEC, respectively. Obviously, they are two orthogonal modes, which co-exist in the same cavity. The fields of the modes are distributed in different directions (cos (φ) or sin (φ) variation). The two degenerate modes in the SICC can be easily excited by setting the angle α between 100 and 130 degrees. Besides, the TM_{c110} and TM_{s110} modes within the SIEC contribute to TZs located at lower sideband and are engaged in passband forming.

C. Coupling slot

As shown in Fig. 3, two poles and four TZs are found in the response of a dual-mode complementary filter. Two poles below the zero Z_{1up} are denoted as P_1 and P_2, respectively. The first and second zeros near the passband are denoted as Z_{1d} and Z_{1up}, respectively. Being so close to the passband, zeros Z_{1d} and Z_{1up} are both helpful to realize a steeper side response. The coupling slot size determines the position of the first zero and then sets the slope of the side response. Figures 4 and 5 illustrate variations of poles, zeros as the coupling slot sizes changed. The distance between the zero Z_{1d} and pole P_1 is decreased as the coupling slot size W_{S} or θ increased, but the frequency of P_1,

Z_{2up} is decreased evidently. Meanwhile, a change occurs in the frequency of P_2 and Z_{1up}.

Table 1: Resonance frequencies obtained from the simulation and equation (6).

	R_a, R_b (mm)	Simulation (GHz)	Calculated (GHz)	Error (%)
1	6, 5.21	22.101	22.216	+0.52
2	8, 6.96	15.513	15.475	-0.25
3	10, 8.045	13.485	13.362	-0.91
4	12, 9.756	11.156	11.131	-0.23
5	13.4, 10.6	9.936	9.976	+0.40
6	16, 12.87	8.366	8.351	-0.18

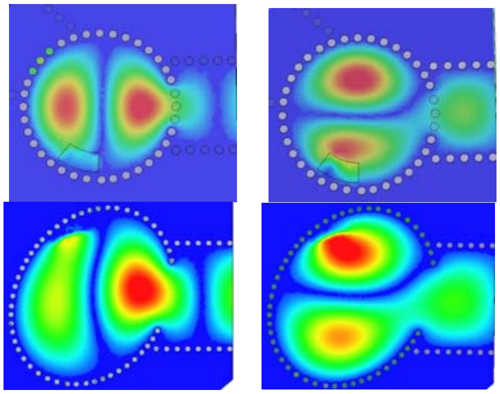

(a) Vertical mode (b) Horizontal mode

Fig. 2. The E-field distributions of the degenerate TM_{110} and quasi TM_{110} modes in SICC and SIEC.

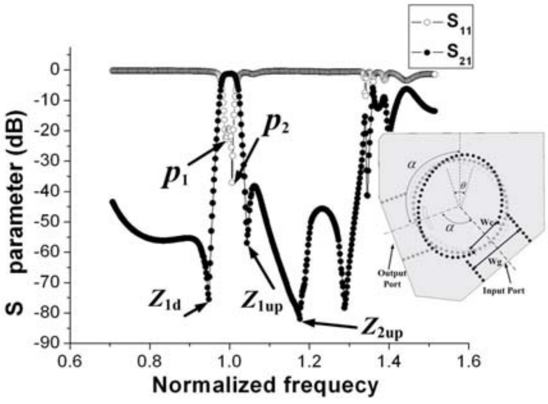

Fig. 3. Response of dual-mode complementary filter with SICC and SIEC.

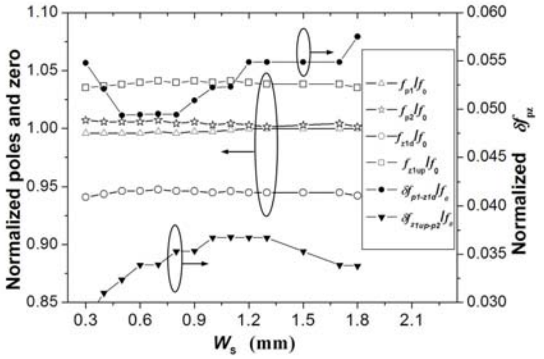

Fig. 4. Variation of poles, zeros with W_S, where, $\delta f_{p1\text{-}z1d} = f_{p1} - f_{p2}$, $\delta f_{z1up\text{-}P2} = f_{z1up} - f_{p2}$, $\theta = 36^o$, f_0 is the Eigen frequency of TM_{110} mode.

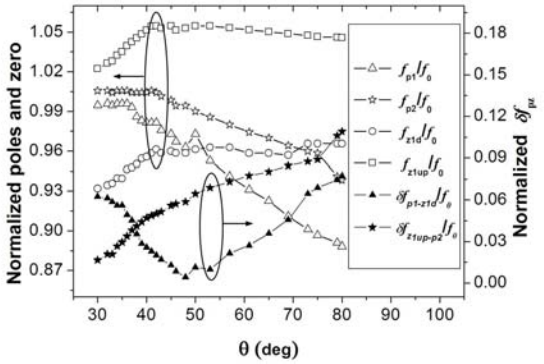

Fig. 5. Variation of poles, zeros with θ, where, $Ws = 0.6$ mm, $\delta f_{p1\text{-}z1d} = f_{p1} - f_{p2}$, $\delta f_{z1up\text{-}P2} = f_{z1up} - f_{p2}$.

As shown in Table 2, the coupling is increased when the slot size is increased. Then, it is possible to control the bandwidth and the rejection level. When the slot size is changed, the positions of P_1, P_2, Z_{1d}, and Z_{1up} influence the operating frequency. As observed in Figs. 4 and 5, the distance between the zero Z_{1d} and pole P_1 decreases evidently with the width of coupling slots W_S or θ decreases.

As observed in Table 3, the angle α also affects the bandwidth of the filter. A large value of α should be chosen for a broadband filter, while a small α may be proper for a narrowband filter. The proper value of α is between 100 and 130 degrees. Besides, the ellipticity e determines the position of the first zero Z_{1d}. As illustrated in Table 4, the ellipticity e is also an important factor affecting the bandwidth. So, a large value of e should be chosen for a broadband filter and vice versa.

Table 2: Relative bandwidth change with θ and W_s.

θ(deg)	$\Delta f/f_0$ (%)	W_s(*mm*)	$\Delta f/f_0$ (%)
30	3.3	0.3	3.10
35	3.6	0.4	3.50
38	4.1	0.6	3.95
40	4.39	0.7	4.10
60	4.5	0.8	4.15

Table 3: $\Delta f/f_0$ change with α.

W_c/R	α (deg)	$\Delta f/f_0$ (%)
0.785	110	3.9
0.785	120	4.1
0.785	130	4.2

Table 4: Relative bandwidth change with *e*.

e	W_c/R	α (deg)	$\Delta f/f_0$ (%)
0.569	0.81	110	2.77
0.587	0.81	110	3.61
0.592	0.81	110	3.85
0.612	0.81	110	4.06
0.646	0.81	110	4.20

D. External feeding structure

The filter is excited by a tapered microstrip lines. Energy travels from the microstrip line into the SIEC resonators and then is magnetically coupled into the adjacent SICC by means of coupling slots.

Moreover, the bandwidth and rolloff slope in the transition band are affected by W_c/R for a given angle α, as shown in Table 5. In general, smaller W_c/R leads to narrower bandwidth and steeper rolloff slope in the transition band.

Table 5: $\Delta f/f_0$ change with W_c/R.

W_c/R	α (deg)	$\Delta f/f_0$ (%)	W_c/R	α (deg)	$\Delta f/f_0$ (%)
0.72	110	3.60	0.79	130	4.3
0.78	110	3.87	0.88	130	4.5
0.87	110	4.10	0.96	130	4.8

E. Design consideration

As shown in Fig. 6, a SICC and SIEC techniques can be employed together to achieve multilayer filter. Nevertheless, its selectivity is lower, and absence of geometric symmetry makes more difficulties in adjustment. So, to achieve higher selectivity, symmetrical structures are proposed as the input/output ports, i.e., double SIECs combined with a SICC.

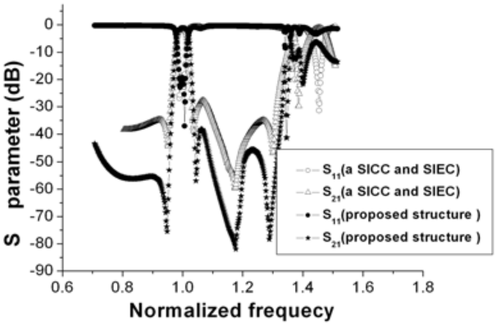

Fig. 6. Responses of multilayer dual-mode filters.

F. Design example

In our design, the center frequency and bandwidth of the filter are 10 GHz and 400 MHz, respectively. The used substrate is Rogers 5880 with relative permittivity (ε_r) of 2.2 and height of 0.508 mm. Here, the SICC and SIEC operate at TM_{110} and quasi TM_{110} modes, respectively. In the present design, the first step is to decide the dimensions of SICC and SIEC cavities. By using equations (2) and (3), the initial values of radius of SICC cavities (*R*) should be 12.3 mm. According to equation (6) and Table 4, the semi-major (R_a) and semi-minor (R_b) axes of the SIEC should be 13.3 mm and 10.7 mm, respectively.

The second step is to calculate the coupling coefficients and external quality factor. The coupling scheme of the proposed dual-mode complementary filter is presented in Fig. 7. Resonators 1, 2 and resonators 3, 4 represent two orthogonal modes, respectively. From the above discussion, the initial geometrical parameters of slot and cavities will be determined as follow:

i) Based on the above discussion, the angle α is the key factor to realize the dual-mode character in multilayer SICCs and SIECs. As shown in Fig.1, the angle between the coupling slot 1 and input port is set to α in order to realize dual-mode in cavity 1. And then, the angle between the coupling slots 1 and 2 is also equal to α so that degenerate modes can exist in cavity 2. Similarly, the angle between the coupling slot 2 and output port must be kept as α in cavity 3. Based on the specification, the proper value of α is 110°.

ii) The coupling slot size determines the bandwidth and the positions of the zeros. According to Figs. 4, 5 and Table 2, the initial geometrical parameters of the slot are determined. One can choose the width of the coupling slot with $W_S = 0.6$ mm, the central angle $\theta = 38^o$.

iii) The bandwidth and rolloff slope in the transition band are affected by W_c/R. As shown in Table 5, the widths of the coupling apertures are determined as $W_c/R = 0.8$. For a given angle $\alpha = 110^o$, the proper parameters are limited in a relatively narrow interval. According to Table 5 and the specifications, the value ranges for W_c/R are from 0.75 to 0.85. Similarly, as observed in Table 2, the value ranges for W_S, θ are from 0.6 to 0.8 and from 35^o to 39^o, respectively. According to the above considerations, the final optimal dimensions of the proposed filter can be easily determined.

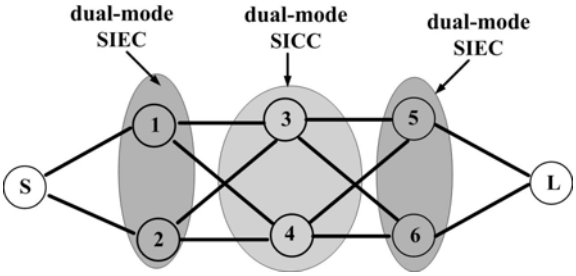

Fig. 7. Coupling scheme of the sixth-order dual-mode filter (gray areas show dual-mode cavities).

III. EXPERIMENT RESULTS

Based on the above-discussed theories, the multilayer dual-mode complementary filter is designed and fabricated with PCB process. Figure 8 is the photograph of the fabricated dual-mode filter. After optimization being implemented by Ansoft HFSS, the geometry parameters of the proposed filter are listed in Table 6. The metallic via diameter is 0.8 mm. The space between two adjacent vias is uniformly arranged around 1.5 mm.

Table 6: Parameters of the fabricated filter.

*D*via(mm)	0.8	*W*strip(mm)	1.58
p(mm)	1.5	*W*g (mm)	16
ε_r	2.2	*W*c (mm)	10.5
*W*s(mm)	0.7	*h*(mm)	0.508
α(deg)	110	*R*(mm)	12.2
θ(deg)	37	R_a(mm)	13.6
R_b(mm)	10.7		

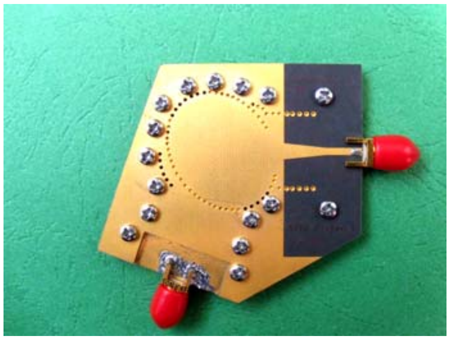

Fig. 8. Photograph of the fabricated filter.

As observed from Fig. 9, the fabricated filter has a center frequency of 9.95 GHz with a bandwidth of 397.6 MHz. The maximum return loss of the proposed filter is 19.5 dB and the insertion loss is about 2.35 dB. Three finite transmission zeros are located at 9.4, 10.3, and 11 GHz, respectively. Its stop band is from 7.8 GHz to 9.45 GHz with the rejection more than 50 dB, and from 10.8 GHz to 12.9 GHz with the rejection more than 45 dB. Table 7 gives some reported performance of SIW filters in recent years for comparison purposes and it demonstrates that this work has realized miniaturization and improved selectivity.

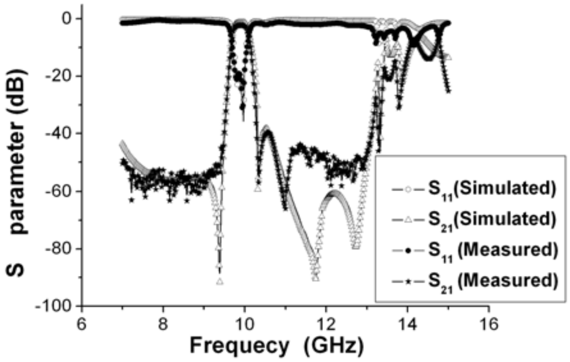

Fig. 9. Simulated and measured results of the dual-mode complementary filter with three layers.

IV. CONCLUSION

A novel multilayer dual-mode complementary filter has been designed, fabricated, and measured in this paper. The complementary SICC and SIEC are introduced in the 3-D multilayer SIW circuits, and a compact dual-mode filter with low loss and elliptic response has been achieved. The bandwidth and restraint outside the band can be controlled by adjusting the parameters of the coupling aperture and arc-shaped slot. The measured maximum return loss is 19.5 dB over the passband while the insertion loss is about 2.35 dB. In particular, measured results show that the stopband rejection of the filter is better than 50 dB. Good agreement is obtained between the simulated and measured results of the proposed structure. This structure is very compact and well suited for the microwave and millimeter wave applications.

Table 7: Performance comparison of the SIW filters.

Ref.	Size (λ_g^2)/ Number of layers and TZs	f_0 (GHz)	Stopband rejection / IL(dB)
[4]	6.80/1/1	14.60	30/3.5
[5]	4.80/2/2	20	16/2.2
[8]	6.36/1/1	25.53	30/2.5
[9]	5.29/4/2	30	25/2.95
This work	4.10/3/4	9.95	50/2.35
Where λ_g is the guided wavelength on the substrate at the center frequency f_0.			

ACKNOWLEDGMENT

This work is supported in part by the National Natural Science Foundation of China (NSFC) under grant 61001028 and in part by Research Fund for the Doctoral Program of Higher Education of China (RFDP) under grant 20100185110001，and in part by the Fundamental Research Funds for the Central Universities under grant ZYGX2010J019.

REFERENCES

[1] X. P. Chen and K. Wu, "Substrate integrated waveguide filter with improved stopband performance for satellite ground terminal," *IEEE Trans. Microw. Theory Tech.*, vol. 57, no. 3, pp. 674-683, March 2009.

[2] W. Shen, W. Y. Yin, and X. W. Sun, "Compact substrate integrated waveguide (SIW) filter with defected ground structure," *IEEE Microw. Wirel. Compon. Lett.*, vol. 21, no. 2, pp. 83-85, Feb. 2011.

[3] D. Deslandes and K. Wu, "Substrate integrated waveguide dual-mode filters for broadband wireless systems," *RAWCON '03. Proceedings*, pp. 385-388, Aug. 2003.

[4] B. Potelon, J. F. Favennec, E. Rius, and J. C. Bohorquez, "Design of a substrate integrated waveguide (SIW) filter using a novel topology of coupling," *IEEE Microw. Wirel. Compon. Lett.*, vol. 18, no. 9, pp.596-598, Sep. 2008.

[5] Q. -F. Wei, Z. -F. Li, and L. -S. Wu, "Compact cross-coupled circular cavity filters using multilayer substrate integrated waveguide," *Electron. Lett.* vol. 45, no. 6, 12th March 2009.

[6] S. J. Zhang and Y. C. Shen, "Eigenmode sequence for an elliptical waveguide with arbitrary ellipticity," *IEEE Trans. Microw. Theory Tech.*, vol. 43, no. 1, pp. 227-230, Jan. 1995.

[7] L. Accatino, G. Bertin, and M. Mongiardo, "Elliptical cavity resonators for dual-mode narrow-band filters," *IEEE Trans. Microw. Theory Tech.*, vol. 45, no. 12, pp. 2393-2401, Dec. 1997.

[8] H. J. Tang, W. Hong, J. -X. Chen, G. -Q. Luo, and K. Wu, "Development of millimeter-wave planar diplexers based on complementary characters of dual-mode substrate integrated waveguide filters with circular and elliptic cavities," *IEEE Trans. Microw. Theory Tech.*, vol. 55, no. 4, pp.776-781, April 2007.

[9] K. Ahn and I. Yom, "A ka-band multilayer LTCC 4-pole bandpass filter using dual-mode cavity resonators," *Microwave Symposium Digest, 2008 IEEE MTT-S International*, pp.1235-1238, June 2008.

[10] R. Rezaiesarlak, M. Salehi, and E. Mehrshahi, "Hybrid of moment method and mode matching technique for full-wave analysis of SIW circuits," *Appl. Comp. Electro. Society (ACES) Journal*, vol. 26, no. 8, pp. 688-695, August 2011.

[11] W. Shao and J. L. Li, "Design of a half-mode SIW high-pass filter," *Appl. Comp. Electro. Society (ACES) Journal*, vol. 26, no. 5, pp. 447-451, May 2011.

[12] R. Q. Li, X. H. Tang, and F. Xiao, "Substrate integrated waveguide dual-mode filter using slot lines perturbation," *Electron. Lett.*, vol. 46, no. 12, 10th June 2010.

[13] D. M. Pozar, *Microwave Engineering,* 2nd Edition, Wiley, New York, 1998.

[14] F. Xu and K. Wu, "Guided-wave and leakage characteristics of substrate integrated waveguide," *IEEE Microw. Theory Tech.*, vol. 53, no. 1, pp. 66-70, Jan. 2005.

Zhigang Zhang was born in Shanxi Province, China. He received the B.Sc. degree in Electronic Information Engineering and M.Sc. degree in wireless physics from Sichuan University and is currently working toward the Ph.D. degree in electromagnetic field and microwave technology from The University of Electronic Science and Technology of China (UESTC), Chengdu, Sichuan, China. His current research interests include SIW technology and its application, microwave and millimeter-wave filters and couplers, electromagnetic theory.

Yong Fan received the B.E. degree from the Nanjing University of Science and Technology, Nanjing, Jiangsu, China, in 1985, and the M.Sc. degree from the University of Electronic Science and Technology of China (UESTC), Chengdu, Sichuan, China, in 1992. He is currently with the School of Electronic Engineering, UESTC. He has authored or coauthored over 60 papers. From 1985 to 1989, he was interested in microwave integrated circuits. Since 1989, his research interests include millimeter-wave communication, electromagnetic theory, millimeter-wave technology, and millimeter-wave systems. Mr. Fan is a Senior Member of the Chinese Institute of Electronics (CIE).

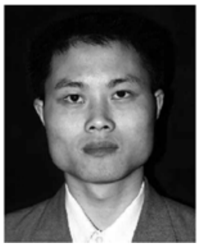

Yonghong Zhang received the B.Sc., M.Sc., and Ph.D. degrees from the University of Electronic Science and Technology of China (UESTC), Chengdu, China, in 1992, 1995, and 2001, respectively. From 1995 to 2002, he was a Teacher with the UESTC. In 2002, he joined the Electronic Engineering Department, Tsinghua University, Beijing, China, as a Doctoral Fellow. In 2004, he rejoined the UESTC. His research interests are in the area of microwave and millimeter-wave technology and applications.

Small Microstrip Low-Pass Filter by using Novel Defected Ground Structure for UWB Applications

Ahmad Faraghi [1], Mohammad-Naghi Azarmanesh [1], and Mohammad Ojaroudi [2]

[1] Microelectronic Research Laboratory
Urmia University, Urmia, Iran
st_a.faraghi@urmia.ac.ir and m.azaramanesh@urmia.ac.ir

[2] Young Researchers Club
Ardabil Branch, Islamic Azad University, Ardabil, Iran
m.ojaroudi@iauardabil.ac.ir

Abstract **─** In this paper, a novel low-pass filter using defected ground structure (DGS) slot with a protruded T-shaped strip inside the slot is presented. The resonant frequency of the slot can be easily controlled by changing the protruded T-shaped strips dimensions, without changing the area taken by the structure. Using this DGS slot, a quasi-elliptic low-pass filter was designed, fabricated, and tested. The experimental results show good agreement with simulation results and demonstrate that excellent stop-band performance could be obtained through the proposed low-pass filter. The filter has a cut-off frequency of about 3.4 GHz.

Index Terms **─**Defected ground structure, microstrip low-pass filter, protruded T-shaped strip, and T-shaped open stub.

I. INTRODUCTION

Conventionally, the microwave low-pass filter (LPF) is implemented either by all shunt stubs or by series connected high-low stepped-impedance microstrip line sections. However, generally these are not easily available in microwave band due to the high impedance microstrip line and the spurious pass-bands. To remove these disadvantages, defected ground structures for microstrip lines have been presented in recent years. They have been presented in a number of different shapes for filter applications [1-5]. Some of the DGS techniques that are used to design these kinds of filters with broad bandwidth include the following: embedding two complementary split ring resonators (CSRR) in the ground plane [2], embedding multilayer coupled resonator DGS [3], using a novel quarter-circle DGS shape [4], utilizing the octagonal defected ground structure (DGS) along with inter-digital and compensated capacitors [5]. This technique is suitable for periodic structures and for both low-pass and band-pass filters, e.g., [6-8]. The DGS applied to a microstrip line causes a resonant characteristic of the structure transmission with a resonant frequency controllable by changing the shape and size of the slot.

This paper introduces a DGS with folded T shaped arms. The resonant frequency of the structure with this slot can be controlled by adjusting the distance between the T-shaped arms without changing the area occupied by the slot or the aperture. A quasi-elliptic low-pass filter based on this slot was designed and fabricated on a Rogers RT/Duroid 5880 substrate with 0.635 mm thickness and with a relative dielectric constant of 2.2. The resonant behavior of the DGS used here introduces transmission zeroes to the filter response and consequently improves its stop-band performance.

II. FILTER DESIGN AND CONFIGURATION

The proposed microstrip filter configuration with apertures under the high-impedance transmission lines is shown in Fig. 1.

Submitted On: June 22, 2012
Accepted On: Feb. 6, 2013

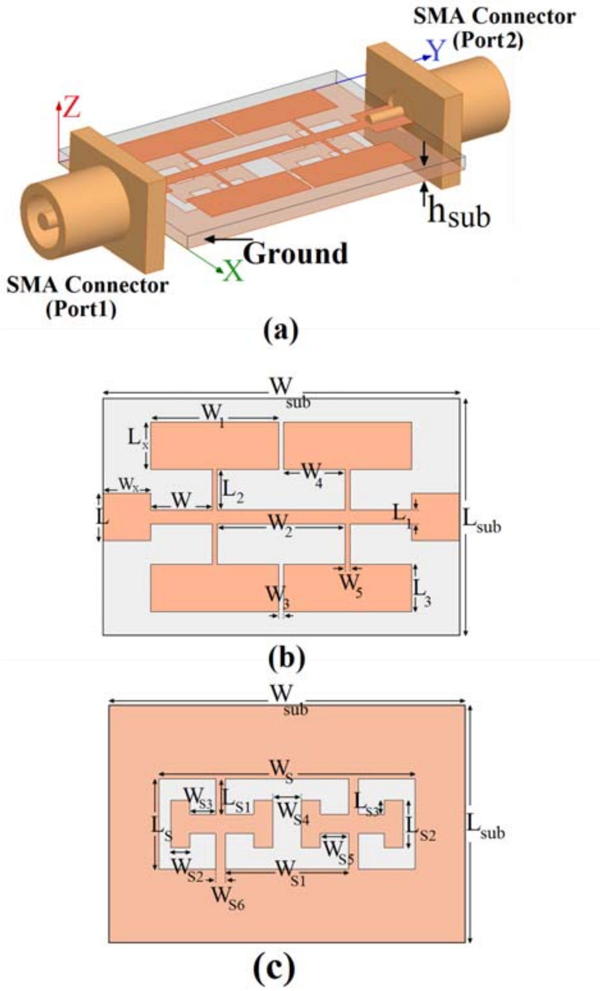

Fig. 1. Geometry of proposed microstrip filter, (a) side view, (b) top view, and (c) bottom view.

In general, the cut-off frequency of the microwave low-pass filter (LPF) can be adjusted by setting proper values of the lumped elements of the filter [9]. In addition, to realize the desired capacitive and inductive values of the filter elements by the stubs of the high/low impedance transmission lines, the characteristic impedance and effective dielectric constant of these transmission lines have to be determined. The low-pass filter shown in Fig. 1 was designed on a Rogers RT/Duroid 5880 substrate with 0.635 mm thickness and relative dielectric constant of 2.2.

Defected ground structure (DGS) evolved from photonic band gap (PBG); it is realized by etching defected pattern and slot in the ground plane. The etched defect in ground plane disturbs the shield current distribution in the ground plane. This disturbance can increase the effective capacitance and inductance of a transmission line, respectively. Thus, an LC equivalent circuit can represent the proposed unit DGS circuit [1-3]. The proposed DGS slot is shown in Fig. 1 (c). The slot is etched in the ground metallization under the microstrip line. This slot has a major advantage in providing tighter capacitive coupling to the line in comparison to known microstrip DGS. Moreover, the resonant frequency of the structure can be controlled by changing the distance between the folded T-shaped arms. The resonant frequency of the slot can be modified by changing the overall slot size, which shifts the cut-off frequency of the filter down. To shift the frequency up instead of frequency back, it is necessary to reduce the inductance of the narrow strip line that is located over the slot. This can easily be done by increasing the width of the strip [10, 11].

The final dimensions of the proposed low-pass filter are specified in Table 1.

Table 1: The final dimensions of the designed filter.

Param.	mm	Param.	mm	Param.	mm
W_{Sub}	15	L_{Sub}	10	W_S	10.8
L_S	3.8	W_{S1}	5.2	L_{S1}	1.5
W_{S2}	0.8	L_{S2}	2	W_{S3}	1.1
L_{S3}	0.6	W_{S4}	1.2	W_{S5}	1.2
W_{S6}	0.4	L	2	L_1	0.6
W_1	5.4	L_2	1.7	W_2	4.4
L_3	2	W_3	0.2	W_4	2.6
W_5	0.2	L_X	2	W_X	2

III. RESULTS AND DISCUSSIONS

The microstrip low-pass filter shown in Fig. 1 was designed on both substrate sides by opening apertures in the ground metallization under the high-impedance transmission line. Replacing some of the apertures by the proposed folded T-shaped arms structure introduces transmission zeroes. The number of transmission zeroes is equal to the number of apertures with folded T-shaped arms. One transmission zero is introduced into the filter response by replacing the central aperture by the proposed folded T-shaped arms structure. This slot, however, shifts the cut-off frequency of the filter down. To shift the cut-off frequency back, it is necessary to reduce the inductance of the narrow strip line that is located over the slot [10]. For the input/output connections 50 Ω microstrip lines are used. The parameters of this proposed filter structure are studied by changing one parameter at a time while others are kept fixed. The simulated results are obtained using the Ansoft simulation software high-frequency structure simulator (HFSS) [12].

To minimize the physical size of the proposed low-pass filter and increase its bandwidth, four T-shaped open stubs are introduced into the microstrip transmission line to alter the input impedance characteristics. Figure 2 shows the structure of the various filter used for simulation studies. Return/insertion loss characteristics for ordinary microstrip transmission line (Fig. 2 (a)), with four rectangular open stubs (Fig. 2 (b)), and with four T-shaped open stubs (Fig. 2(c), which is the proposed structure) are all compared in Figs. 3 (a) and (b). From the results shown in Fig. 3 (a), it is observed that when four T-shaped open stubs are used, the return loss of the proposed filter is changed at lower frequencies. As shown in Fig. 3 (b), the four T-shaped open stubs also influence the bandwidth of the insertion loss [13]. The proposed transmission line structure can be used to extend the lower edge frequency and the upper edge frequency of the insertion loss bandwidth.

Another important parameter of this structure is the exterior length of the T-shaped open stubs L_X. Figure 4 shows the return loss for different values of L_X. It is seen that the lower-edge frequency of the return loss bandwidth is reduced with increasing L_X, but the matching became poor for larger values. Therefore, it can be realized that the optimized L_X is 2 mm.

In this paper, in order to increase the insertion loss bandwidth, two novel C-shaped slots and a rectangular slot with protruded T-shaped strips inside the slots are inserted in the ground plane of the proposed design as shown in Fig. 1. As illustrated in Fig. 5, the microstrip filter with slotted ground plane has wider insertion loss bandwidth in comparison to the same filter without slots in the ground plane [14, 15].

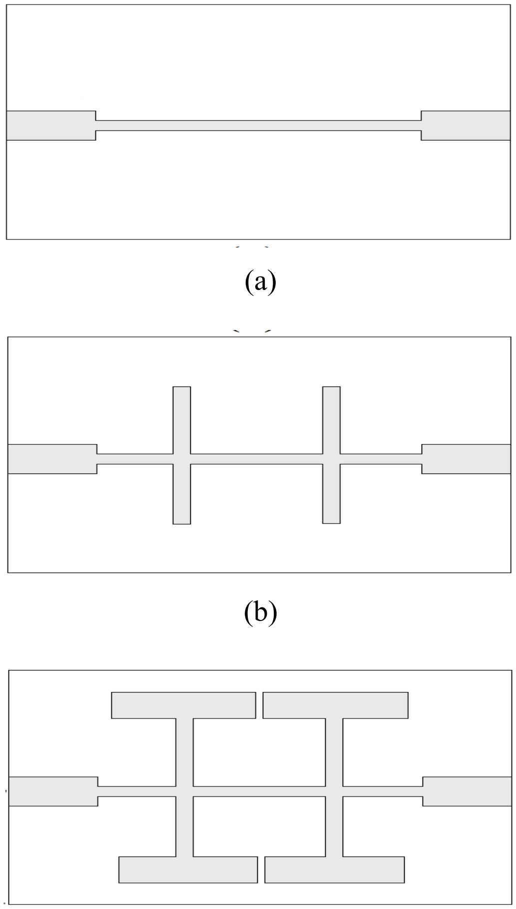

(a)

(b)

(c)

Fig. 2. (a) Ordinary microstrip transmission line (b) with four rectangular open stubs, and (c) with four T-shaped open stubs (the proposed structure).

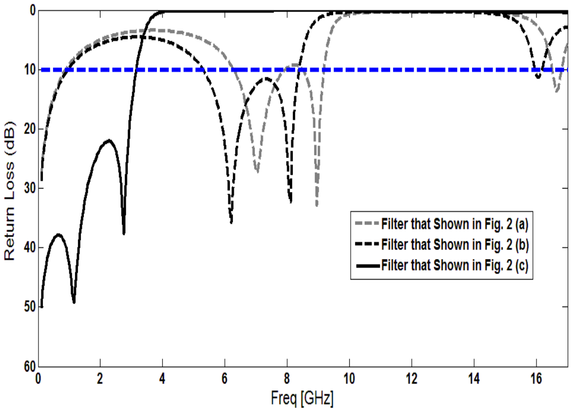

(a)

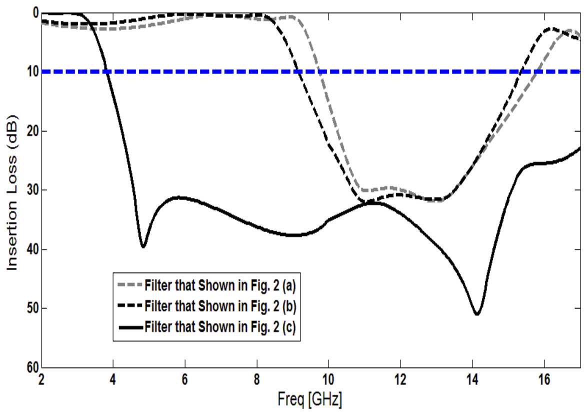

(b)

Fig. 3. Simulated return/insertion loss characteristics for the various filter structures shown in Fig. 2, (a) return loss and (b) insertion loss.

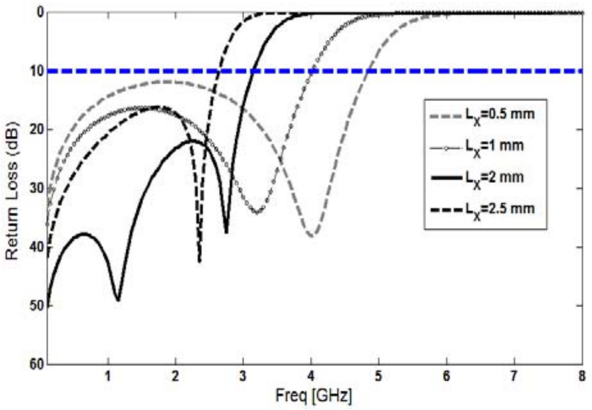

Fig. 4. Simulated return loss characteristics for various values of L_X.

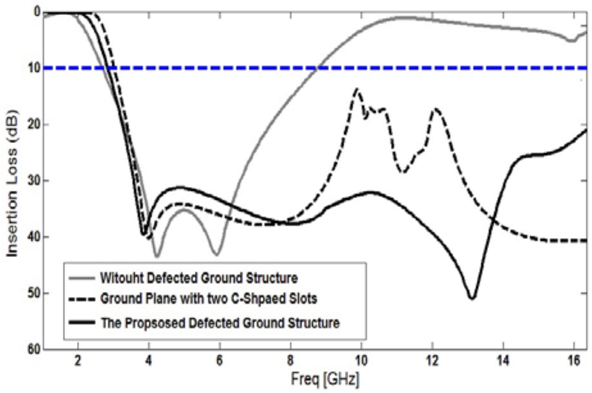

Fig. 5. Simulated insertion loss characteristics for the proposed filter with and without the proposed slots in the ground plane.

By inserting four modified T-shaped strips of suitable dimensions at the corners of ground plane slots, a new configuration can be constructed. The truncated ground plane is playing an important role in the broadband characteristics of this filter, as it helps matching of the transmission line in a wide range of frequencies. This is because the truncation creates a capacitive load that neutralizes the inductive nature of the patch to produce nearly-pure resistive input impedance [16, 17]. Three such slots with different sizes of T-shaped strips are specified in Table 2 as cases 1, 2, and 3.

Table 2: Three cases of the proposed filter with different values of T-shaped strips.

Case	W_{S2}	L_{S2}	W_{S3}	L_{S3}
1	0.5	2.3	0.7	0.9
2	0.8	2	1.1	0.6
3	1	1.8	1.4	0.45

Figure 6 shows the effect of T-shaped strips with different values on the insertion matching in comparison with the same filter without T-shaped strips. It is found that by inserting the four T-shaped strip of suitable dimensions at the ground plane additional transmission zero at 14 GHz is created and hence, much wider insertion loss bandwidth with multi transmission zeros can be produced, especially at the higher band.

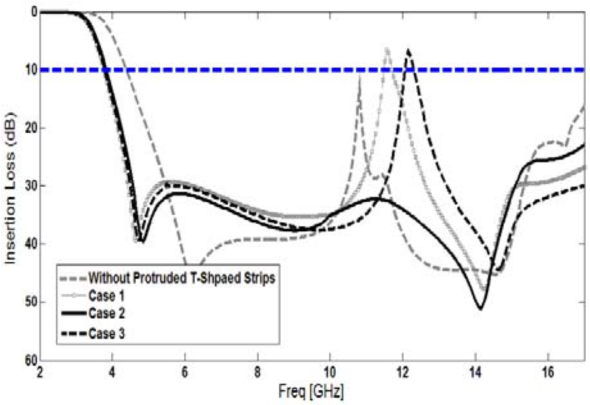

Fig. 6. Simulated insertion loss characteristics for the proposed filter without T-shaped strip and three cases 1, 2, and 3 with strips as shown in Table 2.

Table 3: Comparison of the proposed DGS-LPF with other related LPFs.

Reference	*Dimension (mm^2)*	*Return Loss (S_{11}<-20 dB)*	*Insertion Loss (S_{21}<-20 dB)*	*Cut-Off Frequency*	*Number of Transmission Zeros*
Ref [3]	30×30	1-1.85	3-4.93	2.2 GHz	2
Ref [4]	27×21	0-2.52	3.3-5.43	3.04 GHz	2
Ref [5]	25×14	0-2.5	5-20	2.95 GHz	3
Ref [6]	40×20	0-2.8	3.7-7.5	3.2 GHz	1
This Work	15×10	0-3.15	3.87-17.3	3.4 GHz	3

In Table 3 the performance of the proposed low-pass filter (designed based on the ideas, which are presented in previous sections) has been compared with prototypes in [3-6]. It can be seen from Table 3 that the proposed filter provides good performance in stop-band rejection and pass-band return loss and smaller in size than those reported in literature. The proposed filter with optimal design, as shown in Fig. 7, was fabricated and tested in the Antenna Measurement Laboratory at Iran Urmia University. Figure 8 shows the simulated and measured insertion and return loss of the filter. As shown in Fig. 8, two transmission zeros are introduced to the filter response at about 5.02 GHz and 14.12 GHz. Consequently, a wide stop-band was achieved. Additionally, the proposed DGS low-pass filter also has characteristics of wider and deeper stop-band than those of conventional low-pass filters.

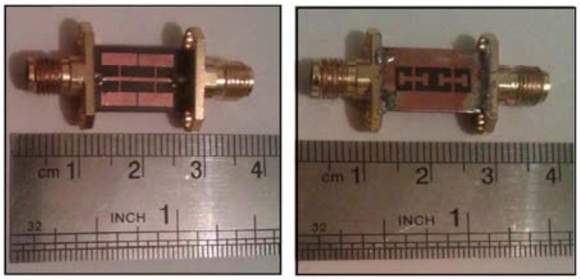

(a) (b)

Fig. 7. Photograph of the realized printed low pass filter (a) top view and (b) bottom view.

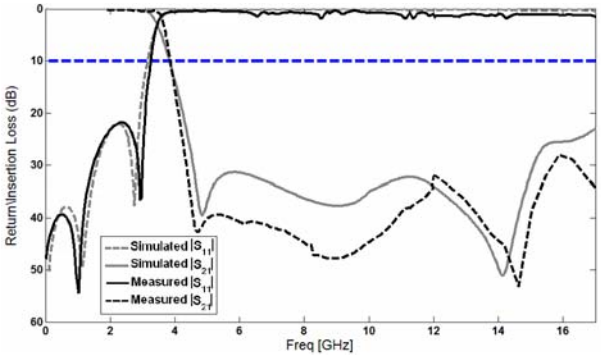

Fig. 8. Measured and simulated return/insertion losses for the proposed low pass filter.

IV. CONCLUSION

In this paper, two compact quasi-elliptic low-pass filters using novel DGS slot with folded T-shaped arms are designed and fabricated. The main advantages of the proposed DGS are its compact size and the fact that the parallel resonant frequency can be controlled without changing the overall slot area of the DGS. The transmission zeros introduced to the filter responses improves their stop-band behavior. Simulation results using 3-D HFSS shows good consistency with experimental results. It is also of potential to be used in microwave and millimeter wave ICs.

ACKNOWLEDGMENT

The authors are thankful to Microwave Technology (MWT) Company staff for their beneficial and professional help (www.microwave-technology.com).

REFERENCES

[1] C. -S. Lim, C. -S. Kim, D. Ahn, Y. -C. Jeong, and S. Nam, “Design of the low-pass filters using defected ground structure,” *IEEE Trans. Microw. Theory Tech.*, vol. 53, no. 8, pp. 2539-2545, Aug. 2005.

[2] S. U. Rehman, A. A. Sheta, and M. A. S. Alkanhal, "Compact bandpass filters with bandwidth control using defected ground structure (DGS)," *Appl. Comp. Electro. Society (ACES) Journal*, vol. 26, no. 7, pp. 624-630, July 2011.

[3] G. E. Al-Omair, S. F. Mahmoud and A. S. Al-Zayed, "Lowpass and bandpass filter designs based on DGS with complementary split ring resonators," *Appl. Comp. Electro. Society (ACES) Journal*, vol. 26, no. 11, pp. 907-914, Nov. 2011.

[4] M. Challal, A. Boutejdar, M. Dehmas, A. Azrar, and A. Omar, "Compact microstrip low-pass filter design with ultra-wide reject band using a novel quarter-circle DGS shape," *Appl. Comp. Electro. Society (ACES) Journal*, vol. 27, no. 10, pp. 808-815, Oct. 2012.

[5] A. Boutejdar, M. Challal, and A. Azrar, "A novel band-stop filter using octagonal-shaped patterned ground structures along with interdigital and compensated capacitors," *Appl. Comp. Electro. Society (ACES) Journal*, vol. 26, no. 4, pp. 312-318, April 2011.

[6] W. Shao and J. L. Li, "Accurate modeling of a patterned ground and its application to microwave filters," *Appl. Comp. Electro. Society (ACES) Journal*, vol. 27, no. 7, pp. 596-602, July 2012.

[7] R. Habibi, Ch. Ghobadi, J. Nourinia, M. Ojaroudi, and N. Ojaroudi, "Very compact broad band-stop filter using periodic L-shaped stubs based on self-complementary structure for X-band application," *Electro. Letters IET*, vol. 48, no. 23, 8th Nov. 2012.

[8] J. S. Yun, G. Y. Kim, J. S. Park, D. Ahn, K. W. Kang, and J. B. Lim, "A design of the novel coupled line bandpass filter using defected ground structure," *IEEE MTT-S Int. Dig.*, Boston, MA, pp. 327-330, June 2000.

[9] J. S. Park, J. S. Yun, and D. Ahn, "A design of the novel coupled line bandpass filter using defected ground structure with wide stopband performance," *IEEE Trans. Microw. Theory Tech.*, vol. 50, no. 9, pp. 2037-2043, Sep. 2002.

[10] J. -S. Lim, C. –S. Kim, Y. –T. Lee, D. Ahn, and S. Nam, "Design of lowpass filters using defected ground structure and compensated microstrip line," *Electro. Letters IET*, vol. 38, no. 22, Oct. 2002.

[11] Ansoft High Frequency Structure Simulation (HFSS), Ver. 13, Ansoft Corporation, 2010.

[12] A. B. Abdel-Rahman, A. K. Verma, A. Boutejdar, and A. S. Omar, "Control of bandstop response of Hi-Lo microstrip low-pass filter using slot in ground plane," *IEEE Trans. Microw. Theory Tech.*, vol. 52, no. 3, pp. 1008-1013, Mar. 2004.

[13] H. -W. Liu, Z. -F. Li, W. Sun, and J. -F. Mao, "An improved 1-D periodic defected ground structure for microstrip line," *IEEE Microw. Wireless Compon. Lett.*, vol. 14, no. 4, pp. 180-182, Apr. 2004.

[14] C. -S. Kim, J. –S. Lim, J. -H. Kim, and D. Ahn, "A design of a miniaturized 2-pole bandpass filter by using slot and hair-pin line," *IEEE MTT-S Int. Dig.*, Fort Worth, TX, pp. 1983-1986, June 2006.

[15] A. R. Ali, A. Abdel-Rahman, A. Amari, and A. S. Omar, "Direct and cross-coupled resonator filters using defected ground structure (DGS) resonators," *Proc. 35th Eur. Microw. Conf.*, Paris, France, pp. 1275-1278, Oct. 2005.

[16] A. Abdel-Rahman, A. K. Verma, A. Boutejdar, and A. S. Omar, "Compact stub type microstrip bandpass filter using defected ground plane," *IEEE Microw. Wireless Compon. Lett.*, vol. 14, no. 4, pp. 136-138, Apr. 2004.

[17] S. -W. Ting, K. -W. Tam, and R. P. Martins, "Compact microstrip quasi-elliptic bandpass filter using open-loop dumbbell shaped defected ground structure," *IEEE MTT-S Int. Dig.*, San Francisco, CA, pp. 527-530, June 2006.

Ahmad Faraghi was born in 1982 in Bileh-Savar, Iran. He received his B.Sc. degree in Electrical Engineering from Islamic Azad University, Sarab Branch. Since 2010, he has been working toward the M.Sc. degree at Urmia University. Since 2010 until now, he has been a Teaching Assistant with the Department of Electrical Engineering, Islamic Azad University, Pars-Abad Branch. Since March 2011, he has been a Research Fellow in the Microwave Technology Company (MWT), Tehran, Iran. His research interests include microstrip filter, low-pass filters for ultra-wideband (UWB) applications and small filters for wireless communications, microwave passive devices and circuits, and microwave/millimeter systems.

Mohammad Naghi Azarmanesh, was born in Tabriz, Iran, in 1950. He received the B.Sc. degree in physics from Tabriz University, Iran, in 1973, the M.Sc. degree in Electrical Engineering from the University of Paris VI in 1976, and Ph.D. degree in Electrical Engineering from Polytechnique De Toulouse, France, in 1978. His doctoral dissertation concerned study of inverted strip dielectric waveguide for millimeter wave applications. In 1979 he joined Applied Physics Department in Urmia University, where he worked effectively in founding Electrical Engineering Department in 1983. In 1998 he worked with three other colleagues in developing Microelectronics Research Center in Urmia University. He is currently the head of Microelectronics Research Center. His main research interests are in the area of planar antenna, RF microelectronics and microwave filters. He is a member of Iranian Society of Electrical Engineers.

Mohammad Ojaroudi was born on 1984 in Germi, Iran. He received his B.Sc. degree in Electrical Engineering from Islamic Azad University, Ardabil Branch and M.Sc. degree in Telecommunication Engineering from Urmia University. Since 2010, he is working toward the Ph.D. degree at Shahid Beheshti University. Since 2007 until now, he has been a Teaching Assistant with the Department of Electrical Engineering, Ardabil Branch, Islamic Azad University, Iran. Since March 2009, he has been a Research Fellow (Chief Executive Officer) in the Microwave Technology Company (MWT), Tehran, Iran. His research interests include analysis and design of microstrip antennas, design and modeling of microwave structures, radar systems, and electromagnetic theory. He is author and coauthor of more than 100 journal and international conference papers. His papers have more than 300 citations with 10 h-index.

A Novel Dual-Band Microstrip Bandpass Filter Design and Harmonic Suppression

Xiuping Li[1, 2] and Junjie Zeng[1, 2]

[1] School of Electronic Engineering, Beijing University of Posts and Telecommunications,
Beijing, 100876, China

[2] State Key Laboratory of Millimeter Waves, Southeast University, Nanjing 210096, China
xpli@bupt.edu.cn, zjj070331@bupt.edu.cn

Abstract **─** This paper proposes a new dual-passband microstrip bandpass filter, which is composed of two asymmetric half-wavelength resonators and four shunt open stubs that provides four transmission zeros. Two short stubs are added to suppress the second harmonic. The relationship of the four transmission zeros and the dimensions of the filter are all provided. The dual-passband microstrip bandpass filter is fabricated with the first passband of 2.4 GHz corresponds to the bandwidth of 0.1 GHz and the second passband of 5.7 GHz corresponds to the bandwidth of 0.25 GHz. The insertion loss of the two passband is less than 1 dB and 3 dB, respectively and the return loss is more than 10 dB. The results of the measured and simulated data agree well.

Index Terms **─** Bandpass filter, dual-band, harmonic suppression, and transmission zeros.

I. INTRODUCTION

Recent development in wireless communication and radar systems has presented new challenges to design and produce high-quality miniature components with a dual-band operation. Therefore, as important component of wireless systems, the filter is required to have dual-band performance. To design the dual-band filter, the simplest way is combining two single-band filters at different passband frequencies [1-3]. But it requires an implementation area twice that of a single-band filter and additional external combining networks. Thus, an integrated filter with a dual-band response is more attractive. Step-impedance resonators (SIR) are utilized in [4-6] and the filters show high skirt selectivity. The method of defect ground structure and shunt open stubs technology are utilized wildly for filter size miniaturization and harmonic suppression [7]. In the filter design process, the shunt stubs are used to create transmission zeros in order to separate the passband and increase the stopband region [8-9].

This paper presents the new applications of shunt stubs for microstrip bandpass filters design. Primarily, the four shunt open stubs not only can be utilized to miniaturize the filter but also can be used to design the dual-band filter. Furthermore, the approach of the shunt short stubs is presented to suppress the harmonic and the harmonic is suppressed more than 10 dB. Finally, the designed filters with transmission zeros at finite frequencies give much improved selectivity. Above all, a dual-band filter with the first passband of 2.4 GHz and the second passband of 5.7 GHz is designed and the bandwidth is 0.1 GHz and 0.25 GHz for the first and second passbands, respectively. The insertion loss is less than 1 dB and 3 dB, respectively, and the return loss is more than 10 dB. The rejection between the two transmission bands is more than -17 dB from 2.7 GHz to 4.8 GHz. The results of the measured and simulated data agree well.

The rest of the paper is organized as follows: the theoretical analysis of the new dual-band filter with four transmission zeros by using two coupling half-wavelength resonators with four shunt open stubs is proposed in section II. The harmonic suppression structure with two short

Submitted On: Nov. 11, 2012
Accepted On: Feb. 6, 2013

stubs is presented in section III. In section IV, a microstrip filter with a dual-passband response is fabricated. The conclusion is given in section V.

II. ANALYZING THE COUPLING OF ASYMMETRIC HALF-WAVELENGTH RESONATORS WITH TWO PARALLEL BRANCHES

Figure 1 shows the configuration of the filter using two asymmetric half-wavelength resonators with four shunt open stubs. The total length of the resonator is $l = 2l_3 + l_2 + l_2 = \lambda_0$, where λ_0 is the guided wavelength at the fundamental resonance. The l_4 connected to the resonator is the shunt open stub. The coupling between the two open ends of the resonators is simply expressed by the gap capacitance C_S [10-11].

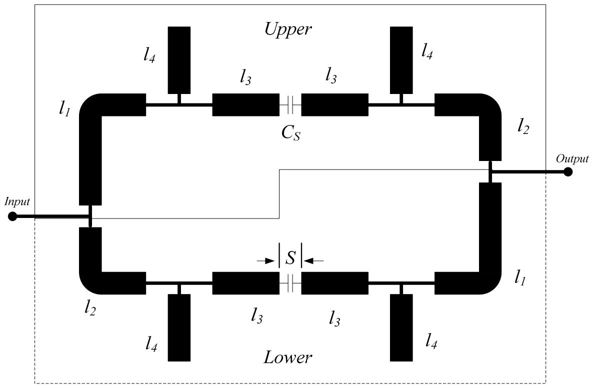

Fig. 1. Configuration of the filter using two asymmetric half-wavelength resonators with four shunt open stubs.

As shown in Fig. 1, the whole circuit represents a shunt circuit, which consists of upper and lower sections. Each section is composed of l_1, l_2, l_3, l_4, and C_S. The ABCD matrices for the upper and lower sections of the lossless shunt circuit are

$$\begin{bmatrix} A & B \\ C & D \end{bmatrix}_{upper} = M_1 M_4 M_3 M_C M_3 M_4 M_2, \quad \text{(1a)}$$

$$\begin{bmatrix} A & B \\ C & D \end{bmatrix}_{lower} = M_2 M_4 M_3 M_C M_3 M_4 M_1, \quad \text{(1b)}$$

with

$$M_n = \begin{bmatrix} \cos\beta l_n & jZ_0 \sin\beta l_n \\ jY_0 \sin\beta l_n & \cos\beta l_n \end{bmatrix} \quad (n = 1,2,3)$$

$$M_C = \begin{bmatrix} 1 & \dfrac{1}{j\omega C_S} \\ 0 & 1 \end{bmatrix},$$

$$M_4 = \begin{bmatrix} 1 & 0 \\ jY_0 \tan\beta l_4 & 1 \end{bmatrix}.$$

Where β is the propagation constant, Z_0 is the characteristic impedance of the resonator, ω is the angular frequency and $Y_0 = 1/Z_0$. The Y-parameters for this circuit can be obtained by adding the upper and the lower section of the Y-parameters, which follow from equations (1a) and (1b), respectively. When the load is matching, S_{21} of the circuit can then be calculated from the total Y-parameters. Furthermore, the transmission zeros can be found by letting $S_{21} = 0$. For a small C_S, an approximate equation can be obtained as,

$$\begin{aligned}&\left[\cos\beta(l_2+l_3)\times\cos\beta(l_1+l_3)-\cos\beta(l_2+l_3)\right]\\ &\times\left[\sin\beta l_1\times\cos\beta l_3\times\tan\beta l_4-\cos\beta(l_1+l_3)\times\sin\beta l_2\times\cos\beta l_3\right]\\ &\times\left[\tan\beta l_4+\sin\beta l_1\times\sin\beta l_2\times\cos\beta l_3^{\,2}\times\tan\beta l_4^{\,2}\right]=0\end{aligned} \quad (2)$$

In generally, we assume $l_1<\lambda_0/4$, $l_2<\lambda_0/4$, $l_3<\lambda_0/4$, $l_4<\lambda_0/4$, where λ_0 is the guided wavelength at fundamental resonance. Thus, we can obtain $\sin\beta l_1\cos\beta l_3\tan\beta l_4 > 0$ and $\sin\beta l_2\cos\beta l_3\tan\beta l_4 > 0$. In addition, we assume $\sin\beta l_1\cos\beta l_3\tan\beta l_4 < 1$ and $\sin\beta l_2\cos\beta l_3\tan\beta l_4 < 1$. The four transmission zeros, f_1, f_2, f_3, and f_4, can be obtained as,

$$f_1 = \frac{c\times n\times arccos(sin\beta l_1 cos\beta l_3 tan\beta l_4)}{2\pi\sqrt{\varepsilon_{eff}}(l_1+l_3)} \quad \text{(3a)}$$

$$f_2 = \frac{c\times n\times arccos(sin\beta l_2 cos\beta l_3 tan\beta l_4)}{2\pi\sqrt{\varepsilon_{eff}}(l_2+l_3)}, \quad \text{(3b)}$$

$$f_3 = \frac{c\times n\times arccos(-\cos\beta l_2\sin\beta l_3\sin\beta l_4)}{2\pi\sqrt{\varepsilon_{eff}}(l_1+l_3+l_4)}, \quad \text{(4a)}$$

$$f_4 = \frac{c\times n\times arccos(-\cos\beta l_1\sin\beta l_3\sin\beta l_4)}{2\pi\sqrt{\varepsilon_{eff}}(l_2+l_3+l_4)}. \quad \text{(4b)}$$

Where ε_{eff} is the effective dielectric constant, n is the mode number, and c is the speed of light in free space. According to [12], the two transmission zeros, f_1' and f_2', in the case of without the stub-loaded resonator, can be written as,

$$f_1'=\frac{c\times n}{4(l_1+l_3)\sqrt{\varepsilon_{eff}}}\ , \tag{5a}$$

$$f_2'=\frac{c\times n}{4(l_2+l_3)\sqrt{\varepsilon_{eff}}}\ . \tag{5b}$$

Comparing equations (3), (4), and (5), the extra passband can be obtained by the shunt open stubs. For the first passband, the center frequency f_{centre} can be obtained as,

$$f_{center} \approx \frac{f_1+f_2}{2}\ .$$

According to equation (5), the center frequency f'_{centre}, in the case of without the shunt open stubs, can be written as,

$$f'_{center} \approx \frac{f_1'+f_2'}{2}\ .$$

Obviously,

$$f_{center} < f'_{center}\ .$$

From the above analysis, the center frequency of the filter can be shifted to a low frequency by shunt open stubs. Therefore, the shunt open stubs can be used to implement the miniaturization of the half-wavelength resonators filter. However, the method will lead to reduced bandwidth after miniaturization. In the asymmetric half-wavelength resonators structure, the reduced bandwidth can be compensated to increase the distance of the two transmission zeros on the two side of the passband.

III. THE SUPPRESSION OF THE SECOND HARMONIC OF THE FIRST PASSBAND

The dual-band bandpass filter is designed with the first passband 2.4 GHz and the second passband 5.7 GHz, however, the second passband suffered from the effect of the second harmonic of the fundamental passband. To suppress the second harmonic of the fundamental passband, the shunt short stubs, as shown in Fig. 2, are designed. The harmonic suppression method of the shunt open stub is reported in [13], but the method of the shunt short stub can work more effective for a dual-band filter with the second passband of 5.7 GHz.

As shown in Fig. 2, there is a shunt short stub in the center of each half-wavelength resonator. The shunt short stub can make the second resonant frequency of the resonators deviated 2 f_0, where f_0 is the fundamental resonant frequency. Similar to [13], assuming $R = f_1/f_0$, where f_1 is the second resonant frequency and R is the ratio of the second resonant frequency and the fundamental frequency.

$$tanR\theta_s = -2tanR\frac{\theta_r}{2}\ , \tag{6}$$

where θ_r is the electrical lengths of the resonant and θ_s is the electrical lengths of the shunt short stub.

Equation (6) presents the relationship between the length of the shunt short stub and the second harmonic frequency. And the resonators with different second resonant frequency can make the harmonic suppression more effective [13]. The responses of the filter with and without the harmonic suppression structure are showed in Fig. 3. The second harmonic of the fundamental passband is suppressed more than 10 dB, as shown in Fig. 3 (b).

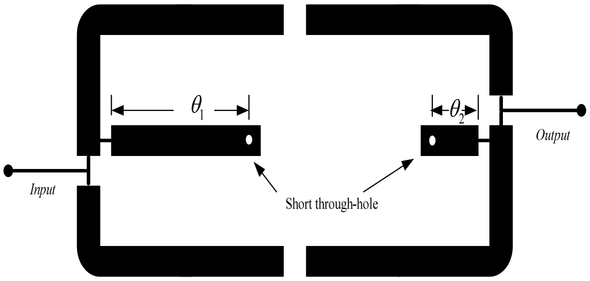

Fig. 2. The asymmetric half-wavelength resonators with shunt short stubs structure.

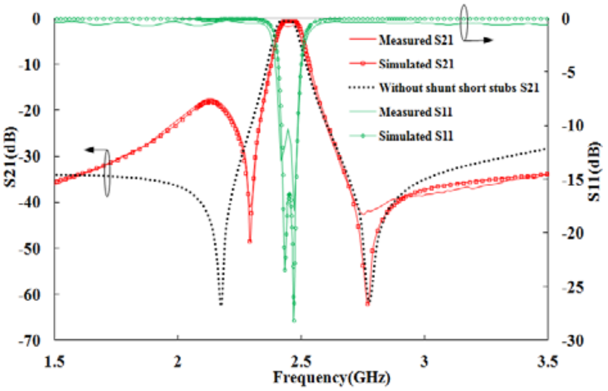

(a)

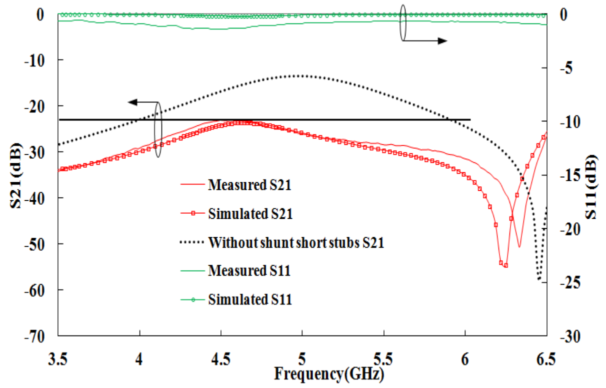

(b)

Fig. 3. The responses of the filter shown in Fig. 2 for, (a) the responses of the first passband and (b) the responses of the second harmonic.

IV. DUAL-BAND MICROSTRIP BANDPASS FILTER WITH FOUR TRANSMISSION ZEROS

Based on the theories presented above, a dual-band bandpass filter is designed with the first passband of 2.4 GHz and the second passband of 5.7 GHz. The Agilent technologies' Advanced Design System (ADS) is used for design and optimizing the filter and the commercial TLX dielectric substrate with a relative dielectric constant of 2.45 and a thickness of 0.79 mm is chosen for the filter design. The physical dimensions of the filter and its photograph are shown in Fig. 4.

The S-parameter simulation and measurement results for this filter are shown in Fig. 5. It can be seen that the first passband with center frequency of 2.45 GHz has less than 1dB insertion loss and greater than 10 dB return loss. The second passband with center frequency of 5.7 GHz has less than 3 dB insertion loss and greater than 10 dB return loss. The bandwidth is 0.1 GHz and 0.25 GHz for the first and second passbands, respectively. In addition, the better cutoff rate in the stopband is provided by four transmission zeros.

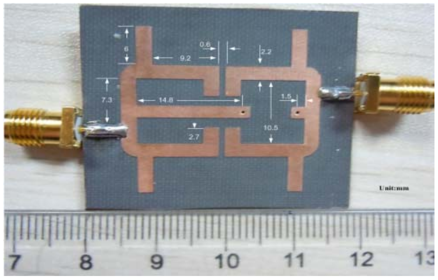

Fig. 4. The photograph of the proposed filter.

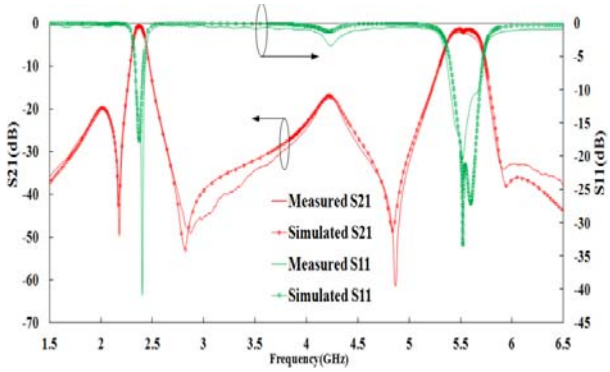

Fig. 5. The responses of the dual-band filter.

V. CONCLUSION

A theory of creating four transmission zeros is proposed by two coupling half-wavelength resonators with four shunt open stubs. Then, in order to suppress the harmonic, the approach of the shunt short stub is presented and the harmonic is suppressed more than 10 dB. Finally, based on the method presented above, a dual-band filter with the first passband of 2.4 GHz and the second passband of 5.7 GHz is designed and the bandwidth is 0.1 GHz and 0.25 GHz for the first and second passbands, respectively. The insertion loss is less than 1 dB and 3 dB, respectively, and the return loss is more than 10 dB. In addition, the designed filters with transmission zeros at finite frequencies give much improved selectivity. The rejection between two transmission bands is more than -17 dB from 2.7 GHz to 4.8 GHz.

ACKNOWLEDGMENT

This work was supported by National Natural Science Foundation of China (No. 61072009), the support from Fundamental Research Funds for the Central Universities.

REFERENCES

[1] H. Miyake, S. Kitazawa, T. Ishizaki, T. Yamada, and Y. Nagatomi, "A miniaturized monolithic dual band filter using ceramic lamination technique for dual mode portable telephones," *IEEE MTT-S Int. Microw. Symp. Dig.*, Denver, CO, pp. 789-792, June 1997.

[2] Y. X. Guo, L. C. Ong, M. Y. W. Chia, and B. Luo, "Dual-band bandpass filter in LTCC," *IEEE MTT-S Int. Microwave Symp. Dig.*, Long Beach, CA, June 2005.

[3] C. Y. Chen and C. Y. Hsu, "A simple and effective method formicrostrip dual-band filters design," *IEEE Microw. Wireless Compon. Lett.*, vol. 16, no. 5, pp. 246-248, May 2006.

[4] C. Y. Hsu, C. Y. Chen, and H. R. Chuang, "Design of microstrip miniature dual-band filter using embedded resonators," *Proceedings of Asia-Pacific Microwave Conference*, Yokohama, Japan, pp. 1811-1813, Dec. 2006.

[5] F. H. Guan, X. W. Sun, and W. Xue, "Design of a tunable dual-band filter using step-impedance resonators with wide stopband," *Proceedings of 2008 Global Symposium on Millimeter Waves*, Nanjing, China, pp. 362-364, Apr. 2008.

[6] A. Eroglu and R. Smith, "Triple band bandpass filter design and implementation using SIRs," *26th Annual Review of Progress in Appl. Comp. Electro. Society (ACES)*, Tampere, Finland, Apr. 2010.

[7] F. Karshenas, A. R. Mallahzadeh, and J. Rashed-Mohassel, "Size reduction and harmonic suppression of parallel coupled-line bandpass filters using defected ground structure," *Appl. Comp. Electro. Society (ACES) Journal*, vol. 25, no. 2, pp. 149-155, Feb. 2010.

[8] C. Quendo, E. Rius, and C. Person, "Narrow bandpass filters using dual-behavior resonators," *IEEE Trans. Microwave Theory Tech.*, vol. 51, pp. 734-743, Mar. 2003.

[9] C. Quendo, E. Rius, and C. Person, "Narrow bandpass filters using dual-behavior resonators based on stepped-impedance stubs and different-length stubs," *IEEE Trans. Microwave Theory Tech.*, vol. 53, pp. 1034-1044, Mar. 2004.

[10] S. Y. Lee and C. M. Tsai, "New cross-coupled filter design using improved hairpin resonators," *IEEE Trans. Microwave Theory Tech.*, vol. 48, pp. 2482-2490, Dec. 2000.

[11] K. C. Gupta, R. Garg, I. Bahl, and P. Bhartia, *Microstrip Lines and Slotlines*, 2^{nd} ed. Artech House, Boston, MA, 1996.

[12] L. H. Hsieh and K. Chang, "Tunable microstrip bandpass filters with two transmission zeros," *IEEE Trans. Microwave Theory Tech.*, vol. 51, no. 2, pp. 520-525, Feb. 2003.

[13] W. H. Tu, H. F. Li, K. A. Michalski, and K. Chang, "Microstrip open-loop ring bandpass filter using open stubs for harmonic suppression," *IEEE MTT-S Int. Microw. Symp. Dig.*, San Francisco, CA, USA, pp. 357-360, June 2006.

Xiuping Li, professor in Beijing University of Posts and Telecommunications, PhD supervisor. She received the B.Sc. degree from Shandong University, China, in 1996, and the Ph.D. degree from Beijing Institute of Technology, Beijing, China. From 2001 to 2003, she went to Nanyang Technological University (NTU) in Singapore for post-doctor. From 2004, she joint Yonsei University in Korea as research professor. On March, 2006, she joint Technology University Berlin (TU-Berlin) in German as senior visiting scholar. From July to September in 2007, she joint Carleton University in Canada as visiting scholar. Prof. Li cooperated with scientists from Singapore, Korea and German has conducted systematical research on the design and artificial neural network modeling of microwave and RF passive and active device, microwave and RF measurement and the high frequency modeling of III-V group compounds semiconductor device, and has obtained many achievements. She has more than 50 papers published on academic journal and conference in domestics and overseas, where more than 20 papers are indexed by SCI. She has applied for 5 national patents, 3 books of her have been published. In 2007, she has been selected into program of ministry of education for new Century Excellent Talents. In 2008，she has been selected into Beijing Nova Program.

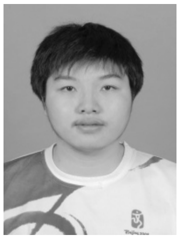

Junjie Zeng was born in Sichuan Province, China, 1987. He received the B.Sc. degree from the School of Information and telecommunication Engineering, Beijing University of Posts and Telecommunications (BUPT), Beijing China, in 2011, where he is currently working toward the M.Sc. degree. His main research interests are antennas and microwave circuit components.

Stop-Band Filter using A New Metamaterial Complementary Split Triangle Resonators (CSTRs)

M. A. Abaga Abessolo, Y. Diallo, A. Jaoujal, A. El Moussaoui, and N. Aknin

Information and Telecommunication Systems Laboratory (LaSIT)
Faculty of Sciences, Abdelmalek Essaadi University, Tetuan, Morocco
Michelabaga1@yahoo.fr, aknin@ieee.org

Abstract **─** In this paper, a compact stop-band microstrip filter based on a new complementary split triangle resonator (CSTRs) is presented. We first describe the structure of the resonator and present its characteristics, which are essentially a simultaneous negative-ε and negative-μ. Then, we apply the complementary of this structure on a microstrip device. The result gives stop-band filter with high rejection band around the resonance frequency of the CSTRs (3.2GHz). The substrate used is the FR4.

Index Terms **─** Metamaterial, split triangle resonators, and stop-band filter.

I. INTRODUCTION

Recently, there has been an extensive research effort within the electromagnetic community to develop and use novel metamaterials. Among these materials electromagnetic bandgap (EBG) structures, a simultaneous negative μ and ε with left-handed (LH) media have received much attention in the microwave and millimeter wave community [1-6]. Split ring resonators (SRRs) proposed by Pendry et al. [1] attracted much attention as a canonical metamaterial structure that gives rise to an effective magnetic response without the need for magnetic materials. SRRs have been successfully applied to the fabrication of LHM. Since then, there have been large numbers of experimental investigations on the observation of this phenomenon. However, there are still some drawbacks such as high losses and limited bandwidth and anisotropic property preventing its further development. These issues prompted researchers to explore new designs such as omega pattern [2-4], S-type [5] or triangular split ring resonator and wire strip [6].

It is well known that the complementary of a planar metallic structure is obtained by replacing the metal parts of the original structure with apertures, and the apertures with metal plates [7]. Due to symmetry considerations, it can be demonstrated that if the thickness of the metal plate is zero, and its conductivity is infinity (perfect electric conductor), then the apertures behave as perfect magnetic conductors. In that case the original structure and its complementary are effectively dual and if the field $F = (E, H)$ is a solution for the original structure, its dual F' defined by,

$$F' = \left(E', H'\right) = \left(-\sqrt{\frac{\mu}{\varepsilon}}.H, \sqrt{\frac{\varepsilon}{\mu}}.E\right) \qquad (1)$$

is the solution for the complementary structure (rigorously speaking is the solution on one side of the plane, and on the other side, due to the lack of magnetic charges in the apertures) [8]. Many researchers proposed microwave structures based on split ring resonator and complementary split ring resonator with metamaterial properties [9-12].

In this paper, a microstrip filter based on a new metamaterial particle named split triangle resonator (STR) with simultaneous negative permittivity and permeability, which are essentials characteristics of metamaterial structures [13]. Then, we use complementary split triangle resonator (CSTRs) to design a band-stop filter in microstrip technology. The CSTRs will be implemented in microstrip technology by etching the triangle particles in the ground plane, just underneath the conductor strip. This position of CSTR is properly excited, this time by an electric field polarized in the axial direction of the triangle particle. In contrast to the usual $\lambda_g / 2$ transmission line resonators, CSTRs are sub-lambda structures,

Submitted On: April 29, 2012
Accepted On: Jan. 16, 2013

i.e., their dimensions are electrically small at the resonant frequency (typically one tenth of the guided wavelength or less). Therefore, high level of miniaturization is expected by using these particles.

II. RESONATOR DESIGN AND SIMULATION STUDY

The split triangle resonator (STRs) is formed by two coupled conducting triangles printed on a dielectric slab. Assuming a particle size much smaller than the free space wavelength, the STR's essentially behaves as a quasistatic RLC circuit fed by the external magnetic flux linked by the particle. Figure 1 (a) shows the cubic unit cell of the proposed structure, composed by a 0.5 mm thick substrate of FR4 (ε_r = 4.4, loss tangent of 0.02) and a copper STR positioned on the top side of the substrate. The cubic cell dimension is a = 15.4 mm. Figure 1 (b) presents the planar view of the top side of the unit with dimensions a = 15.4 mm, b = 16 mm, g = 6 mm, d = 10 mm, e = 0.4 mm, P = 0.6 mm, and m = 1 mm. S-parameters were determined via full-wave simulations. Effective medium parameters (ε, μ) were determined using the standard transfer matrix method [14, 15].

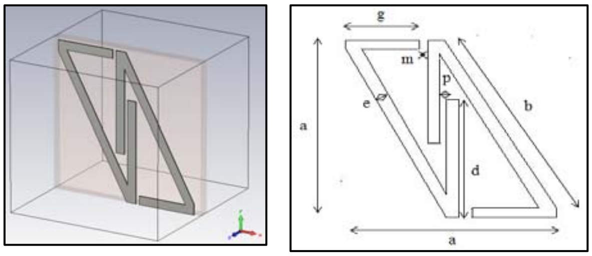

(a) (b)

Fig. 1. Split triangle resonators (STRs), (a) perspective view of the unit cell and (b) planar view of the unit cell.

Figure 2 presents the amplitude of the calculated S-parameters for the metamaterial structure, it can be seen that S_{11} is equal to S_{22}, and S_{12} is equal to S_{21}, since the structure is symmetric and indeed roughly matched at 3.5 GHz. Accordingly, using the standard retrieval method [14], the results for an effective refractive index, effective permittivity, and permeability are presented.

As shown in Fig. 3, the range of the simultaneous negative permittivity and permeability starts from 3.2 GHz to 3.75 GHz. Moreover, Fig. 4 confirms the negative index of the split triangle resonator.

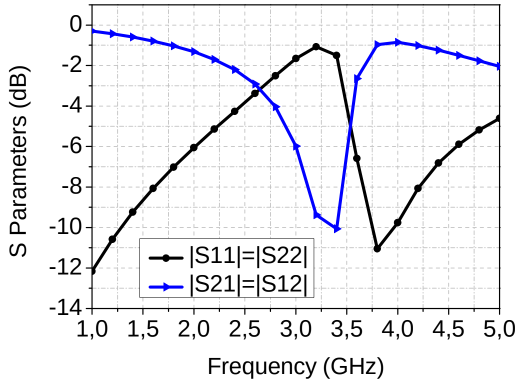

Fig. 2. S-parameters.

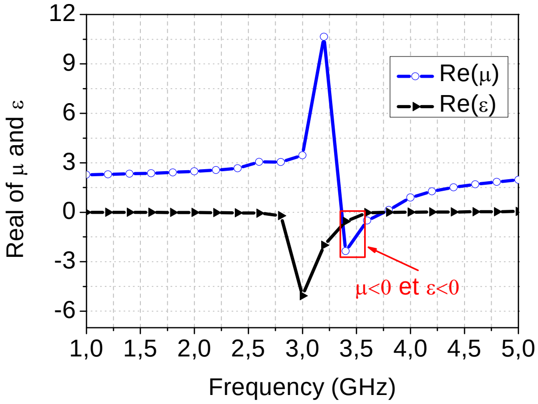

Fig. 3. Real permeability and permittivity.

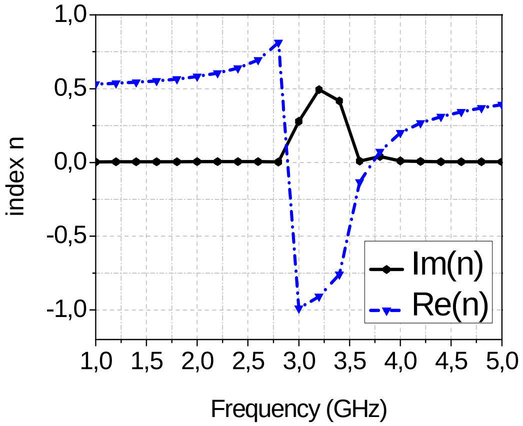

Fig. 4. Index of unit split triangle resonator.

III. STOP-BAND MICROSTRIP FILTER DESIGN BY ETCHING CSTRs ON THE GROUND PLANE

A. Filter description

Usually, in the microstrip technology, complementary split ring resonators are achieved by periodically etching capacitive gaps in the ground plane underneath the 50 Ω microstrip line [16-19]. Since ours CSTRs are excited by the electric field, they produce negative effective permittivity $\mathrm{Re}(\varepsilon_{eff}) < 0$ and negative effective permeability $\mathrm{Re}(\mu_{eff}) < 0$.

Thus, a time varying electric field having a strong component in the axial direction gives rise to ε and μ effective medium. Considering this fact in mind, the working mechanism of the CSTRs based stop-band filter can be explained as follows: a microstrip transmission line induces electric field lines that originate from the central strip and terminate perpendicularly on the ground plane. Due to the presence of dielectric substrate, field lines are tightly concentrated just beneath the central conductor and the electric flux density reaches its strongest value in the vicinity of this region. Therefore, if CSTRs is etched on the ground plane aligned with the strip, a strong electric coupling with the desired polarization is expected.

Figure 5 (a) (top view) and Fig. 5 (b) (bottom view) show the geometry of the CSTRs loaded microstrip on an FR4 substrate of $\varepsilon_r = 4.4$, $\tan\delta = 0.02$, and thickness = 1.5 mm. All dimensions of the CSTRs have been selected identical to their STR counterparts (Fig. 1 (b)) so that the operating frequency of the filter is also around 3.25 GHz. Figure 5 (c) presents photograph of the fabricated prototype using Protomat S100.

B. Simulation and experimental results

The proposed filter has been simulated and measured. Figures 6 (a), 6 (b), and 6 (c) show the simulated frequency response (S_{11} and S_{21}) of the proposed filter with various numbers of CSTRs. In all cases, a deep rejection band is obtained around the design frequency. It is oblivious that the rejection characteristic depends on the number of SRRs used. The best rejection is found using two CSTRs.

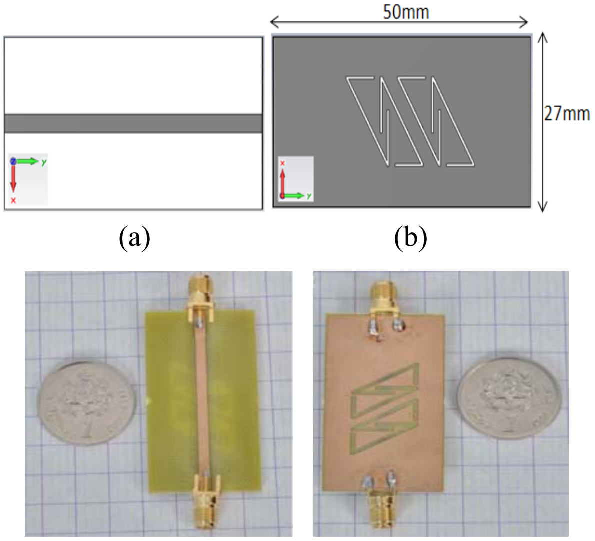

(a) (b)

Top view Bottom view

(c)

Fig. 5. (a) Top view of microstrip stop-band filter with CSTRs etched into the ground plane, (b) bottom view of proposed filter, and (c) photograph of the fabricated prototype.

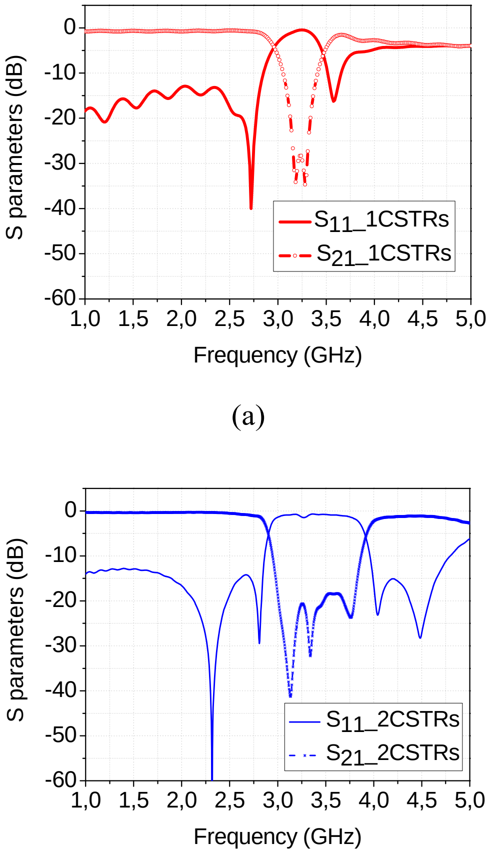

(a)

(b)

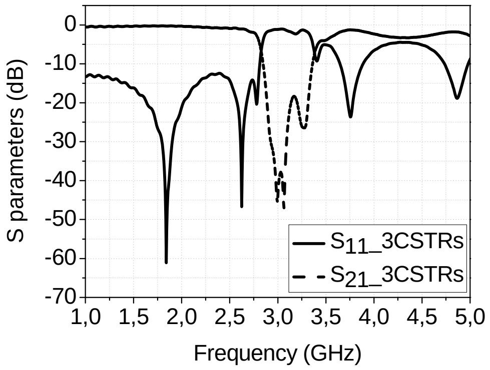

(c)

Fig. 6. Results of the stop-band filter with CSTRs on the ground plane, (a) S_{11} and S_{21} of the proposed microstrip filter with 1 CSTRs, (b) S_{11} and S_{21} of the proposed microstrip filter with 2 CSTRs, and (c) S_{11} and S_{21} of the proposed microstrip filter with 3 CSTRs.

We present simulation result of all S-parameters in Fig. 7. We observe a symmetric characteristic of the proposed filter. The comparison results are shown in Fig. 8. Very good agreement is obtained between simulated and measured results. The small discrepancies can be attributed to fabrication tolerances and to the dissipative losses not taken into account in the simulation. A deep rejection band is obtained around 3.25 GHz, with sharp cutoffs, maximum rejection of 30 dB, and low return losses.

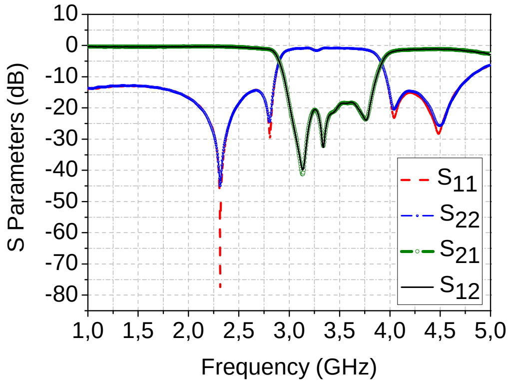

Fig. 7. Simulated S-parameters of the proposed filter (S_{11}, S_{22}, S_{21}, and S_{12}).

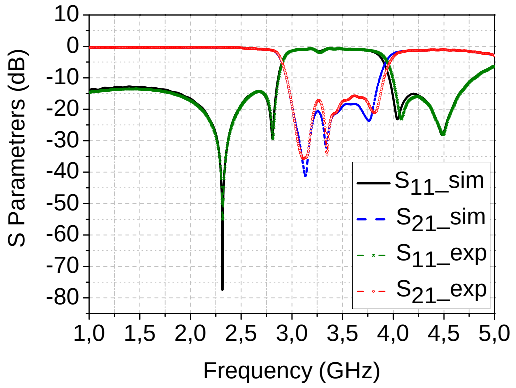

Fig. 8. Comparison of measured and simulated S-parameters (S_{11} and S_{21}) for the proposed stop-band filter in microstrip technology based on complementary STRs.

IV. CONCLUSION

In this paper, a new metamaterial resonator (STRs) with simultaneous negative-ε and negative-μ is presented and applied on microstrip stop-band filter. The compact stop-band microstrip filter based on CSTRs has been proposed and successfully tested. The measured result shows a good agreement with experimental measurement and simulation. We observed that the proposed device is very compact and produces very high rejection band around the resonance frequency of CSTRs.

REFERENCES

[1] J. B. Pendry, A. J. Holden, D. J. Robbins, and W. J. Stewart, "Magnetism from conductors and enhanced nonlinear phenomena," *IEEE Trans. on Microwave Theory and Techniques,* vol. 47, no. 11, Nov. 1999.

[2] C. R. Simovski and S. L. He, "Frequency range and explicit expressions for negative permittivity and permeability for an isotropic medium formed by a lattice of perfectly conducting omega particles," *Phys. Lett.*, vol. A, no. 311, pp. 254, 2003.

[3] L. Ran, J. Huangfu, H. Chen, Y. Li, X. Zhang, K. Chen, and J. A. Kong, "Microwave solid-state left-handed material with a broad bandwidth and an ultralow loss," *Phys. Rev.*, vol. B, no. 70, 2004.

[4] M. A. Abessolo, A. El Moussaoui, and N. Aknin, "Dual-band monopole antenna with omega particles for wireless applications," *Progress In Electromagnetics Research Letters,* vol. 24, pp. 27-34, 2011.

[5] H. Chen, L. Ran, J. Huangfu, X. Zhang, and K. Chen, "Left-handed materials composed of only S-shaped resonators," *Phys. Rev.*, E, vol. 70, 2004.

[6] C. Sabah, "Tunable metamaterial design composed of triangular split ring resonator and wire strip for S and C microwaves bands," *Progress In Electromagnetics Research B,* vol. 22, pp. 341-357, 2010.

[7] H. G. Booker, "Slot aerials and their relation to complementary wire aerials (Babinet's principle)," *J. Inst. Elect. Eng., pt. III-A,* vol. 93, no. 4, pp. 620-626, May 1946.

[8] G. A. Deschamps, "Impedance properties of complementary multi-terminal planar structures," *IRE Trans. Antennas Propagat.*, vol. 7, pp. 371-378 Dec. 1959.

[9] A. Alù, F. Bilotti, N. Engheta, and L. Vegni, "Sub-wavelength, compact, resonant patch antennas loaded with metamaterials," *IEEE Trans. Antennas Propagat.*, vol. 55, no. 1, pp. 13-25, 2007.

[10] F. Falcone, T. Lopetegi, J. D. Baena, R. Marqués, F. Martín, and M. Sorolla, "Effective negative-ε stopband microstrip lines based on complementary split ring resonators," *IEEE Microwave and Wireless Compoments Lett.,* vol. 14, no. 6, June 2004.

[11] B. D. Braaten, R. P. Scheeler, M. Reich, R. M. Nelson, C. Bauer-Reich, J. Glower, and G. J. Owen, "Compact metamaterial-based UHF RFID antennas: deformed omega and split-ring resonator structures," *Appl. Comp. Electro. Society (ACES) Journal*, vol. 25, no. 6, pp. 530-542, June 2010.

[12] Z. Duan and S. Qu, Y. Hou, "Electrically small antenna inspired by spired split ring resonator," *Progress In Electromagnetics Research Letters*, vol. 7, pp. 47-57, 2009.

[13] M. A. Abessolo, N. Aknin, and A. El Moussaoui, "A new left-handed metamaterial structure based on split-triangle resonators (STRs)," *Appl. Comp. Electro. Society (ACES) Journal*, vol. 26, no. 11, Nov. 2011.

[14] D. R. Smith, D. C. Vier, Th. Koschny, and C. M. Soukoulis, "Electromagnetic parameter retrieval from inhomogeneous metamaterials," *Foundation for Research and Technology Hellas (FORTH),* 71110 Heraklion, Crete, Greece, March 2005.

[15] D. R. Smith, S. Schultz, P. Markoš, and C. M. Soukoulis, "Determination of effective permittivity and permeability of metamaterials from reflection and transmission coefficient," *Phys. Rev.* vol. B 65, 195104, 2002.

[16] Q. -L. Zhang, W. -Y. Yin, S. He, and L. -S. Wu, "Evanescent-mode substrate integrated waveguide (SIW) filters implemented with complementary split ring resonators," *Progress In Electromagnetics Research*, vol. 111, pp. 419-432, 2011.

[17] X. -C. Zhang, Z. -Y. Yu, and J. Xu, "Novel band-pass substrate integrated waveguide (SIW) filter based on complementary split ring resonators (CSRRs)," *Progress In Electromagnetics Research*, vol. 72, pp. 39-46, 2007.

[18] X. Hu, Q. Zhang, and S. He, "Compact dual-band rejection filter based on complementary meander line split ring resonator," *Progress In Electromagnetics Research Letters*, vol. 8, pp. 181-190, 2009.

[19] M. Keshvari and M. Tayarani, "A novel miniaturized bandpass filter based on complementary split ring resonators (CSRRs) and open-loop resonators," *Progress In Electromagnetics Research Letters*, vol. 23, pp. 165-172, 2011.

Michel Audrey Abaga Abessolo was born in Oyem, Gabon, in January 1981. He received the License of Sciences in physics and the DESA degree in Information and Telecommunication Systems from the Abdelmalek Essaadi University, Tetuan, Morocco, respectively, in 2005 and 2007. In 2012, he received the PhD degree in Electrical Engineering from Abdelmalek Essaadi University in Tetouan, Morocco. His current interest includes microwave antennas, filters based on enhanced transmission phenomena, and metamaterials. He has been a Professor of physics in Omar Bongo University, Libreville, Gabon since December 2012.

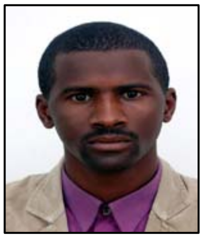

Diallo Yaccoub Mohamed Hamidne was born in Monguel, Mauritania, in 1982. He received B.Sc. degree in Physics-Chemistry from Nouakchott University, Mauritania, and M.Sc. degree in Electronics and Telecommunications from the Abdelmalek Essaadi University, Tetuan, Morocco, respectively in 2007 and 2009. He is currently working toward the Ph.D. degree at the Abdelmalek Essaadi University. His current interest includes electronic engineering for wireless systems.

A. El Moussaoui received the PhD degree in Electronics at the University of Bradford in 1990. In 2007 he received the international Master in E-learning in the Curt Bosh institute in Switzerland. He has been a member of the organizing and the scientific committees of several symposia and conferences dealing with RF, mobile networks and information technologies. He has participated in several projects with France and Spain. His research interests are: electronic engineering, third generation mobile system, radio network planning and optimization. Currently, he is the vice president of Abdelmalek Essaidi University in Tetuan Morocco.

Noura Aknin received the License in Physics and the PhD degree in Electrical Engineering, respectively, in 1988 and 1998 from Abdelmalek Essaadi University in Tetouan, Morocco. She is a Professor of Telecommunications and Computer Engineering in Abdelmalek Essaadi University since 2000. She is the co-founder of the IEEE Morocco Section since November 2004 and she is the Women in Engineering Coordinator. She has been a member of the organizing and the scientific committees of several symposia and conferences dealing with RF, mobile networks, and social web and information technologies. She is a member of the IEEE communications society and computer society. Her research interests focus mainly on Wireless and mobile communication systems, radio network planning and optimization. Moreover, she is the project manager for research and development project related to mobile networks funded by the national telecommunications company “Maroc Telecom”.

2013 INSTITUTIONAL MEMBERS

DTIC-OCP LIBRARY
8725 John J. Kingman Rd, Ste 0944
Fort Belvoir, VA 22060-6218

AUSTRALIAN DEFENCE LIBRARY
Northcott Drive
Canberra, A.C.T. 2600 Australia

BEIJING BOOK CO, INC
701 E Linden Avenue
Linden, NJ 07036-2495

DARTMOUTH COLLEGE
6025 Baker/Berry Library
Hanover, NH 03755-3560

DSTO EDINBURGH
AU/33851-AP, PO Box 830470
Birmingham, AL 35283

SIMEON J. EARL – BAE SYSTEMS
W432A, Warton Aerodome
Preston, Lancs., UK PR4 1AX

ENERGY KEN LIBRARY
PO Box 300613
Jamaica, NY, 11430

ENGINEERING INFORMATION, INC
PO Box 543
Amsterdam, Netherlands 1000 Am

ETSE TELECOMUNICACION
Biblioteca, Campus Lagoas
Vigo, 36200 Spain

GA INSTITUTE OF TECHNOLOGY
EBS-Lib Mail code 0900
74 Cherry Street
Atlanta, GA 30332

TIMOTHY HOLZHEIMER
Raytheon
PO Box 1044
Rockwall, TX 75087

HRL LABS, RESEARCH LIBRARY
3011 Malibu Canyon
Malibu, CA 90265

IEE INSPEC
Michael Faraday House
6 Hills Way
Stevenage, Herts UK SG1 2AY

INSTITUTE FOR SCIENTIFIC INFO.
Publication Processing Dept.
3501 Market St.Philadelphia, PA
19104-3302

LIBRARY – DRDC OTTAWA
3701 Carling Avenue
Ottawa, Ontario, Canada K1A OZ4

LIBRARY of CONGRESS
Reg. Of Copyrights
Washington DC, 20559

LINDA HALL LIBRARY
5109 Cherry Street
Kansas City, MO 64110-2498

MISSOURI S&T
400 W 14th Street
Rolla, MO 56409

MIT LINCOLN LABORATORY
244 Wood Street
Lexington, MA 02420

NATIONAL CHI NAN UNIVERSITY
Lily Journal & Book Co, Ltd
20920 Glenbrook Drive
Walnut, CA 91789-3809

JOHN NORGARD
UCCS
20340 Pine Shadow Drive
Colorado Springs, CO 80908

OSAMA MOHAMMED
Florida International University
10555 W Flagler Street
Miami, FL 33174

NAVAL POSTGRADUATE SCHOOL
Attn:J. Rozdal/411 Dyer Rd./ Rm 111
Monterey, CA 93943-5101

NDL KAGAKU
C/0 KWE-ACCESS
PO Box 300613 (JFK A/P)
Jamaica, NY 11430-0613

OVIEDO LIBRARY
PO BOX 830679
Birmingham, AL 35283

DAVID PAULSEN
E3Compliance
1523 North Joe Wilson Road
Cedr Hill, TX 75104-1437

PENN STATE UNIVERSITY
126 Paterno Library
University Park, PA 16802-1808

DAVID J. PINION
1122 E Pike Street #1217
SEATTLE, WA 98122

KATHERINE SIAKAVARA
Gymnasiou 8
Thessaloniki, Greece 55236

SWETS INFORMATION SERVICES
160 Ninth Avenue, Suite A
Runnemede, NJ 08078

YUTAKA TANGE
Maizuru Natl College of Technology
Maizuru, Kyoto, Japan 625-8511

TIB & UNIV. BIB. HANNOVER
Welfengarten 1B
Hannover, Germany 30167

UEKAE
PO Box 830470
Birmingham, AL 35283

UNIV OF CENTRAL FLORIDA
4000 Central Florida Boulevard
Orlando, FL 32816-8005

UNIVERSITY OF COLORADO
1720 Pleasant Street, 184 UCB
Boulder, CO 80309-0184

UNIVERSITY OF KANSAS – WATSON
1425 Jayhawk Blvd 210S
Lawrence, KS 66045-7594

UNIVERSITY OF MISSISSIPPI
JD Williams Library
University, MS 38677-1848

UNIVERSITY LIBRARY/HKUST
Clear Water Bay Road
Kowloon, Honk Kong

CHUAN CHENG WANG
8F, No. 31, Lane 546
MingCheng 2nd Road, Zuoying Dist
Kaoshiung City, Taiwan 813

THOMAS WEILAND
TU Darmstadt
Schlossgartenstrasse 8
Darmstadt, Hessen, Germany 64289

STEVEN WEISS
US Army Research Lab
2800 Powder Mill Road
Adelphi, MD 20783

YOSHIHIDE YAMADA
NATIONAL DEFENSE ACADEMY
1-10-20 Hashirimizu
Yokosuka, Kanagawa,
Japan 239-8686

APPLIED COMPUTATIONAL ELECTROMAGNETICS SOCIETY JOURNAL
http://aces.ee.olemiss.edu

INFORMATION FOR AUTHORS

PUBLICATION CRITERIA

Each paper is required to manifest some relation to applied computational electromagnetics. **Papers may address general issues in applied computational electromagnetics, or they may focus on specific applications, techniques, codes, or computational issues.** While the following list is not exhaustive, each paper will generally relate to at least one of these areas:

1. **Code validation.** This is done using internal checks or experimental, analytical or other computational data. Measured data of potential utility to code validation efforts will also be considered for publication.

2. **Code performance analysis.** This usually involves identification of numerical accuracy or other limitations, solution convergence, numerical and physical modeling error, and parameter tradeoffs. However, it is also permissible to address issues such as ease-of-use, set-up time, run time, special outputs, or other special features.

3. **Computational studies of basic physics.** This involves using a code, algorithm, or computational technique to simulate reality in such a way that better, or new physical insight or understanding, is achieved.

4. **New computational techniques** or new applications for existing computational techniques or codes.

5. **"Tricks of the trade"** in selecting and applying codes and techniques.

6. **New codes, algorithms, code enhancement, and code fixes.** This category is self-explanatory, but includes significant changes to existing codes, such as applicability extensions, algorithm optimization, problem correction, limitation removal, or other performance improvement. **Note: Code (or algorithm) capability descriptions are not acceptable, unless they contain sufficient technical material to justify consideration.**

7. **Code input/output issues.** This normally involves innovations in input (such as input geometry standardization, automatic mesh generation, or computer-aided design) or in output (whether it be tabular, graphical, statistical, Fourier-transformed, or otherwise signal-processed). Material dealing with input/output database management, output interpretation, or other input/output issues will also be considered for publication.

8. **Computer hardware issues.** This is the category for analysis of hardware capabilities and limitations of various types of electromagnetics computational requirements. Vector and parallel computational techniques and implementation are of particular interest.

Applications of interest include, but are not limited to, antennas (and their electromagnetic environments), networks, static fields, radar cross section, inverse scattering, shielding, radiation hazards, biological effects, biomedical applications, electromagnetic pulse (EMP), electromagnetic interference (EMI), electromagnetic compatibility (EMC), power transmission, charge transport, dielectric, magnetic and nonlinear materials, microwave components, MEMS, RFID, and MMIC technologies, remote sensing and geometrical and physical optics, radar and communications systems, sensors, fiber optics, plasmas, particle accelerators, generators and motors, electromagnetic wave propagation, non-destructive evaluation, eddy currents, and inverse scattering.

Techniques of interest include but not limited to frequency-domain and time-domain techniques, integral equation and differential equation techniques, diffraction theories, physical and geometrical optics, method of moments, finite differences and finite element techniques, transmission line method, modal expansions, perturbation methods, and hybrid methods.

Where possible and appropriate, authors are required to provide statements of quantitative accuracy for measured and/or computed data. This issue is discussed in "Accuracy & Publication: Requiring, quantitative accuracy statements to accompany data," by E. K. Miller, *ACES Newsletter,* Vol. 9, No. 3, pp. 23-29, 1994, ISBN 1056-9170.

SUBMITTAL PROCEDURE

All submissions should be uploaded to ACES server through ACES web site (http://aces.ee.olemiss.edu) by using the upload button, journal section. Only pdf files are accepted for submission. The file size should not be larger than 5MB, otherwise permission from the Editor-in-Chief should be obtained first. Automated acknowledgment of the electronic submission, after the upload process is successfully completed, will be sent to the corresponding author only. It is the responsibility of the corresponding author to keep the remaining authors, if applicable, informed. Email submission is not accepted and will not be processed.

EDITORIAL REVIEW

In order to ensure an appropriate level of quality control, papers are peer reviewed. They are reviewed both for technical correctness and for adherence to the listed guidelines regarding information content and format.

PAPER FORMAT

Only camera-ready electronic files are accepted for publication. The term **"camera-ready" means that the material is neat, legible, reproducible, and in accordance with the final version format listed below.**

The following requirements are in effect for the final version of an ACES Journal paper:

1. The paper title should not be placed on a separate page.

The title, author(s), abstract, and (space permitting) beginning of the paper itself should all be on the first page. The title, author(s), and author affiliations should be centered (center-justified) on the first page. The title should be of font size 16 and bolded, the author names should be of font size 12 and bolded, and the author affiliation should be of font size 12 (regular font, neither italic nor bolded).

2. An abstract is required. The abstract should be a brief summary of the work described in the paper. It should state the computer codes, computational techniques, and applications discussed in the paper (as applicable) and should otherwise be usable by technical abstracting and indexing services. The word “Abstract” has to be placed at the left margin of the paper, and should be bolded and italic. It also should be followed by a hyphen (—) with the main text of the abstract starting on the same line.

3. All section titles have to be centered and all the title letters should be written in caps. The section titles need to be numbered using roman numbering (I. II. ….)

4. Either British English or American English spellings may be used, provided that each word is spelled consistently throughout the paper.

5. Internal consistency of references format should be maintained. As a guideline for authors, we recommend that references be given using numerical numbering in the body of the paper (with numerical listing of all references at the end of the paper). The first letter of the authors’ first name should be listed followed by a period, which in turn, followed by the authors’ complete last name. Use a coma (,) to separate between the authors’ names. Titles of papers or articles should be in quotation marks (“ ”), followed by the title of journal, which should be in italic font. The journal volume (vol.), issue number (no.), page numbering (pp.), month and year of publication should come after the journal title in the sequence listed here.

6. Internal consistency shall also be maintained for other elements of style, such as equation numbering. Equation numbers should be placed in parentheses at the right column margin. All symbols in any equation have to be defined before the equation appears or right immediately following the equation.

7. The use of SI units is strongly encouraged. English units may be used as secondary units (in parentheses).

8. Figures and tables should be formatted appropriately (centered within the column, side-by-side, etc.) on the page such that the presented data appears close to and after it is being referenced in the text. When including figures and tables, all care should be taken so that they will appear appropriately when printed in black and white. For better visibility of paper on computer screen, it is good to make color figures with different line styles for figures with multiple curves. Colors should also be tested to insure their ability to be distinguished after black and white printing. Avoid the use of large symbols with curves in a figure. It is always better to use different line styles such as solid, dotted, dashed, etc.

9. A figure caption should be located directly beneath the corresponding figure, and should be fully justified.

10. The intent and meaning of all text must be clear. For authors who are not masters of the English language, the ACES Editorial Staff will provide assistance with grammar (subject to clarity of intent and meaning). However, this may delay the scheduled publication date.

11. Unused space should be minimized. Sections and subsections should not normally begin on a new page.

ACES reserves the right to edit any uploaded material, however, this is not generally done. It is the author(s) responsibility to provide acceptable camera-ready files in pdf and MSWord formats. Incompatible or incomplete files will not be processed for publication, and authors will be requested to re-upload a revised acceptable version.

COPYRIGHTS AND RELEASES

Each primary author must execute the online copyright form and obtain a release from his/her organization vesting the copyright with ACES. Both the author(s) and affiliated organization(s) are allowed to use the copyrighted material freely for their own private purposes.

Permission is granted to quote short passages and reproduce figures and tables from and ACES Journal issue provided the source is cited. Copies of ACES Journal articles may be made in accordance with usage permitted by Sections 107 or 108 of the U.S. Copyright Law. This consent does not extend to other kinds of copying, such as for general distribution, for advertising or promotional purposes, for creating new collective works, or for resale. The reproduction of multiple copies and the use of articles or extracts for commercial purposes require the consent of the author and specific permission from ACES. Institutional members are allowed to copy any ACES Journal issue for their internal distribution only.

PUBLICATION CHARGES

All authors are allowed for 8 printed pages per paper without charge. Mandatory page charges of $75 a page apply to all pages in excess of 8 printed pages. Authors are entitled to one, free of charge, copy of the printed journal issue in which their paper was published. Additional reprints are available for $ 50. Requests for additional re-prints should be submitted to the managing editor or ACES Secretary.

Corresponding author is required to complete the online form for the over page charge payment right after the initial acceptance of the paper is conveyed to the corresponding author by email.

ACES Journal is abstracted in INSPEC, in Engineering Index, DTIC, Science Citation Index Expanded, the Research Alert, and to Current Contents/Engineering, Computing & Technology.